UNIVERSIDAD COMPLUTENSE DE MADRID

Facultad de Ciencias Físicas

TESIS DOCTORAL

Spin-dependentant transport in oxide multiferroic tunnel junctions

Transporte dependiente de espín en uniones túnel multiferroicas de óxidos

MEMORIA PARA OPTAR AL GRADO DE DOCTOR

PRESENTADA POR

Javier Tornos Castilla

Director

Jacobo Santamaría Sánchez-Barriga

Madrid, 2014

Facultad de Ciencias Físicas
Universidad Complutense de Madrid

Spin-dependent transport in oxide multiferroic tunnel junctions

Transporte dependiente de espín en uniones túnel multiferroicas de óxidos

Memoria presentada por

Javier Tornos Castillo

para optar al grado de Doctor en Ciencias Físicas

Directores:

Jacobo Santamaría Sánchez-Barriga

Carlos León Yebra

Madrid, 2014

CONTENTS

1 Introduction

1 Transition metal oxides

Complex transition metal oxides are a wide family of materials which contain elements with incomplete d shells, what gives rise to different forms of magnetic interactions. Almost every electronic or lattice groundstate of solid matter can be found including superconductivity, ferromagnetism, antiferromagnetism, ferroelectricity, multiferroicity etc [1,2]. Distinct members of this class of materials are high T_c superconductors and colossal magnetoresistance manganites which have gathered one of the strongest research efforts in the history of science in terms of number and impact of research articles and number of researchers involved. Many complex oxides share a common perovskite structure where the basic building block is the oxygen octahedron surrounding the transition metal ion. The strong crystal (electric) field generated by the oxygen ions act on the otherwise 5 fold degenerate d levels of the transition metal ion splitting them in e_g and t_{2g} levels which are double and triple degenerate respectively. d orbitals are directional and their overlap mediated by the oxygen p orbitals is weak what yields the narrow d bands with large effective masses. Electrons have thus low mobilities and strongly feel the lattice giving rise to the strong electron lattice coupling (Jahn-Teller) which may further split the degeneracy of crystal field levels. But more importantly, narrow

and directional bands poorly screen the electrostatic repulsion between electrons. The unscreened Coulomb interaction gives rise to strong correlations in the electron system [2]. As a result, the electronic properties cannot be described within conventional one electron band pictures. In a system with one electron per site, expected to be a metal in the one electron band theory of solids, the electrostatic repulsion opens a gap at the Fermi energy. This is the so called Mott gap. Strong electron correlations underlie the strong entanglement between the various interactions in these materials with a multiplicity of competing phases with similar characteristic energies. This is probably at the origin of the rich phase diagrams and of the inhomogeneous ground states displayed by many transition metal oxides [3]. Most likely this competition between interactions also underlies the complex (often giant) collective responses exhibited by these materials upon small perturbations whose understanding and prediction remains a major challenge of condensed matter physics for the years to come [4].

In recent years there has been a lot of activity directed to the growth of heterostructures combining complex transition metal oxides. The strongly correlated nature of the conduction electrons underlying the interplay between the various degrees of freedom is at the origin of the rich variety of new effects and phenomena found at oxide interfaces. The fabrication technique of these oxide heterostructures has reached a level of control comparable to the semiconductor technology and interfaces can be grown with atomic precision allowing the lattices with dissimilar materials to match with a high degree of crystalline perfection. Much in the same way than in the history of semiconductor devices, where interesting effects and phenomena and even novel states of matter have been found at their rather inert interfaces, oxide interfaces constitute an appealing playground for the exploration of exciting new physics [5, 6].

The broken symmetry at the interface between dissimilar correlated oxides underlies the nucleation of emergent electronic phases with unexpected properties far from those of the constituent oxides. Charge density n, repulsion energy U, and band width W, the important parameters critically controlling the properties of correlated oxides are known to vary at interfaces providing interesting avenues to tailor their electronic structure. On the one hand, charge density is known to leak across interfaces as the result from differences between

electrochemical potentials, varying smoothly across the interface over the Thomas Fermi screening length. Repulsive interaction U is also known to depend critically on the ionic environment and band width W is controlled by bond reconstruction (length and angle) at the interface. Since many of these oxides are doped insulators in the vicinity of a metal to insulator transition, the charge density profile at the interface has a critical influence in nucleating novel phases at (the most stable) individual values in a process called electronic reconstruction [7]. Furthermore, since not only n but also U and W change at the interface lattice discontinuity, novel phases nucleate at individual values of n, U and W with unexpected spin and conducting properties in a more general scenario named electronic metamorphosis [5].

2 Motivation

One of the fields were explore oxide interfaces with new multifunctional capabilities has rekindled interest in multiferroics systems which are characterized by the simultaneous presence of magnetic and electric order parameters. These two orders could be coupled leading to a magneto-electric coupling. In naturally occurring multiferroics the magnetoelectric coupling is often weak, and new classes of artificially structured composite materials that combine dissimilar magnetic and ferroelectric systems are being developed to optimize order parameter coupling [8-12]. The possibility of use these functionalities as “active” barrier in tunnel junction architecture brings the opportunity to create new concept tunnel devices. The tunnel current depends sensitively on the density of states at the interface between the barrier and the electrodes, and can thus be used as a probe of the interfacial properties such magneto-electric coupling. Artificial multiferroic tunnel junctions (MFTJ) constituted by ferromagnetic electrodes and ferroelectric tunnel barrier exploit the capability to control electron and spin tunnelling via ferromagnetic and ferroelectric polarizations [13, 14]. The interfacial magneto-electric coupling has been theoretically explored in MFTJ showing that the orientation of ferroelectric polarization in the tunnel barrier affects strongly the interfacial spin polarizations [15] and very recently has been experimentally observed [16, 17]. The origin of the resistive switching in multiferroic tunnel junctions or ferroelectric tunnel junction is still controversial because complex resistive switching mechanisms

involving electrochemical interface reactions associated with ferroelectric polarization reversal that cannot be excluded. Moreover, the effect of defects like oxygen vacancies it has never be explored in multiferroic tunnel junctions. It's kwon that small amount of these defects can produce huge effect in ferroelectric properties such pinning ferroelectric polarization or fatigue, furthermore, the effects oxygen vacancies in the ferroelectric polarization reversal of the tunnel barrier and its influence in the tunneling conductance could be significant.

In this thesis we investigate the spin-dependent transport in complex oxide-based magnetic tunnel junction with a $BaTiO_3$ ferroelectric barrier and $La_{0.7}Sr_{0.3}MnO_3$ ferromagnetic electrodes. We take advantages of the large sensitivity of the tunnel conductance to the interface properties in order to study magnetic and electronic reconstructions at the $La_{0.7}Sr_{0.3}MnO_3/BaTiO_3$ interface, the interplay between ferroelectricity and ferromagnetism and the oxygen vacancies influence. We emphasize the role of the oxygen vacancies in the ferroelectric properties at the nanoscale like ferroelectric polarization reversal and its influence in the spin-dependent tunneling transport.

3 Basic Concepts. Spin dependent tunneling in magnetic tunnel junctions

3.1 Electron tunneling

Electron tunneling is a quantum phenomenon by which an electric current may flow from one electrode, through an insulating barrier, into another electrode. A simple way to understand how tunneling is possible is by considering an electron wave which encounters a potential step, see Figure 1.1. Though most of the intensity is reflected at the potential step, a portion decays exponentially through the barrier. For sufficiently thin barriers (typically few nanometers thick), some intensity remains on the other side of the potential step, and therefore, the electron will have a finite probability of being found on the other side of the potential barrier. The most straightforward realization of this structure is in a metal-insulator-metal (M-I-M) trilayer structure commonly called a tunnel junction, with the insulator typically provided by a metal oxide (e.g. Al_2O_3).

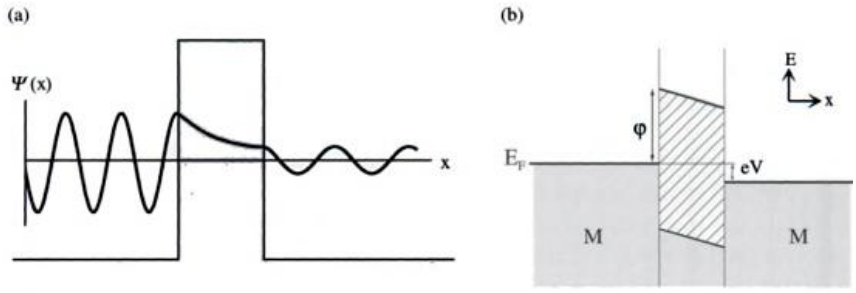

Figure 1.1. (a) Tunneling in metal-insulator-metal structures. (a) Electron wave function decays exponentially in the barrier region, and for thin barriers, some intensity remains in the right side. (b) Potential diagram for a M-I-M structure with applied bias eV- Shaded areas represent filled states, open areas are empty states, and the hatched area represents the forbidden gap in the insulator. Adapted from ref [18].

In most works, tunneling phenomenon in M-I-M structures is studied by observing the current (or its derivative) as a function of applied voltage across the junction. As an illustration, we consider phenomenologically an idealized M-I-M structure, with the electrode-tunnel barrier system modeled as a step potential (Figure 1.1). Without an applied voltage across the junction, the two metals will equilibrate, and the Fermi levels will be at the same energies for the two electrodes. When a bias V is applied across the junction, one Fermi level shift by eV with respect to the other, where e is the electron charge (Figure 1.1 (b)). The number of electrons tunneling from one electrode to the other is given by the product of the density of states at a given energy in the left electrode $\rho_l(E)$, and the density of states at a given energy in the right electrode, $\rho_r(E)$, multiplied by the square matrix element $|M|^2$, which is essentially the probability of transmission through the barrier. One must also then multiply by the probabilities that the states in the left electrode are occupied, f(E), and that the states in the right electrode are empty, 1-f(E-eV)), where f(E) is the Fermi-Dirac function. This product is an expression of the requirement that electrons on one side of the barrier must have empty states to tunnel into on the other side of the barrier. For the general case, the tunnel current I from the left electrode (l) to the right electrode (r) is given by:

$$I_{l\to r}(V) = \int_{-\infty}^{\infty} \rho_l(E)\rho_r(E+eV)|M|^2 f(E)[1-f(E+eV)]dE \qquad (1.1)$$

where the subscript l (r) refers to the left (right) electrode. The total tunnel current is then given by $I_{l\to r} - I_{r\to l}$. Simmons [19] used the WKB approximation to obtain the matrix elements $|M|^2$ for an arbitrary barrier of average height $\bar{\varphi}$ above the common Fermi level E_F. He then calculated the tunnel current from (1.1), using a free electron relation for $\rho_l(E)$, and approximating the Fermi-Dirac functions as step functions (i.e., T = 0). His well known result for a trapezoidal barrier (Figure 1.1) is

$$J(V) = \frac{J_0}{d^2}\left(\bar{\varphi} - \frac{eV}{2}\right) e^{\left[-Ad\sqrt{\bar{\varphi}-\frac{eV}{2}}\right]} - \frac{J_0}{d^2}\left(\bar{\varphi} + \frac{eV}{2}\right) e^{\left[-Ad\sqrt{\bar{\varphi}+\frac{eV}{2}}\right]} \qquad (1.2)$$

where J is the tunnel current density$A = 4\pi\sqrt{2m_e^*}/h$, and $J_0 = e/2\pi h$ are constants, m_e^* is the electron effective mass, d is the barrier thickness, $\bar{\varphi}$ is the average barrier height above the Fermi level, and V is the applied bias. If we take the barrier thickness in Angstroms, the barrier height in electron Volts, and the bias in Volts, then A = 1.025 $eV^{-0.5}$ $Å^{-1}$ and J_0= 6.2 x 10^{10} eV^{-1} $Å^2$, with the resulting current density J in A/cm^2. At moderate voltages, Simmons showed that $J \sim \alpha V + \beta V^3$, which leads to one of the hallmark characteristics of tunneling: a parabolic dependence of conductance ($G \equiv dI/dV$) on voltage, which is often observed experimentally for tunnel junctions. Nevertheless, any dependence of the current density on the electronic density of states (DOS) in the electrodes is suspiciously absent [20], which is a direct result of the over-simplified model used [21, 22]. In practice even junctions with equal electrode materials present different interface properties leading to unequal energy profiles on each side of the insulator. An asymmetric barrier model was reported by Brinkman [23] using a trapezoidal potential barrier model (Figure (b)). Such a model describes the barrier by the width d and the potentials φ_1, φ_2 at the metal-insulator interfaces, where the potential spatial function is:

$$\varphi(x) = \varphi_1 + \frac{x}{t}(\varphi_2 - eV - \varphi_1) \qquad (1.3)$$

If the applied voltage $V \ll \varphi$, the tunnel conductance is:

$$\frac{G(V)}{G\,(0)} = 1 - \frac{A_0 \Delta\varphi}{16\bar{\varphi}^{3/2}} eV + \frac{9A_0^2}{128\bar{\varphi}} (eV)^2 \tag{1.4}$$

where $A_0 = 4\pi d\sqrt{2m_e^*}/3\hbar$, $G(0) = \frac{e^2}{dh^2}\sqrt{2m_e^*\,\bar{\varphi}}e^{\left(\frac{-4\pi}{\hbar}\sqrt{2m_e^*\,\bar{\varphi}}\right)}$, $\Delta\varphi = \varphi_2 - \varphi_1$ is the barrier asymmetry, $\bar{\varphi} = \frac{\varphi_1+\varphi_2}{2}$ is the effective barrier height in eV. This equation are often used to fit experimental J(V) characteristics to obtain effective barrier heights and thicknesses.

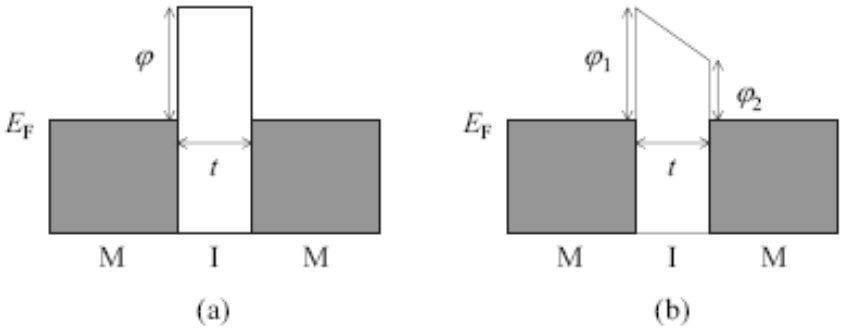

Figure 1.2. Potential schematic of tunnel barrier models (a) Simmons model and (b) Brinkman model.

3.2 Magnetic Tunnel Junctions. The Jullière model

A magnetic tunnel junction (MTJ) consists of an ultra- thin (few nanometers) insulating barrier layer sandwiched by two ferromagnetic metal layers. If a bias voltage is applied between the two metal electrodes across the insulator the electrons can tunnel through the barrier. In a MTJ the tunneling current depends on the relative orientation of the magnetizations of the two ferromagnetic electrodes, which can be controlled by an applied magnetic field (Figure 1.3). This phenomenon is called tunneling magnetoresistance (TMR).

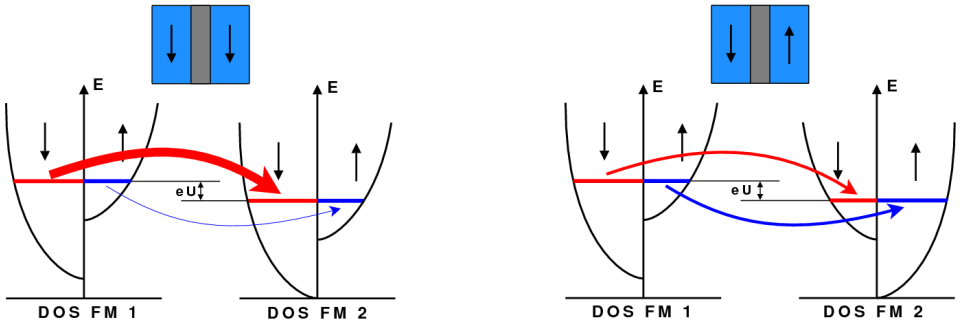

Figure 1.3. Schematic of the spin-dependent tunneling process through an insulating barrier when the magnetizations of the ferromagnetic electrodes are aligned parallel (left) and antiparallel (right) to one another. In this case the tunneling current is larger in the parallel state.

The first TMR experiment was made by Julliere [24] in 1975 using Co and Fe ferromagnetic films and a Ge barrier layer observing sizable magnetoresistance at 4.2 K. Julliere interpreted these results in terms of a simple model assuming that spin of electrons is conserved in the tunneling process and tunnelings of up- and down-spin electrons are two independent processes, so the conductance occurs in the two independent spin channels. According to this assumption, electrons originating from one spin state of the first ferromagnetic film are accepted by unfilled states of the same spin of the second film. If the two ferromagnetic films are magnetized parallel, the minority spins tunnel to the minority states and the majority spins tunnel to the majority states. If, however, the two films are magnetized antiparallel (subscript *AP*) the identity of the majority- and minority-spin electrons is reversed, so the majority spins of the first film tunnel to the minority states in the second film and vice versa. Second, Julliere assumed that the conductance for a particular spin orientation is proportional to the product of the effective (tunneling) DOS of the two ferromagnetic electrodes. According to these assumptions, the conductance for the parallel and antiparallel alignment, G_P and G_{AP}, can be written as follows:

$$G_P \propto \rho_1^{\uparrow}\rho_2^{\uparrow} + \rho_1^{\downarrow}\rho_2^{\downarrow} \tag{1.5}$$

$$G_{AP} \propto \rho_1^{\uparrow}\rho_2^{\downarrow} + \rho_1^{\downarrow}\rho_2^{\uparrow} \tag{1.6}$$

Where $\rho_i^{\uparrow}$ and $\rho_i^{\downarrow}$ are the tunneling DOS of the ferromagnetic electrodes (designated by index i = 1, 2) for the majority- and minority-spin electrons. It follows from equations (1.5) and (1.6) that the parallel- and antiparallel-

magnetized MTJs have different tunnel conductances. TMR is defined as the conductance difference between parallel and antiparallel magnetizations, normalized by the antiparallel conductance. Using equations (1.5) and (1.6), we arrive then at Julliere's formula:

$$TMR = \frac{(G_P - G_{AP})}{G_{AP}} = \frac{(R_{AP} - R_P)}{R_P} = \frac{2P_1P_2}{(1 - P_1P_2)} \quad (1.7)$$

which expresses the TMR in terms of the effective spin polarization of the two ferromagnetic electrodes:

$$P_i = \frac{\rho_i^{\uparrow} - \rho_i^{\downarrow}}{\rho_i^{\uparrow} + \rho_i^{\downarrow}} \quad (1.8)$$

where $i = 1, 2$.

3.3 Tunnel magnetoresistance experiments

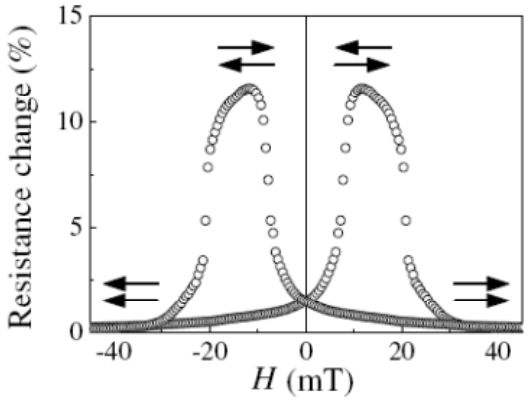

Figure 1.4. The first observation of reproducible, large, room temperature magnetoresistance in a CoFe/Al2O3/Co MTJ. The arrows indicate the relative magnetization orientation in the CoFe and Co layers. From [25].

In 1995, nearly 20 years after the original "discovery" of the TMR effect, Moodera et al. [25] reported the observation of large and reproducible TMR > 10% at room temperature in MTJ with Al_2O_3 tunnel barrier (Figure 1.4). This experiment demonstrated the fabrication procedure which provides MTJs with a pinhole-free tunnel barrier and with smooth interfaces. This achievement quickly garnered a great deal of attention, and catalyzed many groups to investigate

MTJs. MTJs can be used as non-volatile magnetic random access memories (MRAMs) [26], i.e. arrays of MTJs, have been commercialized since 2007. MRAM and sensor applications of MTJs require, in addition to high values of TMR, a reduced resistance–area (RA) product. Obviously, one expects the largest TMR values for ferromagnetic electrodes with the largest spin polarization. Materials with a spin polarization of 100% are called halfmetals [27]. MTJs based on half-metallic manganite electrodes such as $La_{2/3}Sr_{1/3}MnO_3$ (LSMO) or $La_{2/3}Ca_{1/3}MnO_3$ (LCMO) do exhibit TMR values of several hundred percent [28-32] corresponding within the Jullière model to *P*spin of up to 95% [30]. Importantly, the TMR of manganite-based MTJs is only large at low temperature and vanishingly small at 300K [33]. In 2001, theoretical calculations predicted that epitaxial MTJs with a crystalline magnesium oxide (MgO) tunnel barrier would have TMR ratios of over 1000%. The complex band structure produces that the majority-spin conductance dominates tunneling which leads to a very high TMR for thick enough barriers [34]. Experimentally, after the pioneering work of Bowen *et al.* [35] who reported a TMR of 60% in epitaxial Fe/MgO/Fe junctions, TMR values in excess of 200% were reported by Parkin *et al.* [36] and Yuasa *et al.* [37]. There have also been reports of very large TMR in Co/MgO/Co (410%) [38], CoFe/MgO/CoFe (290%) [36] and CoFeB/MgO/CoFeB (1144% at low temperature and 604% at room temperature) [39].

One of the important properties of MTJs, which affects strongly the SDT, is the chemical bonding at the ferromagnet/insulator interface. The bonding mechanism determines the effectiveness of transmission across the interface which can be different for electrons of different characters. Tsymbal and Pettifor [40] showed that for tunnelling from transition metal ferromagnets across a thin barrier layer, the spin polarization of the conductance depends strongly on the interfacial bonding between the ferromagnet and the insulator. For example, De Teresa et al. [41, 42] observed that the tunneling spin polarization depends explicitly on the insulating barrier used. They found that Co/Al_2O_3/LSMO MTJs gave a positive TMR for all biases, not surprising since both LSMO and the Co/Al_2O_3 interface are known to have positive polarizations. Surprisingly, $Co/SrTiO_3$/LSMO junctions showed *negative* TMR values at zero bias, and further displayed a strong bias dependence. They proposed that the polarization of the Co/SrTiO3 interface must be *negative* opposite to that of Co/Al2O3

interfaces. In order to show this more conclusively, De Teresa et al. investigated Co/ Al_2O_3/$SrTiO_3$/LSMO junctions, with the expectation that since the LSMO and Co/ Al_2O_3 tunneling spin polarizations are both positive, a normal positive TMR would result for all biases. Another remarkable result was reported by Yuasa et al. in 2002 [43]. They found quantum well oscillations of the TMR inserting ultrathin layers of single crystalline Cu interlayers in Co(001)/Cu(001)/Al_2O_3/$Ni_{80}Fe_{20}$ junctions. Increasing the number of non magnetic metal at the ferromagnetic electrode/insulate barrier TMR oscillates at the zero-bias with a period of 1.14 nm is in good agreement with the Fermi surface of Cu. As has be shown, the tunnel current depends sensitively on the density of states at the interface between the barrier and the electrodes, and can thus be used as a probe of the interfacial properties, so that tunnel junctions appear as very appropriate architectures to exploit novel interface effects in practical devices.

4 Basic Concepts. Ferroelectrics

4.1 Introduction

A ferroelectric is an insulating system with at least two stable or metastable states of spontaneous polarization (nonzero electric polarization in zero applied electric field). For a system to be considered ferroelectric, it must be possible to switch between these states with an applied electric field, the threshold field being designated the coercive field. The mechanism of switching is understood to take place on scales longer than unit-cell scale, and generally to require the growth and shrinking of domains through the motion of domain walls. The observation of an electric hysteresis loop is considered necessary to establish ferroelectricity. In its canonical form, the ferroelectric P-E hysteresis loop is symmetric and the remnant and coercive fields are easily defined and extracted (Fig 1.5).

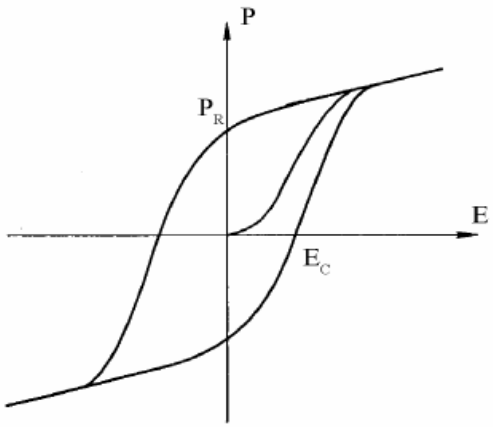

Figure 1.5. Ferroelectric hysteresis loop schematization [44]. P_R is the remanent polarization in the abscense of external electric field and E_C is the electric coercive field.

In all known ferroelectric crystals, the spontaneous polarization is produced by the atomic arrangement of ions in the crystal structure, depending on their positions, as in conventional ferroelectrics, or on charge ordering of multiple valences, as in electronic ferroelectrics. One condition that ensures the presence of discrete states of different polarization and enhances the possibility of switching between them with an accessible electric field is that the crystal structure can be obtained as a "small" symmetry-breaking distortion of a higher-symmetry reference state. This involves a polar displacement of the atoms in the unit cell. In most ferroelectrics, there is a phase transition from the ferroelectric state to a non polar paraelectric phase with increasing the temperature. The symmetry-breaking relation between the high-symmetry paraelectric structure and the ferroelectric structure is consistent with a second order transition. This analysis naturally leads to the prediction that the dielectric susceptibility diverges at the transition.

Devonshire was the first to applied Landau's symmetry-based treatment of phase transitions to the case of ferroelectrics [45- 47]. Bulk ferroelectrics systems can be specified by the temperature (T), the polarization (P), the electric field (E), the strain (η), and the stress (σ). We can define the free energy density of the system as

$$F_P = -E \cdot P\frac{1}{2}aP^2 + \frac{1}{4}bP^4 + \frac{1}{6}cP^6 + \cdots \quad (1.9)$$

The equilibrium configuration is determined by finding the minima of F_P, using

$$\frac{\partial F_P}{\partial P} = 0 \quad (1.10)$$

This equation gives us an expression for the electric field E as a function of the polarization

$$E = aP + bP^3 + cP^5 \quad (1.11)$$

In the Landau-Devonshire theory is assumed that near the Curie point ($T \sim T_C$)

$$a = \frac{1}{C}(T - T_C) \quad (1.12)$$

where C is the Curie constant. Given the equation

$$\chi = \frac{P}{E} = \frac{1}{a} \quad (1.13)$$

we can combine it with equation 1.12 and obtain the Curie-Weis law

$$\chi = \frac{C}{T - T_C} \quad (1.14)$$

The free energy as a function of polarization in the paraelectric state ($T >> T_c$) and in the ferroelectric state ($T << T_C$) is shown in figure 1.6.

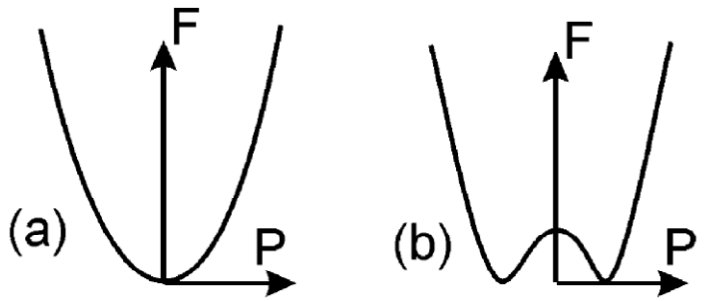

Figure 1.6. Free energy as a function of polarization in the paraelectric state (a), and in the ferroelectric state (b)

The sign of the coefficient b determines the nature of the paraelectric-ferroelectric transition. If $b > 0$ the polarization develops continuously in a second order transition, and if $b < 0$ the polarization develops discontinuously in a first order transition.

4.2 Ferroelectric Perovskite Oxides

The most studied family of ferroelectric oxides is that known as the perovskite oxides. This is a very large family of composition ABO_3, where A and B each represent a cation element or mixture of two or more such elements or vacancies (Figure 1.7 (a)). In order to exhibit a spontaneous electric polarization it must have a noncentrosymmetric arrangement of the constituent ions and their corresponding electrons. The noncentrosymmetric structure is reached by shifting either the A or B (or both) off center relative to the oxygen anions, and the spontaneous polarization derives largely from the electric dipole moment created by the shift (Figure 1.7 (b) and (c)). If the bonding in an ideal cubic perovskite were entirely ionic, and the ionic radii were of the correct size to ensure ideal packing, the structure would remain centrosymmetric, and therefore not ferroelectric. This is because, although long-range Coulomb forces favor the ferroelectric state, the short range repulsions between the electron clouds of adjacent ions are minimized for nonpolar, cubic structures [48, 49]. The existence or absence of ferroelectricity is determined by a balance between these short-range repulsions that favor the nonferroelctric symmetry structure and additional

bonding considerations which act to stabilize the distortions necessary for the ferroelectric phase [50]. The changes in chemical bonding that stabilize distorted structures have long been recognized in the field of coordination chemistry, and are classified as second-order Jahn Teller effects [51-53], or sometimes pseudo Jahn-Teller effects [54]. One of the ferroelectric distortions is the ligand-field stabilization of the B-site transition metal cation by its surrounding anions, as occurs, for example, at the Ti site in $BaTiO_3$. Here the centrosymmetric, formally d^0 transition metal mixed oxygen p character as it displaces towards an oxygen ion or group of ions [55] causing an energy-lowering rehybridation.

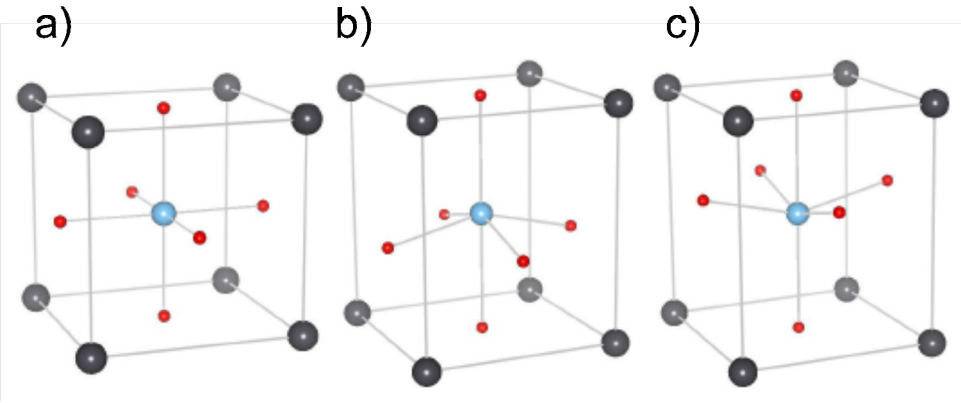

Figure 1.7. Crystal structure of the perovskite ABO_3 (A = black, B= blue, and O = red) in the (a) paraelectric cubic phase, and (b) and (c) in the ferroelectric tetragonal phases for the polarization pointing upward (b) and downward (c) . Adapted from [56].

4.3 Size Effects

In many cases, and especially in the past, samples below a certain size did not display ferroelectricity, not because intrinsic size effect had suppressed it but rather due to the difficulties in fabrication. The fact that the experimentally obtained minimum thickness for a ferroelectrics thin film has decreased by orders of magnitude over the years is a clear sign that for the most part the suppression was due to the limitations on sample quality. For example dead layers, grain boundaries and defects such as oxygen vacancies are all known to have strong influences on ferroelectric properties. In recent years, a degree of maturity in materials-processing techniques was reached, allowing fundamental size effects to be experimentally probed. The predominant role of electrostatic boundary

conditions is controlling ferroelectricity in very thin-films has now been demonstrated from first principles [57-59], but in fact the idea of imperfect screening has considerable history; in the 1970s [60-61] researchers at IBM studied the effect that a finite screening length for the electrodes would have on the critical thickness of films within the framework of the Ginzburg-Landau-Devonshire theory.

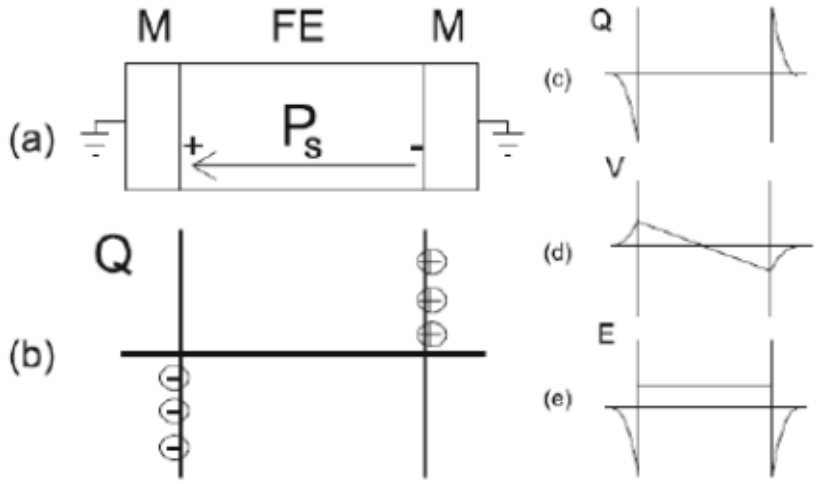

Figure 1.8. Schematic representation of a short-circuited metal/ferroelectric/metal capacitor with the ferroelectric film homogeneously polarized with spontaneous polarization P_s. (b) Schematic representation of the associated charge distribution in the presence of perfect electrodes. (c) Charge distribution, (d) voltage and (e) field profiles in the presence of realistic electrodes. From Dawber et al. [62].

In an idealized ferroelectric capacitor where the metal electrodes are perfect conductors the screening charges are only located at the metal/ferroelectric interface, compensating the ferroelectric polarization surface charges. However, in the realistic electrodes the screening charges are distributed over a small length in the metal. This spatial extension is the effective Thomas Fermi screening length λ_{eff}. This spatial charge distribution creates finite dipoles at the interfaces and leads to an associated voltage drops

$$\Delta V = \frac{\lambda_{eff}}{\epsilon_0} P \tag{1.15}$$

where P is the ferroelectric polarization and ε_0 is the electric permittivity. A compensating depolarizing field across the ferroelectric film is necessary to ensure that the short-circuited ferroelectric capacitor is equipotential [60]. This depolarizing field is then

$$E_d = -2\frac{\lambda_{eff}}{d\epsilon_0}P \tag{1.16}$$

where d is the ferroelectric film thickness. E_d increases as the sample thickness is decreased. With ferroelectric film thickness reaching the range of the Thomas-Fermi effective screening length, polarization instability, therefore metal with small λ_{eff} would screen better the surface charges leading to a more stable ferroelectric phase. In Figure 1.8 is shown the schematic representation of this charge distribution (c), voltage drop (d) and electric field (e) for a ferroelectric capacitor with realistic electrodes. The electrode/ferroelectric/electrode system is a straightforward model to illustrate the concepts of screening length and depolarizing field. However, in realistic systems, other screening mechanisms have to be considered. For example the screening by mobile charges inside the ferroelectric layer as a result of doping is possible. In $BaTiO_3$ oxygen vacancies generate free electrons via the reaction equation [63]

$$O_o \rightarrow \frac{1}{2}O_2 + V_o^{\cdot\cdot} + 2e^- \tag{1.17}$$

These carriers, which screen the polarization-induced charges, strongly influence the electrostatic boundary conditions and may favor one ferroelectric polarization over the other. These oxygen vacancies also play a role in pinning the domain walls during the fatigue process due to their ordering [64]. Another important screening mechanism is the penetration of the polarization distortion into the metal. It is easy to imagine in metallic transition metal oxide electrodes due to their ionic structure. If the ionic displacements associated with the polarization continue into the metal, then those long-range electrostatic effects associated with a nearby-electrode suppression of polarization are heavily reduced for this type of system. In other words the ionic polarizability of the nearby-interfacial layers of the electrode could stabilize the ferroelectric phase [65]. It has been also demonstrated in ultrathin ferroelectric films the big influenced of the chemical

bonds at the ferroelectric/metal interfaces [66]. For example the interfacial termination in metal/ferroelectric of a complex oxide system can leads to an interfacial dipole which can pin the ferroelectric polarization at the interface [67] producing a detrimental of the ferroelectric instability. There are also other ways to reduce the depolarization field, like the formation of a ferroelectric domain structure [68,69], or increasing the material tetragonallity by strain engineering which could increases the ferroelectric properties in perovskite oxides [70].

5 Thesis Outline

- Chapter 2: in this chapter the experimental techniques that are used throughout the thesis comprehending: x-ray diffraction, scanning and transmission electron microscopy and atomic force microscopy to structural characterization; vibrating sample magnetometry for magnetic characterization; piezoresponse force microscopy to nanoscale-ferroelectric characterization; polarized neutron reflectometry and x-ray magnetic circular dichroism for studying the details on bulk and interfacial magnetic profile. We also give details of the sample growth method and of the tunnel junction patterning process.

- Chapter 3: In this chapter we characterize the structural properties of $La_{0.7}Sr_{0.3}MnO_3/BaTiO_3$ epitaxial heterostructures. We study the magnetic properties of these samples and we discuss their ability for use them as magnetic tunnel junctions. We demonstrate ferroelectricity in a few nanometers thick $BaTiO_3$ films grown on $La_{0.7}Sr_{0.3}MnO_3$ buffered layer.

- Chapter 4: we analyze the magnetotransport properties of $La_{0.7}Sr_{0.3}MnO_3/BaTiO_3/La_{0.7}Sr_{0.3}MnO_3$ magnetic tunnel junctions. We discuss the possibility of Coulomb blockade charging effect and an induced magnetic moment in the $BaTiO_3$ tunnel barrier by the presence of oxygen vacancies at $La_{0.7}Sr_{0.3}MnO_3/BaTiO_3$ bottom interface.

- Chapter 5: we analyze the effect of the $BaTiO_3$ ferroelectric polarization in the spin dependent transport of $La_{0.7}Sr_{0.3}MnO_3/BaTiO_3/La_{0.7}Sr_{0.3}MnO_3$ magnetic tunnel junctions. We find unexpected results such tunnel electro resistance values and a modulation of the tunnel magnetoresistance amplitude. We discuss a possible scenario were interfacial charge density is modulated by the ferroelectric polarization reversal producing changes in the effective tunnel barrier width. It is also discussed the control of the spin filtering effect produced by the Ti induced magnetic moment effect by this charge density modulation.

- Chapter 6 summarizes the main conclusions of this work.

6 References

[1] M. Imada, A. Fujimori, and Y. Tokura, *Rev. Mod. Phys.***70** 1039 (1998).

[2] S. Maekawa, T. Tohyama, S.E. Barnes, S. Ishihara, W. Koshibae and G Khaliullin, Physics of Transition Metal Oxides (Springer, 2004), chap. 1

[3] E. Dagotto, *Science* **309** 257 (2005).

[4] E. Dagotto and Y. Tokura, *MRS Bull.* **33** 1037 (2008).

[5] J. Mannhart and D. G. Schlom, *Science* **327** 1607 (2010).

[6] H. Y. Hwang, Y. Iwasa, M. Kawasaki, B. Keimer, N. Nagaosa, and Y. Tokura, *Nature Mater.* **11**, 103 (2012).

[7] S. Okamoto, and A. Millis, *Nature* **428** 630 (2004).

[8] M. Fiebig, *J. Phys. D: Appl. Phys*. **38**, R123 (2005).

[9] W. Eerenstein, N. D. Mathur, and J. F. Scott, *Nature* **442**, 759 (2006).

[10] R. Ramesh, and N. A. Spaldin, *Nat. Mater*. **6**, 21 (2007).

[11] J. M. Rondinelli, M. Stengel, and N. A. Spaldin, *Nat. Nanotechnol*. **3**, 46 (2008).

[12] Y.-H. Chu, L. W. Martin, M. B. Holcomb, M. Gajek, S.-J. Han, Q. He, N. Balke, C.-H. Yang, D. Lee, W. Hu, Q. Zhan, P.-L. Yang, A. Fraile-Rodrıguez, A. Scholl, S. X. Wang, and R. Ramesh, *Nat. Mater*. **7**, 478 (2008).

[13] M. Y. Zhuravlev, S. S. Jaswal, E. Y. Tsymbal, and R. F. Sabirianov, *Appl. Phys. Lett.,* **87** , 222114 (2005).

[14] M. Y. Zhuravlev, S. Maekawa, and E. Y. Tsymbal, *Phys. Rev. B* **81** , 104419 (2010).

[15] J. P. Velev, C.-G. Duan, J. D. Burton, A. Smogunov, M. K. Niranjan, E. Tosatti, S. S. Jaswal, and E. Y. Tsymbal, Nano Lett. **9**, 427–432 (2009).

[16] V. Garcia, M. Bibes, L. Bocher, S. Valencia, F. Kronast, A. Crassous, X. Moya, S. Enouz-Vedrenne, A. Gloter, D. Imhoff, C. Deranlot, N. D. Mathur, S. Fusil, K. Bouzehouane, and A. Barthélémy, *Science* **327**, 1106-1110 (2010).

[17] D. Pantel, S. Goetze, D. Hesse, and M. Alexe, *Nature Mater.* **11**, 289 (2012).

[18] J. Bland, and B. Heinrich, Ultrathin Magnetic Structures III: Fundamentals of Nanomagnetism (Springer Verlag, 2005).

[19] J. G. Simmons, *J. Appl. Phys*. **34**, 1793 (1963).

[20] W. A. Harrison, *Phys. Rev.* **123**, 85 (1961).

[21] J. Bardeen, Phys. Rev. Lett. **6**, 57 (1961).

[22] S. Zhang, and P. Levy, Eur. Phys. J. B **10**, 599 (1999).

[23] W. F. Brinkman, R. C. Dynes, and J. M. Rowell, *J. Appl. Phys.* **41**, 1915 (1970).

[24] M. Jullière, *Physics Letters A* **54**, 225 (1975)

[25] J. S. Moodera, L. R. Kinder, T. M. Wong, and R. Meservey, *Phys. Rev. Lett.* **74**, 3273 (1995).

[26] W. J. Gallagher, and S. S. P. Parkin, *IBM J. Res. Dev*. **50,** 5–23 (2006).

[27] R. A. de Groot, F. M. Mueller, P. G. van Engen, and K. H. J. Buschow, *Phys. Rev. Lett.* **50,** 2024 (1983).

[28] M. H. Jo, N. D. Mathur, N. K. Todd, and M.G. Blamire, *Phys. Rev. B* **61**, R14905 (2000).

[29] J. O'Donnell, A.E. Andrus, S. Oh, E.V. Colla, and J. N. Eckstein, *Appl. Phys. Lett.* **76**, 1914 (2000).

[30] M. Bowen, M. Bibes, A. Barthélémy, J. P. Contour, A. Anane, Y. Lemaître, and A. Fert, *Appl. Phys Lett*. **82**, 233 (2003).

[31] Y. Ishii, H. Yamada, H. Sato, H. Akoh, Y. Ogawa, M. Kawasaki, and Y. Tokura, *Appl. Phys. Lett*. **89**, 042509 (2006).

[32] E. T. Wertz, and Q. Li, *Appl. Phys. Lett*. **90**, 142506 (2007).

[33] V. Garcia, M. Bibes, A. Barthélémy, M. Bowen, E. Jacquet, J.P. Contour, and A. Fert, *Phys. Rev. B,* **69**, 052403 (2004).

[34] J. Mathon, and A. Umerski, *Phys. Rev.* B **63**, 220403 (2001).

[35] M. Bowen, V. Cros, F. Petroff, A. Fert, C. Mantínez Boubeta, J. L. Costa-Krämer, J. V. Anguita, A. Cebollada, F. Briones, J. M. de Teresa, L. Morellòn, M.R. Ibarra, F. Güell, F. Peirò, and A. Corret, *Appl. Phys. Lett*. **79**, 1655 (2001).

[36] S. S. P. Parkin, C. Kaiser, A. Panchula, P.M. Rice, B. Hughes, M. Samant, and S.-H. Yang, Nature Mater. **3**, 862 (2004).

[37] S. Yuasa, T. Nagahama, A. Fukushima, Y. Suzuki, and K. Ando, Nature Mater. **3**, 868 (2004).

[38] S. Yuasa, A. Fukushima, H. Kubota, Y. Suzuki, and K. Ando, *Appl. Phys. Lett.* **89**, 042505 (2006).

[39] S. Ikeda, J. Hayakawa, Y. Ashizawa, Y. Lee, K. Miura, H. Hasegawa, M. Tsunoda, F. Matsukura, and H. Ohno, *Appl. Phys. Lett*. **93**, 082508 (2008).

[40] E. Y. Tsymbal, and D. G. Pettifor, *J. Phys.: Condens. Matter* **9**, L411 (1997).

[41] J. M. De Teresa, A. Barthélémy, A. Fert, J. P. Contour, R. Lyonnet, F. Montaigne, P. Seneor, and A. Vaurès, *Phys. Rev. Lett*. **82**, 4288 (1999).

[42] J. M. De Teresa, A. Barthélémy, A. Fert, J. P. Contour, F. Montaigne, and P. Seneor, *Science* **286**, 507 (1999).

[43] S. Yuasa , T. Nagahama, and Y. Suzuki, *Science* **297** 234 (2002).

[44] F. Jona, and G. Shirane, Ferroelectric crystals (Clarendon Press 1962).

[45] A. F. Devonshire, *Philos. Mag*. **40**, 1040 (1949).

[46] A. F. Devonshire, *Philos. Mag.* **42**, 1065 (1951).

[47] A. F. Devonshire, *Adv. Phys.* **3**, 85 (1954).

[48] R. E. Cohen, *Nature* **358**, 136 (1992).

[49] R. E. Cohen, *J. Phys. Chem. Solids,* **61**, 139 (2000).

[50] H. D. Megaw, Acta Crystallgr. **5**, 739 (1952).

[51]P. S. Halasyamani and K. R. Poeppelmeier, *Chem. Mater.* **10**, 2753 (1998).

[52] U. Opik, and M. L. H. Pryce, *Proc, RoySoc. A* **238**, 425 (1957).

[53] R. F. W. Bader, *Mol. Phys.* **3**, 137 (1960).

[54] I. B. Bersuker, *Chem. Rev*. **101**, 1067 (2001).

[55] A. Filipetti, and N. A. Hill, *Phys Rev. B* **65**, 195120 (2002).

[56] C. Ahn, K. M. Rabe, and J. M. Triscone, *Science* **303**, 488 (2004).

[57] P. Ghosez, and K. M. Rabe, *Appl. Phys. Lett*. **76**, 2767 (2000).

[58] B. Meyer, and D. Vanderbilt, *Phys. Rev. B* **63**, 205426 (2001).

[59] J. Junquera, and P. Ghosez, *Nature (London)* **422**, 506 (2003).

[60] R. R. Mehta, B. D. Silverman, and J. T. Jacobs, *J. Appl. Phys*. **44**, 3379 (1973).

[61] I. P. Batra, P. Wurfel, and B. D. Silverman, *J. Vac. Sci. Technol*. **10**, 687 (1973).

[62] M. Dawber, P. Chandra, P. B. Littlewood, and J. F. Scott, *J. Phys. Condens. Matter* **15,** L393 (2003).

[63] R. Moos and K. H. Hardtl, *J. Am. Ceram. Soc*. **80**, 2549 (1997).

[64] M. Dawber, K. M. Rabe, and J. F. Scott *Rev. Mod. Phys*. **77**, 1083 (2005).

[65] G. Gerra, A. K. Tagantsev, N. Setter, and K. Parlinski, *Phys. Rev. Lett.* **96,** 107603 (2006).

[66] M. Stengel, D. Vanderbilt, and N. A. Spaldin, *Nature. Mater.* **8**, 392 (2009).

[67] X. Liu, Y. Wang, P. V. Lukashev, J. D. Burton, and E. Y. Tsymbal, *Phys Rev. B* **85**, 125407 (2012).

[68] S. K. Streiffer, J. A. Eastman, D. D. Fong, C. Thompson, A. Munkholm, M. V. Ramana Murty, O. Auciello, G. R. Bai, and G. B. Stephenson, *Phys. Rev. Lett.* **89**, 067601 (2002).

[69] D. D. Fong, G. B. Stephenson, S. K. Streiffer, J. A. Eastman, O. Auciello, P. H. Fuoss, and C. Thompson, *Science* **304**, 1650 (2004).

[70] K. J. Choi, M. Biegalski, Y. L. Li A Sharan, J. Schubert, R. Uecker, P. Reiche, Y. B. Chen, X. Q. Pan, V. Gopalan, L.-Q. Chen, D. G. Schlom, and C. B. Eom, *Science* **306**, 1005 (2004).

2 Experimental Techniques

1 Sample preparation

Samples are prepared by sputter deposition in high O_2 pressure. This method is based on the ballistic impact of atoms against a substrate after being removed from a material source. The sputtered ions come from targets made of the stoichiometric compound while the oxygen plays the role of the sputtering element. In our case the substrate is placed on a heater plate below the targets. The growth takes place inside a chamber in which a high vacuum of about 10^{-6} mbar is previously realized. The chamber, shown in Figure 2.1, is connected to a turbo-molecular pump supported by a membrane pump. A constant oxygen flow is injected and controlled by a system of needle valves. Since the sputter yield depends on the energy of the incoming O_2 ion and the source atom species, the material removed from the target will deposit on the substrate in a manner which strongly depends on several controllable parameters such as the temperature of the substrate, the applied radio frequency power and the pressure inside the chamber. In order to grow epitaxial oxide heterostructures high temperature and pressure are usually required. All the samples studied in this work have been grown on $SrTiO_3$ substrate (100)-oriented. The high oxygen pressure (3.2 mbar) applied during the deposition, favors a complete thermalization of the extracted species and at the same time prevents them from back-sputtering and loss of

oxygen in the final crystal structure. The substrate temperature is kept at 900ºC. Under these conditions the deposition rate is slow (0.3nm/min) and ensures the epitaxial growth of the sample. To preserve the optimal oxygen content of the structure an *in-situ* annealing at 900 mbar O_2 pressure is necessary. The chamber is oxygenated at 800ºC and the annealing is made at 750ºC during 1hour.

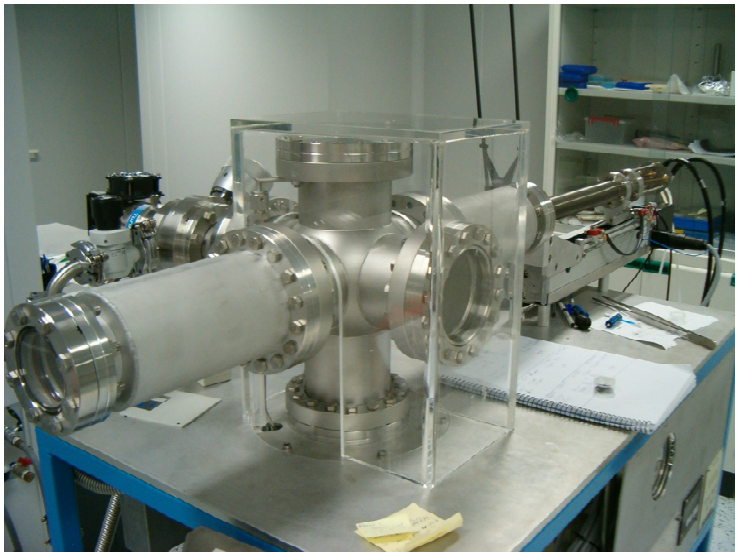

Figure 2.1. View of the sputtering chamber. The targets are mounted on a remote controlled arm to switch between the different materials.

2 Structural characterization: XRR, XRD

X-ray reflectivity (XRR) and diffraction (XRD) patterns allowed determining the thickness and the structural quality of our samples. XRR and XRD measurements have been carried out at CAI de Difracción de Rayos-X (UCM), with a Philips X'pert MRD diffractometer, using a Cu tube as X-ray source (λ_x= 0.15418nm) operating at 45kV an 40mA.

2.1 X-ray reflectivity

The coherent and collimated radiation coming from an X-ray source is reflected at the interface between layers with different electronic densities (the

substrate, the film, the air). The different refractive indexes induce a change in the path length of the X-ray and consequently a constructive/destructive interference of the different reflected beams. In an analogous way, the interference resulting from a layered structure produces oscillation in the reflectivity pattern. This pattern is obtained by measuring the reflected intensity as a function of the incident angle (2θ) through a detector which is set in θ-2θ (Bragg) geometry with respect to the source (see Figure 2.2).

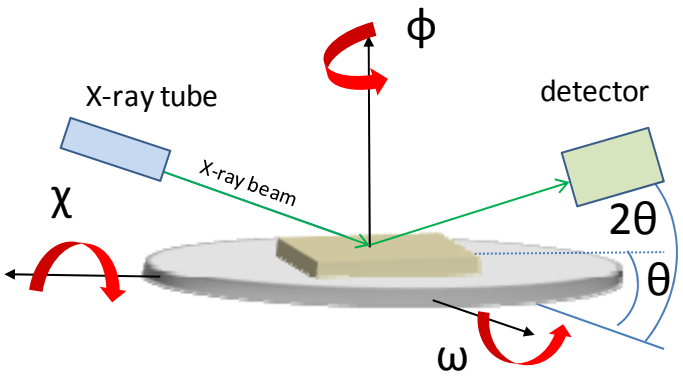

Figure 2.2. Schematic diagram of the θ-2θ geometry

Reflectivity scans showed in this work are usually taken up to an angle of 2θ~10 degrees. In this range of angle we are able to see finite size oscillations (2θ < 7º), related to the total thickness of the sample as shown in Figure 2.3. The period of the finite size oscillations is inversely related to the thickness d of the whole sample. By indexing the position of the maxima and minima (m=1,2..) we can calculate the total thickness using the formula:

$$sin^2\theta = \left[\frac{(m-k)\lambda_x}{2d}\right] + 2\delta \qquad (2.1)$$

where k=0 correspond to a minimum, k=1/2 to a maximum and δ is the real part of the refraction index:

$$n = 1 - \frac{\rho_n r_e \lambda_x}{2\pi}(f_0 + \Delta f' - i\Delta f'') = 1 - \delta + i\beta, \quad (2.2)$$

where ρ_n is the electronic density, r_e is the electron radius, f_0 is the atomic dispersion factor, *Δf'* and *Δf''* are corrections due to the anomalous dispersion [1, 2]. In Figure 2.3 we show a representative reflectivity curve of a thin film.

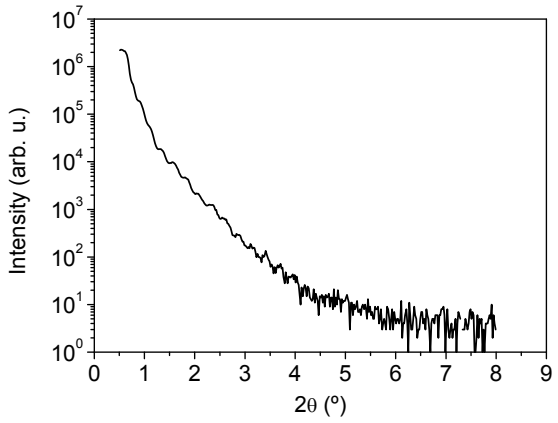

Figure 2.3. Reflectometry scan from a $La_{0.7}Sr_{0.3}MnO_3$ 25 nm / $BaTiO_3$ 4.4 nm/ $La_{0.7}Sr_{0.3}MnO_3$ 7 nm thin film.

2.2 X ray diffraction

Atomic layers in a crystal are separated by a distance *d*. Specular reflected X-rays will travel different distances due to this separation and will yield constructive interference if the difference in path is an integer multiple of the X-ray wavelength. For an epitaxial structure of different materials, a diffraction scan carried out in *θ-2θ* geometry, after optimizing around one of the (00*l*) diffraction peaks of the substrate will show only the Bragg peaks of the same family [3]. Thus the diffraction condition described by the Bragg law:

$$2d_{hkl}sin\theta = n\lambda_x \quad (2.3)$$

can be used for determining the lattice spacing of a set of crystallographic planes, parallel to the film plane, we will usually call this distance the lattice parameter c.

In Figure 2.4 (a) we can see a diffraction scan from a [BTO 4.4 nm / LSMO 7 nm] thin film grown on STO substrate where the diffraction peaks are labeled. In the case of multilayers the characteristic length scales are: the lattice spacing of the constituent material, and the modulation wavelength Λ defined as the thickness of the bilayer that is repeated to form the superlattice. This additional periodicity will cause new diffraction peaks to appear which can be indexed about the average lattice constant $\bar{d}$ following [4].

$$2\frac{sin\theta}{\lambda_x} = \frac{1}{\bar{d}} \mp \frac{m}{\Lambda}, \tag{2.4}$$

where m is an integer that labels the order of the satellite around the main Bragg peak and $\bar{d} = {\Lambda}/{(N_A + N_B)}$, where N_A and N_B are the number of atomic planes of material A and B in one bilayer. In Figure 2.4 (b) we show the diffraction spectra of a $[LSMO_{27\ \mathbf{u.c.}}/BTO_{17\ \mathbf{u.c.}}]_{\mathbf{x4}}$ superlattice were the superlattice Bragg peaks (labeled as 0) and the superlattice satellite peaks are labeled according to equation 2.4.

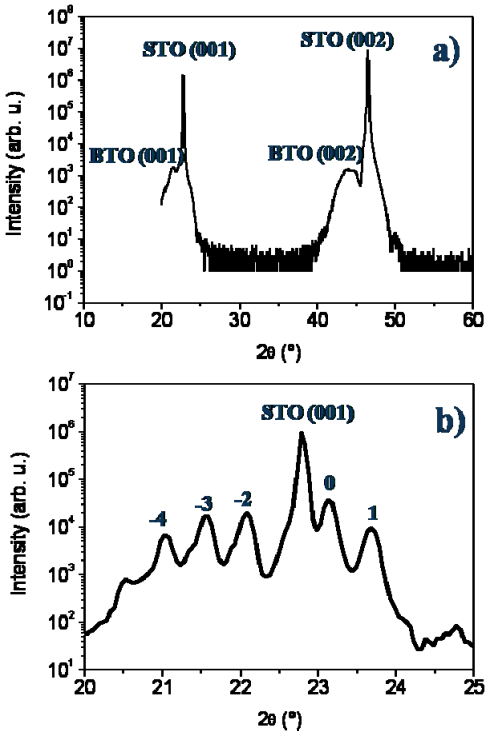

Figure 2.4. X-ray diffraction spectra of a (a) [$BTO_{11\ u.c.}$ /$LSMO_{18\ u.c.}$] bilayer and of a (b) [$LSMO_{27\ u.c.}$/$BTO_{17\ u.c.}$]$_{x4}$ superlattice grown on STO (001) substrate.

3 Scanning Transmission Electron Microscopy

A scanning transmission electron microscope (STEM) is a powerful technique to provide two-dimensional maps revealing atomic and electronic structure of complex oxide with sub-Ångstrom spatial resolution and sub-eV energy resolution. All the STEM measurements in this thesis were done at the S. J. Pennycook group (STEM Group) of the Oak Ridge National Laboratory by Gabriel Sánchez-Santolino and Maria Varela.

In the scanning-transmission electron microscope (see Figure 2.5), a field-emission source and strong electromagnetic lenses are used to form a small probe that can be raster-scanned across the specimen [5]. Images are obtained

serially as the probe is scanned pixel-by-pixel using a number of detectors with different geometries. The key advantage of STEM is the ability to detect multiple signals simultaneously.

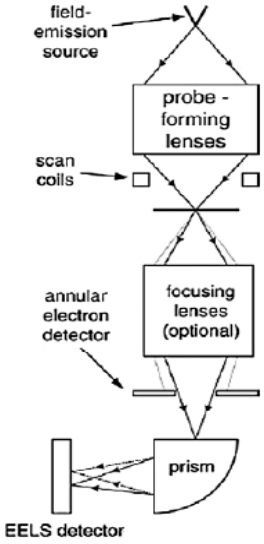

Figure 2.5. Schematic of a scanning-transmission electron microscopy system. From ref [5]

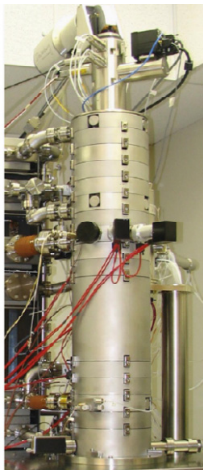

Figure **¡Error! No hay texto con el estilo especificado en el documento.**2.6. Photograph of a NION ULTRASTEM column [6].

The high angle annular dark field (HAADF) detector is normally used for Z-contrast imaging. A dark-field image, representing transmitted electrons scattered through relatively large angles, is formed by feeding the signal from a ring-shaped (annular) detector to a display device scanned in synchronism with the probe scan (Figure 2.7). Alternatively, the whole spectrum is read out at each probe position (pixel), resulting in a large spectrum-image data set that can be processed off-line [7]. The dark field image was collected over a wide range of scattering angles and showed strong atomic number contrast. The fact that the Z-contrast images are directly interpretable makes this technique very appealing. For higher collection efficiency a lower angle ADF detector can be used to improve signal-to-noise ratio (Figure 2.7 (right)).

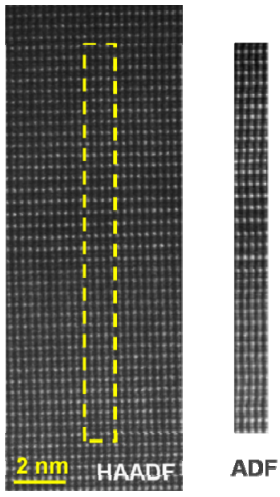

Figure 2.7. (left) High magnification HAADF image of a LSMO/BTO heterostructure. (right) Simultaneous annular dark field ADF image. It is shown that the ADF image the atoms (bright circles) are slightly brighter.

Bright field image (Figure 2.8) shows the usual characteristics of an interference or phase contrast image [8-10]. Light atoms scatter much less than heavy atoms and have usually been invisible in a Z-contrast image until aberration corrected. Recently an annular bright field mode has been shown to give less Z-contrast image [11, 12]. The reduced Z dependence means light elements are easier to see in the image.

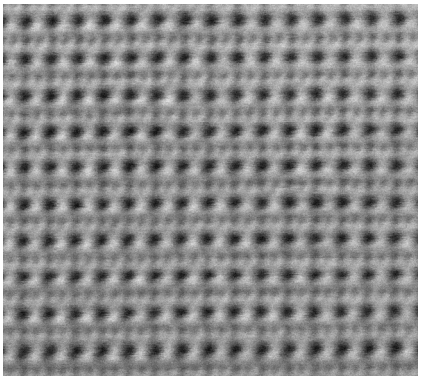

Figure 2.8. Annular bright field image of a LSMO/BTO heterostructure. In ABF the atoms positions are represented for the dark cicles (no counts in the detector). Lights atoms like oxygen is clearly shown.

The Z- contrast image also enabled atomic resolution EELS [13-14] by providing an unambiguous signal that allowed the probe to be located over a specific atomic column or plane. EELS is formally equivalent to X-ray absortion spectroscopy. Electrons scattered through smaller angles enter a single prism spectrometer, which produces an energy-loss spectrum (EELS spectrum) for a given position of the probe on the specimen [15]. With modern microscopes it is possible to obtain an EELS spectrum in each atomic column (Figure 2.9); this makes this technique a powerful tool to investigate the chemical composition of interfaces. EELS provides difference in termination or interdiffusion between different interfaces of an oxide thin film or multilayer. The high energy resolution of this technique also allows the study of the fine structure in the absorption edges which permits study electronic properties as oxidation state in transition metals. EELS edges are a result of the excitations of inner shell electrons into occupied levels above the Fermi level. Therefore, the EELS fine structure ensues directly as a result of the material's unoccupied density of states and they can be used to probe electronic properties when core electrons are excited. In complex oxides, properties such as the transition metal oxidation state can be measured from the EELS fine structure of the transition metal $L_{2,3}$ edge and the O K edge [16-18].

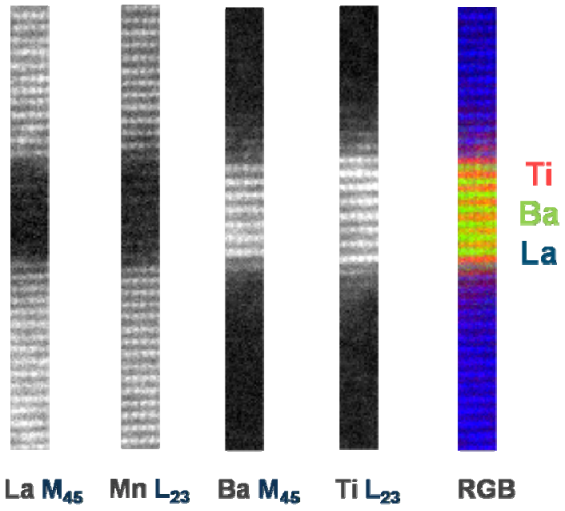

Figure 2.9. (from left to the right) Atomic elemental maps corresponding to the La $M_{4,5}$, Mn $L_{2,3}$, Ba $M_{4,5}$, Ti $L_{2,3}$ signal and false color image where three atomic resolution images have been overlayed: a Ti $L_{2,3}$ image in red, a La $M_{4,5}$ image in blue, and Ba $M_{4,5}$ image in green (RGB).

4 Vibrating sample magnetometry

We performed magnetic measurements using a Vibrating Sample Magnetometer (VSM). The VSM measures the difference in magnetic induction between region of space with and without the specimen. It therefore gives a direct and absolute measure of the magnetization. The magnetic moment of the sample is measured according to Faraday's law. The sample oscillates sinusoidally inside a small pick-up coil with a frequency of about 40Hz. The induced voltage due to $E = - d\varphi/dt$ is detected with the lock-in technique and converted to magnetic moment with an instrument specific calibration factor. It allows for the rapid measurement of M vs. T and M vs. H data with a useful sensitivity of approx. 10^{-6} emu. The sample is mounted on a diamagnetic stick fixed to a carbon rod (see Figure 2.10). All of the VSM measurements shown in this thesis were done on a Quantum Design physical properties measurement system (PPMS). The VSM measurements were done at the Mar García-Hernández group by N. M. Nemes. and A. Alberca.

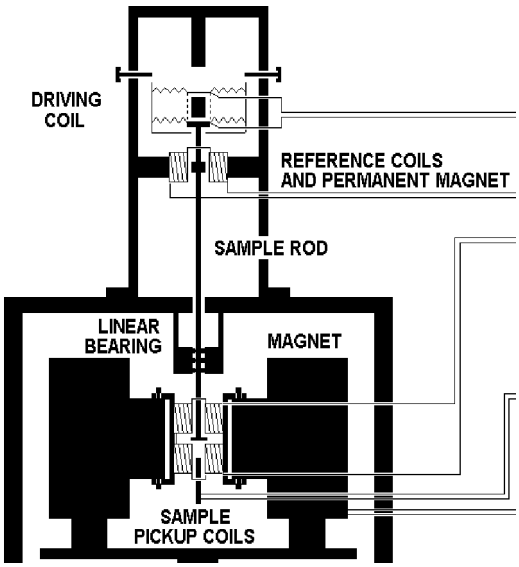

Figure 2.10. Diagrams of a VSM magnetometer.

5 Scanning Probe Microscopy

All the scanning probe microscopy measurements of this thesis were done at the M. García-Hernández group of the Instituto de Ciencia de Materiales de Madrid by C. Munuera.

5.1 Atomic Force Microscopy. Topography

Atomic force microscopy AFM is currently the most broadly employed tool in the scanning probe microscopy (SPM) family. Moreover, the measurements are performed at normal (ambient) temperature and pressure, thus not requiring special environmental conditions. Its resolution in the vertical direction is of the order of subnanometer, while the lateral is limited by the tip radius of curvature, in the order of few tens of nanometers. AFM is based on a probe, constituted by a sharp tip at the end of a flexible cantilever. The tip has the height of the order of micrometers and a radius of curvature of generally 10-20 nm. Upon proximity to a surface, the cantilever reacts to the forces between the

tip and the investigated surface, deflecting in first approximation according to Hooke's law. Various kinds of atomic forces are involved in such interaction, among which the Van der Waals force is the dominant one. By scanning the tip over the surface under investigation, the cantilever reacts to the topography of the sample. A feedback loop monitoring the cantilever's deflection keeps either the tip at a constant distance to the surface or the contact force constant (depending by the scanning mode employed) by moving the probe downwards or upwards. Such movement gives the topography of the scanned surface. The deflection of the cantilever is measured by the so-called optical lever mode. A laser light form a solid state diode is reflected off the back of the cantilever and collected by a photodetector. This consists of closely spaced photodiodes whose output signal is collected by a differential amplifier. Angular displacement of cantilever results in one photodiode collecting more light than the other photodiode, producing an output signal. Therefore the detector keeps track of the cantilever's deflection.

The most widely employed AFM mode for topography imaging is the tapping. This mode operates by scanning the probe across the sample surface, while the cantilever is oscillated. The cantilever oscillates at or near its resonance frequency with amplitude ranging typically from 10 nm to 100nm. Variations in the tip-surface average distance make the oscillation amplitude to change. The feedback loop monitors the root mean square (RMS) of the oscillation, acquired by the photodetector and keeps it constant at the setpoint value by vertical movements of the scanner.

5.2 Piezoresponse Force Microscopy

Piezoresponse Force Microscopy (PFM) is an extension of the AFM contact mode, and it is based on converse piezoelectric effect. In contact mode the probe is brought towards the surface. The feedback loop regulates the vertical position in a way to maintain the deflection constant to the setpoint. Using the tip as top electrode, an electric field can be applied on the studied sample. Because all ferroelectrics materials are piezoelectric, they change their sizes in response to the applied field. In PFM is used an alternating voltage $V = V_0 \sin(\omega t)$ combined with lock-in techniques. The modulation voltage generates an

alternating field across the sample, which makes it to oscillate. The phase of such oscillations depends on the polarization direction inside the sample (Figure 2.11). The piezoelectric oscillation is extracted from the overall signal using a lock-in amplifier. The signal extracted is referred as piezoresponse signal [19] and is composed by phase and amplitude

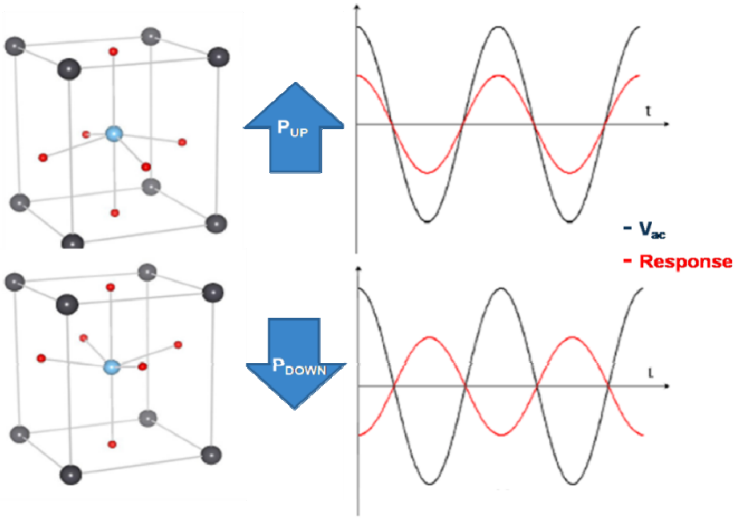

Figure 2.11. Alternating voltage applied to the PFM tip (black curve) and the signal response signal of the studied sample (red) for the two ferroelectric polarization direction, upward (top) and downward (bottom)

To demonstrate ferroelectricity in a nanoscale thn film a piezoelectric hysteresis loop is needed to be measured. Hysteresis loops are obtained by sweeping the DC voltage, and measuring piezoresponse at each voltage value. The DC voltage is ramped in steps. After the voltage pulse the system is given a time to stabilize and then the piezoresponse is measured [20]. In figure 2.12 is shown a phase (top) and amplitude (bottom) piezoresponse signal from a 12 nm $BaTiO_3$ ultrathin film grow on a 15 nm $La_{0.7}Sr_{0.3}MnO_3$ buffered layer grown on a $SrTiO_3$ (100) substrate.

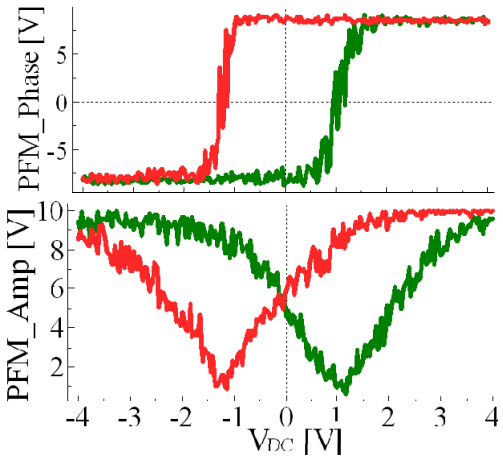

Figure 2.12. PFM phase (top) and amplitude (bottom) hysteresis loop for a 12 nm $BaTiO_3$ thin film grow on a 15 nm $La_{0.7}Sr_{0.3}MnO_3$ buffered layer grown on a SrTiO3 (100) substrate.

6 X-ray Magnetic Circular Dichroism (XMCD)

X-ray magnetic circular dichroism (XMCD) spectroscopy makes use of high energy X-rays to explore the structural and magnetic properties of matter. It was first suggested by Erskine and Stern [21] and pioneered by Schütz et al. [22]. It has several capabilities not afforded by traditional magnetic techniques. Its foremost strengths are the element-specific, quantitative determination of spin and orbital magnetic moments and their anisotropies. An XMCD experiment usually consists of illuminating the sample with intense circularly polarized X-rays produced in synchrotron sources and tuning the X-ray energy on the absorption edge of a specific element. The difference between left and right circularly polarized X-ray absorption cross section (the dichroism signal) of a ferromagnetic or a ferrimagnetic material is directly proportional to the mean value of the macroscopic magnetic moment.

6.1 X-ray absorption spectroscopy (XAS): chemical environment

X-ray absorption spectroscopy (XAS) studies the effect of photon absorption on the matter. It is not necessarily dependent on the incident photon

spin. In X-ray absorption a photon is absorbed by an atom giving rise to a transition of an electron (a photoelectron) from a core state to an empty state above the Fermi level. The absorption cross-section depends on the energy and on the measured element. To excite an electron in a given core level, the photon energy has to be equal or higher than the energy of this core level which is characteristics of the element [23]. When this energy level is crossed, a sudden jump in the absorption intensity is observed (Figure 2.13). Excitation of photoelectrons gives rise to the creation of core holes. These vacancies present an unstable condition for the atom. As the atom returns to its stable condition, electrons from the outer shells are transferred to the inner shells giving off, during the process, a characteristic X-ray whose energy is the difference between the two binding energies of the corresponding shells. The emitted X-rays produced from this process can be detected in the fluorescence yield (FY) mode. The secondary X-ray excitations can promote additional electronic transitions; in fact when a vacancy is created in the L-shell by the excitation, an electron from the M or N shell "jumps in" to occupy the vacancy Figure 2.14.

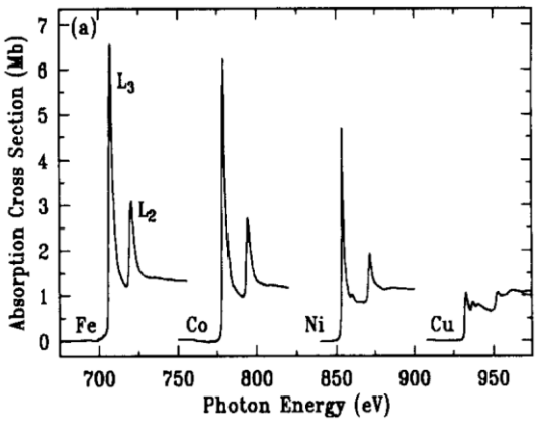

Figure 2.13. X-ray absorption spectra recorded by total electron yield detection near the L2, and L3 edges for Fe, Co, Ni, and Cu metal, showing the existence of white lines for Fe, Co, and Ni and its near-absence for Cu, due to its nearly filled d shell. Adapted from ref [24].

In this process, it emits X-rays and in turn, produces a vacancy in the M or N shell. In transition metals the *d*-orbitals are partially filled and close to the Fermi level. If an X-ray has just sufficient energy to excite a core level, then the resultant photoelectron will leap into unoccupied states above the Fermi level

Figure 2.14(b). On the other hand when the excitation energy from the inner atom is transferred to one of the outer electrons, this (Auger) electron is ejected from the atom. The energy spectrum of the emitted electrons consists of well defined lines due to photoelectrons and Auger electrons on top of a background due to secondary electrons. These low-energy secondary electrons resulting from inelastic collisions of initially excited photoelectrons or Auger electrons, give rise to a major portion of the electron emission, and the sample can be regarded as an effective electron multiplier. Monitoring the total electron yield (TEY), i.e. all electrons emitted from the sample, offers the simplest mode for detecting the photo-absorption process. It is often easier to measure not the emitted electrons directly but their complement given by the sample drain current flowing into the sample. The transitions are usually labeled according to the position of the exited electron; transition from the $p_{1/2}$ level would lead to the L_2 line, while transition from $p_{3/2}$ would lead to the L_3 line.

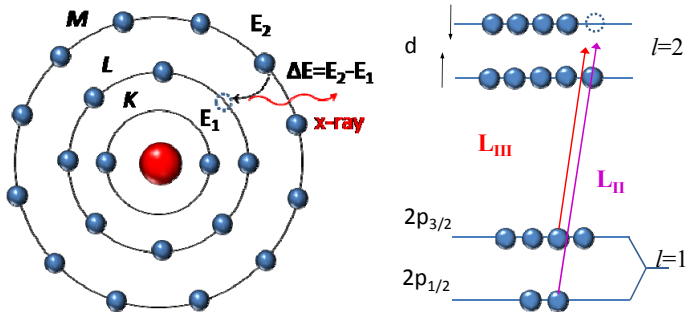

Figure 2.14. Schematic diagram of fluorescence process (left) and electronic transition (right).

Spectra taken from a single metal mainly show two broad peaks, reflecting the width of the empty *d*-bands (Figure 2.6). In general the oxide spectra are more complicated exhibiting multiplet structure due to the electrostatic interactions between 2p core-hole and 3d valence electrons and 2p core-hole spin-orbit interactions, as well as by the local crystal fields and the hybridization with the O 2*p* ligands [25, 26].

6.2 XMCD: magnetic information

A correct description of the dichroism effect can be made by applying the principles of crystal-field theory. In a semi-classical model where the atom is quantified and the electromagnetic field is described by Maxwell's equations. The interaction Hamiltonian is written as

$$H_{int} = -\left[\sum_i \frac{q}{m} p_i \cdot A(r_i) - \sum_i \frac{q^2}{2m} A(r_i)^2\right] - \left[\sum_i g_i \frac{q}{m} S \cdot B(r_i)\right] \quad (2.5)$$

where q, m, **p**, and **S** are the electron charge, mass, momentum and spin respectively. The photon electromagnetic field is described by the vector potential ***A*** which includes the electric field ***e,*** and by ***B.*** The second term is proportional to the electric quadrupole operator while the third term is proportional to the magnetic dipole operator. Magnetic dipole transitions and electric quadrupole transitions are respectively about 10^5 and 10^8 times more unlikely than similar electric dipole transitions. In a first order approximation the third term results to be zero. This means that the spin is conserved during the absorption: $\Delta m_s = 0$. (Spin dependence will result from spin-orbit interactions). From the time-dependent perturbation theory we know that the transition probability between an initial state $|i\rangle$ to a final state $|f\rangle$, is given the Fermi Golden Rule:

$$T_{i,f} = \frac{2\pi}{\hbar} \sum_{i,f} |\langle f|e \cdot r|i\rangle|^2 \, \delta\left(E_f - E_i - \hbar\omega\right) \quad (2.6)$$

where ***e*** is the X-ray electric field vector and ***r*** denotes the electron's position vector: $r = e_x x + e_y y + e_z z$

Therefore one should proceed with the calculation of the transition matrix elements$|\langle f|\boldsymbol{e} \cdot \boldsymbol{r}|i\rangle|^2$. Since the electromagnetic field is circular polarized which means that vector turns around the direction of propagation we will have:

$$e^- = \frac{1}{\sqrt{2}}\left(e_x - i e_y\right) \;\; right \quad (2.7)$$

$$e^{+} = \frac{1}{\sqrt{2}}\left(e_x + ie_y\right) \qquad left \tag{2.8}$$

The transition is now described by polarization-dependent dipolar operators: $\boldsymbol{e^{+}\cdot r}$ and $\boldsymbol{e^{-}\cdot r}$. The dipolar operators can be written in terms of the spherical harmonics $\boldsymbol{Y_l^{m_l}(\theta,\varphi)}$ where l=1 and m_l=0,±1 , assuming the form $\boldsymbol{P_{m_l}^{(l)}}$ which depicts the role of the orbital angular momentum l and its projection along the z direction m_l (m_l=0 would refers to linear polarization):

$$P_1^{(1)} = \frac{1}{\sqrt{2}}(x + iy) = -r\sqrt{\frac{4\pi}{3}}Y_1^1 \qquad right \tag{2.9}$$

$$P_{-1}^{(1)} = \frac{1}{\sqrt{2}}(x - iy) = r\sqrt{\frac{4\pi}{3}}Y_1^{-1} \qquad left \tag{2.10}$$

$$P_0^{(1)} = z = r\sqrt{\frac{4\pi}{3}}Y_1^0 \qquad linear \tag{2.11}$$

The transition matrix element, a combination of spherical harmonics, is non-zero only if:

$$\Delta l = l_f - l_i = \pm 1 \tag{2.12}$$

$$\Delta m_l = m_{lf} - m_{li} = +1 \qquad left \tag{2.13}$$

$$\Delta m_l = m_{lf} - m_{li} = -1 \qquad right \tag{2.14}$$

where l is the orbital momentum and m_l its projection along z direction. These are the selection rules for the electric dipole approximation. Finally the two absorption cross-section for the left (σ_+) and right (σ_-) circular polarization are

$$\sigma_{\pm} = 4\pi^2\hbar\omega\alpha \sum_{i,f}\left|\left\langle i\left|\mp\sqrt{\frac{4\pi}{3}}rY_1^{-1}\right|f\right\rangle\right|^2 \delta\left(E_f - E_i - \hbar\omega\right) \tag{2.15}$$

The experimental dichroism signal is then defined as the asymmetry ratio:

$$XMCD = \frac{\sigma_+ - \sigma_-}{\sigma_+ + \sigma_-} \tag{2.16}$$

Constraints on the transition are represented by the selection rules. Because of the $\Delta J=0,\pm1$ dipole selection rule the $1/2 \rightarrow 5/2$ (or inverse) transition is forbidden (spin flips are forbidden in electric dipole transition), spin-up (spin-down) photoelectrons from the *p* core shell can only be excited into spin-up (spin-down) *d* hole states. Hence the spin-split valence shell acts as a detector for the spin of the excited photoelectron and the transition intensity is simply proportional to the number of empty *d*-states of a given spin [27]. The quantization axis of the valence shell "detector" is given by the magnetization direction. When circular polarization is applied to the photon beam, the electromagnetic field vector turns around the direction of the propagation vector. The difference between the transition probability for left and right circularly polarized light gives the circular magnetic dichroism. Since the dipole selection rule is different for right (RCP) and left (LCP) circularly polarized light, the respective components may be absorbed differently, depending on the nature of the two magnetic band states (see Figure 2.15). The emitted radiation will reflect this imbalance and will be elliptically polarized with the major polarization axis rotated relative to that of the incident light. The most common way of measuring XMCD in the soft x-ray region is total electron yield (TEY)

X-ray resonant magnetic reflectivity (XRMR) provides an alternative method for measuring the magnetic dichroism from the subsurface region. Resonant reflectivity measurements present some advantages if compared to other techniques. XRMR is a coherent elastic scattering process with no complex final state effect, and the presence of a core excitation makes it element selective [27]. It also presents some strictly experimental advantages: it is a photon-in/photon-out process, hence not affected by the presence of magnetic fields acting on the sample, and collecting the reflectivity at different angles gives a coarse way of tuning the probing depth [28-30]. XRMR and XMCD signals cannot be directly compared since the reflected intensity measured is a dynamically scattered beam that depends upon both the absorptive and dispersive parameters of the material. The most common way of measuring XMCD in the soft x-ray region is total electron yield (TEY), because of the easy experimental setup and high signal-to-noise ratio compared to fluorescence yield. After determining the energy position of the maximum magnetic signal, one can sweep the magnetic field to recreate a hysteresis loop. The determination of the intensity, shape, coercivity of a XMCD hysteresis loop can be very useful to

distinguish between the magnetic behavior of the single layers in multilayers of alternating soft and hard ferromagnets [31] and as further information about induced ferromagnetic moment at interfaces [32].

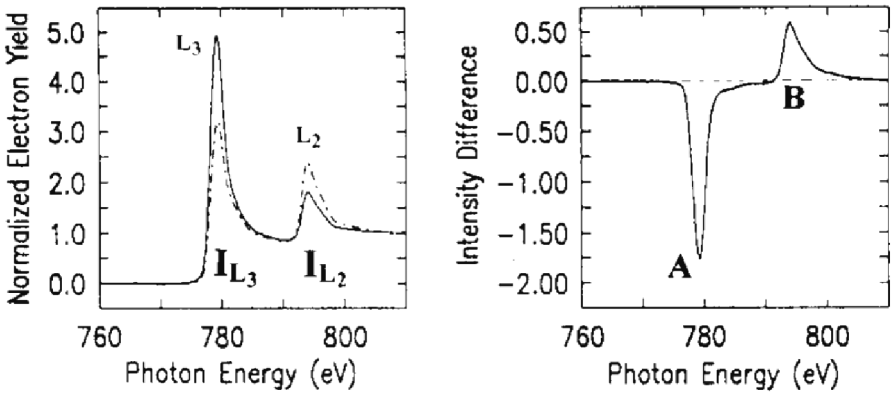

Figure. 2.15: (Left) Normalized X-ray magnetic circular dichroism spectra at the L_3 and L_2 edges for Co metal. The original spectra have white line intensities I_{L3} and I_{L2} which depend on the relative orientation of photon spin and magnetization direction, shown solid for parallel and dashed for antiparallel alignment. (Right) The difference spectrum gives dichroism intensities ,A < 0 and B > 0 at the L_{III} and L_{II} edges, respectively.

7 Polarized neutron reflectometry

Similarly to the X-ray reflectivity, polarized neutron reflectometry (PNR) consists of a measure of the intensity of the reflected neutron beam as a function of the perpendicular component of the wave vector transfer . Due to the fact that polarized neutrons are intrinsically sensitive to the difference of both magnetic and nuclear components of the refractive index across interfaces, PNR can provide detailed quantitative information about the magnetization depth profile and structural details of thin films and multilayers. Scattering techniques (diffraction, inelastic scattering) were developed soon after the discovery of the neutron but PNR is a relatively new technique [33, 34]. Like X-rays and electrons, neutrons can be reflected on surfaces. In reflectivity geometry, the incidence angle θ_i is the same as the reflection angle θ_r and typically starts from a region of total reflection, in the range 0.5º-5º. The reflected radiation is related to the depth dependence of the index of refraction averaged over the lateral

dimensions of the surface or interface. PNR is characterized by an extremely high depth resolution of a fraction of a nanometer even for films as thick as several hundred nanometers. For instance, in a multilayered stack consisting of ferromagnetic and non-ferromagnetic layers any parallel or antiparallel alignment of the ferromagnetic layers can be uniquely distinguished. The neutron is a very well suited probe for investigation of magnetic thin films. It is highly penetrating into the sample, without structural damages, due to its neutrality. At the same time, it interacts with the magnetic moments since it has spin $\frac{1}{2}$. Interactions can be represented by a scattering potential consisting of a nuclear contribution and a magnetic contribution: $V = V_n + V_m$.

Treating the neutron as a particle-wave, we can solve the Schrödinger wave equation and obtain an expression which connects the index of refraction with the wave vector in each medium. In order to simplify the problem we account for some condition such one dimensional scattering potential, specular reflection (Figure 2.17) and elastic scattering. The scattering potential resulting from the interaction between neutron and nuclei in the material is given by:

$$\mathrm{V(y)} = \frac{2\pi\hbar^2}{\mathrm{m}}\rho(\mathrm{y}) \qquad (2.17)$$

where *y* is the direction perpendicular to the sample surface. The depth dependent quantity ρ is called the *scattering length density* (SLD) and is the sum of the atomic density of the nuclei in the material multiplied by their individual nuclear coherent scattering lengths b_i [33]:

$$\rho = \sum_i^J \mathrm{N_i b_i} \qquad (2.18)$$

For example in the case of $SrTiO_3$:

$$\rho_{\mathrm{STO}} = \frac{\sum_i^J \mathrm{n_i b_i}}{\mathrm{V_{STO}}} = \frac{1\cdot 7.02+1\cdot(-3.438)+3\cdot 5.803}{(3.905)^3}\frac{10^{-15}\mathrm{m}}{10^{-28}\mathrm{m}^3} = 3.53\cdot 10^{-6}\text{Å}^{-2}$$

where the volume V_{STO} is the volume of the STO unit cell.

The Schrödinger equation in this system is

$$\left[\frac{\hbar^2}{2m}\frac{\partial^2}{\partial y^2} + V(y)\right]\Psi(y) = E \cdot \Psi(y) \tag{2.19}$$

the wave functions for the incident and transmitted wave take the form:

$$\Psi_0(y) = e^{+ik_0 y} + re^{-ik_0 y} \tag{2.20}$$

$$\Psi_1(y) = te^{+ik_1 y} \tag{2.21}$$

where r and t are the reflection and transmission amplitudes respectively.

Elastic scattering imply conservation of momentum ($|\vec{k_i}| = |\vec{k_f}| = k_0$) and conservation of neutron intensity ($|\Psi|^2 = 1$).

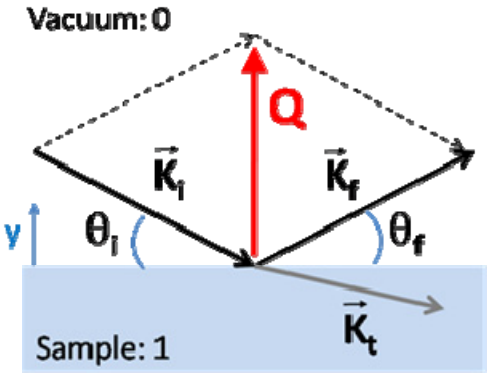

Figure 2.17. Specular reflection and direction of the wave vector transfer Q.

Applying the condition of continuity

$$\Psi_0(0) = \Psi_1(0) \qquad \left.\frac{\partial \Psi_0}{\partial y}\right|_{y=0} = \left.\frac{\partial \Psi_1}{\partial y}\right|_{y=0} \tag{2.22}$$

you can obtain the final form of the reflection amplitude

$$r = \frac{k_0 - k_1}{k_0 + k_1} \tag{2.23}$$

The energy E and the wave vector k_0 of the incident neutron are given by:

$$\begin{cases} E = \frac{\hbar^2 k_0^2}{2m} \\ k_0 = \frac{2\pi \sin\theta_i}{\lambda} \end{cases} \quad (2.24)$$

with m and λ, neutron mass and wavelength respectively. An expression in the form of the Helmholtz equation arises:

$$\left[\frac{\partial^2}{\partial y^2} + 4\pi\rho(y) - k_0^2\right]\Psi(y) = 0 \quad (2.25)$$

which implies: $k = \frac{2m}{\hbar^2}(E - V)$

From general optical considerations: $nk_0 = k_1$ and $n^2 = 1 - \frac{V}{E}$

If we match these last two equations we obtain:

$$k_1 = \sqrt{1 - \frac{4\pi\rho(y)}{k_0^2}}\, k_0 \quad (2.26)$$

The observed quantity, the reflectivity, is defined as: $R = rr^* = |r|^2$ so that

$$R = \left|\frac{k_0 - k_1}{k_0 + k_1}\right|^2 \quad (2.27)$$

The accessible range of wave vector transfer:

$$Q = k_f - k_i = \frac{4\pi \sin\theta}{\lambda} \quad (2.28)$$

is inversely proportional to the resolution of a material distribution in real space; this allows connecting a R vs $Q_\perp$ pattern to the depth profile of the sample. The intensity of the reflected radiation is measured for selected values of the scattering wave vector k_0. This can be achieved by changing the wavelength λ of the neutron beam. The neutron wavelength is measured at pulsed neutron sources by recording the time-of-flight of a neutron to travel a known distance.

In a PNR experiment a magnetic field H is usually applied to the sample and represents the laboratory field of reference (see Figure 2.18). Given the relation $\vec{B} = \mu_0 \vec{H} + \vec{M}$, since H is usually much smaller than M, the neutron spin will interact only with the magnetic induction inside the sample and then cannot distinguish between spin and orbital moment. The magnetic contribution to the scattering potential is given by $V_m = -\overrightarrow{\mu_n} \cdot \vec{B}$ where μ_n is the neutron magnetic moment. Neutrons can be polarized, by appropriate devices, to be parallel or antiparallel to the field applied to the sample. The guiding field, the polarization axis of the incident beam and the field used as a detector are usually collinear so the guiding magnetic field outside the sample provides a quantization axis for the neutron spin. If the magnetic induction ***B*** inside the sample makes an angle with the applied field H, the in-plane component of ***B*** perpendicular to H will lead to spin-flip scattering (the spin state of the reflected neutron may flip 180º depending upon the time the neutron spends in that region and the strength of the induction). This is a consequence of the precession of the neutron spin around *B*. As a convention, R^{++} and R^{--} indicate the non-spin-flip reflectivities (where the sign + and - indicates spin parallel or antiparallel to H respectively). Since neutrons are reflected by potential gradients across interfaces and since $\nabla \cdot B = 0$, perpendicular components of ***B*** are constant across a reflecting interface and therefore do not produce specularly reflected intensity [35].

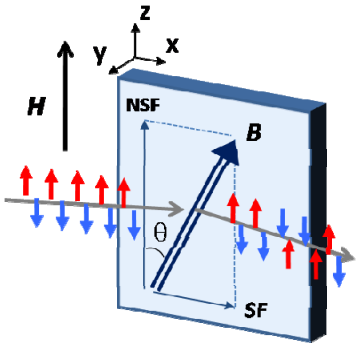

Figure 2.18. Schematic representation of the magnetization components which induce spin flip (SF) and non-spin flip (NSF) scattering, relative to the neutron polarization

If the magnetic induction is collinear with the guiding field and then with the direction of the incident neutron spin, the polarization of the neutron beam will remain the same after interacting with the magnetization of the sample.

Reflectivity in this case depends on the relative orientation of the spin (parallel or antiparallel) of the incident neutron and the magnetization of the magnetic layer. As a result, the magnetic film acts as a birefringent medium and the scattering potential takes the form:

$$V^{\pm} = \frac{2\pi\hbar^2}{m}\rho \pm \mu B \tag{2.29}$$

The solution to the Schrödinger equation now contains the spin dependence:

$$\Psi(y) = U_+ \begin{pmatrix} 1 \\ 0 \end{pmatrix} \Psi_+ + U_- \begin{pmatrix} 0 \\ 1 \end{pmatrix} \Psi_-$$

where:

$$\Psi_+(y) = e^{ik_+ y}$$
$$\Psi_-(y) = e^{ik_- y}$$

The refractive index is given by:

$$k_{\pm} = n_{\pm} k_0 = \sqrt{1 - \frac{4\pi(\rho_n \pm \rho_m)}{k_0^2}}\, k_0 \tag{2.30}$$

The neutron magnetic scattering length (mSLD) density ρ_m can be defined as:

$$\rho_m = \sum_i^J N_i p_i = C \sum_i^J N_i \mu_i = C'm \tag{2.31}$$

where p is the magnetic scattering length (in units of Å), μ is the magnetic moment per formula unit (in Bohr magnetons μ_B) and m is the volume magnetization density (in emu/cm^3), $C = 2.645 \cdot 10^{-5} Å \mu_B{}^{-1}$ and $C' = 2.853 \cdot 10^{-9} Å^{-2} cm^3/emu$.

For the analysis of polarized neutron reflectometry data it is used the software POLLY, which has been developed in ISIS Science and Technology Facilities Council. It performs analysis of the R^{++} and R^{--} reflectivity curves by optimizing several parameters introduced by the user and initially set to describe an ideal model. The optimization is obtained by minimizing the χ^2 that is a measure of the error between the observed and the calculated reflectivity.

8 Tunnel junction patterning

Thin films must be geometrically defined laterally or patterned in the layer plane in order to obtain tunnel junction devices. The complexity of the patterning process depends on the materials involve in the thin film and the feature dimensions. Tunnel junction pillars required near few μm lateral to avoid tunnel barrier defects and obtain measured junction resistance values, therefore standard ultra violet (UV) optical lithography and dry etching techniques such Ar ion milling are necessary.

8.1 Optical Lithography

Photolithography is a technique used to produce high precision two-dimensional patterns in the microscopic scale on a photoresist material [36], it is the equivalent to the negative used in photography. These patterns are optically projected from a master pattern in a photomask, which are generally made of a thin chromium or ferrite layer on a glass or quartz plate. Masks patterns commonly fabricated using high resolution lithography process using electron beam lithography. Printing of this negative mask requires physical transference of the pattern to the film surface in question through the use of a photoresist which is sensible to the UV radiation. Two types of photoresist are available and their behaviors are distinguished in the effect of the light. The positive photoresist faithfully reproduces the opaque mask pattern, in this case light exposure causes scission of polymerized chains rendering the resist soluble in the developer. Alternatively, negative resists reproduce the transparent portion of the mask pattern because photon-induced polymerization leaves a chemically inert resist layer behind [37]. The resist layer deposited on the sample surface must be thin enough to obtain high lateral resolution. This thickness should be near few microns or less. To obtain these thicknesses a spinner system, which achieves high speeds near 6000 rpm, is used.

Figure 2.19. Photograph of a Karl Suss alignment equipment.

The core of the microlithography process is the exposure system. Figure 2.19 shows the alignment and exposure system, it consists of a lithographic lens system to collimate UV light from a Hg lamp, a mask holder, a optical microscope, and a sample positioning system with micrometers screws.

8.2 Ar Ion Milling

Ar ion milling is basically a sputtering process where the sample position is on the target place. In this case the inert-gas-ions impact on the sample surface removing selected regions which are not protected with the photolithography resist. This technique is not material selective, therefore if your features are submicron size you must use reactive gases. In this work we have used a South Bay Reactive Ion Etcher 2000 ion system as an Ar ion milling. This system works at pressures around 100 mTorr, at these high pressures the etching process is isotropic, which means a low aspect ratio etching. Our featuring size in the micron size is much higher than the etching depth of around 10 nm, allowing us working at high pressures. Other technical considerations have to be account such the etching rate of your sample's materials and the photoresist employed. Although the etching rate of the $La_{0.7}Sr_{0.3}MnO_3$ and the $BaTiO_3$ is very small comparing with the resist, using large enough resist thickness allows that the resist is not completely removed when the etching process is finished. To

minimize any heating which can produce resist degradation or sample desoxygenation, the sample is mounted onto the water-cooled sample-holder.

8.3 From trilayer to tunnel junction device

In order to increase the number of measureable tunnel junction per sample we have reduced the number of technological steps comparing with previous work in our group [38]. It also reduces the time of patterning process allowing us to measure more samples. A schematic of the complete patterning process is represented in Figure 2.20.

1. The first process step defines the junction pillars in the trilayer structure. After cleaning the sample surface with subsequent ultrasonic baths of acetone and propanol, we deposit metal on the whole sample surface evaporating silver. In the first lithography process the mask used consists of dark junction areas on a clear background, so that once the resist is exposed and developed; only those areas on the sample are covered with resist so as to be preserved from the ion milling etching step. Once the lithographic substep is completed, the sample is etched down beyond the upper electrode to either the barrier or the lower electrode layer, defining trilayer pillars.

2. Electrical passivation is done to avoid short circuiting the pillar when contacting the lower and upper portions. The sample is covered with a thick (700nm) layer of resist. Although photoresist is not a suitable passivator for low temperature measurements, depositing resist is much easier than sputter SiO_2 or other oxide taking only a few minutes. We open holes in the resist layer to perform electrical contacts on the junctions and lower electrodes. Thus the mask used consists of light areas on a dark background.

3. The third process step defines electrical pads. Using a simple mechanical mask we fill the holes and define the electrical pads of near 1 mm^2 size on the top of the resist evaporating silver.

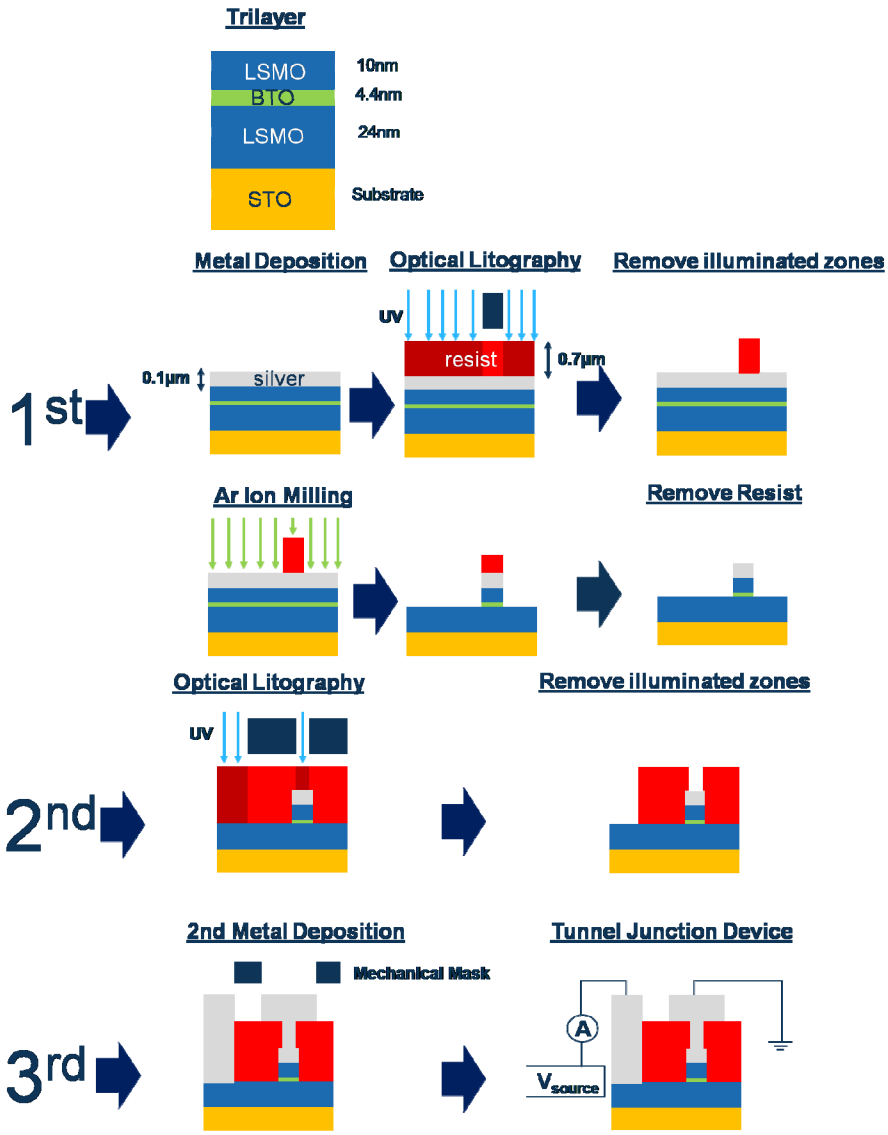

Figure 2.20. Schematic of the 3 steps patterning process from the trilayer (top) to the final device (bottom).

9 Resistance measurements

For our low temperature resistance measurements we used a closed-cycle Cryophysics helium refrigerator which works with the expansion of highly-pure He-gas compressed in a Gifford McMahon cycle. The expansion through the capillaries undergoes two steps at 50K and at 8.5K. The sample is mounted onto a cooled copper piece in contact with the second cooling step. The system is evacuated by a rotary pump capable of a pressure down to 10mTorr, measured with a Pirani vacuum sensor. The best temperature was 14K. A silicon diode thermometer is in contact with the sample holder calibrated for measuring between 10 and 325K. The system is also equipped with a heater controlled by a Lake Shore 330-11 temperature controller which permits to control the sample's temperature between room temperature and 14K with 10-mK accuracy. Micro-coaxial wires connect the different parts for low noise measurements. For magnetoresistance measurements we used an electromagnet (with a 10cm separation between the magnetic cores) which provided a magnetic field in the range of ± 4200Oe.

The resistance of thin layer was measured using the Van der Pauw four-point method [39] to eliminate any contribution given by the in-series contact resistance. Four electrical contacts were made on the surface of the sample by evaporation of silver and then connected to the low-noise wiring by indium. In the case of tunnel junctions (current perpendicular to plane) measurement because the junction resistance are much higher than the electrode, and the silver/manganite is an ohmic contact, we were measured using 2-points method. The instruments used were a Keithley 2400 sourcemeter, capable of apply voltage between 5μV and 210V and measure current from 10pA to 1.055A.

10 References

[1] D. M. Kelly, E. E. Fullerton, J. Santamaria, and I. K. Schuller, *Scripta Metall. Mater.* **33**, 1603 (1995).

[2] O. Nakamura, E. E. Fullerton, J. Guimpel, and I. K. Schuller, *Appl. Phys. Lett.* **60**, 120 (1992).

[3] A. Guinier, *X-ray diffraction in crystals, imperfect crystals, and amorphous bodies* (Dover Publications, 1994)]

[4] E. E. Fullerton, I. K. Schuller, H. Vanderstraeten, and Y. Bruynseraede, *Phys. Rev. B* **45**, 9292 (1992).

[5] R. Egerton, *Rep. Prog. Phys.* **72**, 016502 (2009).

[6] O. L. Krivanek, G. J. Corbin, N. Dellby, B. F. Elston, R. J. Keyse, M. F. Murfitt, C. S. Own, Z. S. Szilagyi, and J. W. Woodruff, *Ultramicroscopy* **108**, 179 (2008).

[7] C. Jeanguillaume and C. Colliex, *Ultramicroscopy* **28**, 252 (1989).

[8] J. M. Cowley, Bull. *Mater. Sci*. **6**, 477 (1984).

[9] S. J. Pennycook, and L. A. Boatner, *Nature* **336**, 565 (1988).

[10] S. J. Pennycook, *Ultramicroscopy* **30**, 58 (1989).

[11] E. Okunishi, I. Ishikawa, H. Sawada, F. Hosokawa, M. Hori and Y. Kondo, *Microsc. Microanal*. **15**, 164 (2009).

[12] S. D. Findlay, N. Shibata, and H. Sawada, *Appl. Phys. Lett*. **95**, 191913 (2009).

[13] N. D. Browing, M. F. Chisholm, and S. J. Pennycook, *Nature* **366**, 143 (1993).

[14] P. E. Batson, *Nature* **366**, 727 (1993).

[15] N. Browning, D. Wallis, P. Nellist, and S. Pennycook, *Micron* **28**, 333 (1997).

[16] O. L. Krivanek, and J. H. Paterson, *Ultramicroscopy* **32**, 313 (1990).

[17] H. Kurata, and C. Colliex, *Phys. Rev. B* **48**, 2102 (1993).

[18] J. H. Rask, B. A. Miner, and P. R. Buseck, *Ultramicroscopy* **21**, 321 (1987).

[19] A. Gruverman, O. Auciello, and H. Tokumoto, *Integr. Ferr.* **19**, 49 (1998).

[20] M. Alexe, and A. Gruverman, *Nanoscale Characterizations of Ferroelectric Materials, Scanning Probe Microscopy Approach* (Springer 2004).

[21] J. L. Erskine, and E. A. Stern, *Phys. Rev. B* **12**, 5016 (1975).

[22] K. H. Müller, K. Dörr, T. Walter, M. Sahana, K. Brand, and L. Schultz, *J. Magn. Magn. Mater.* **242-245**, 447 (2002).

[23] F. Groot, and J. Vogel, *Neutron and X-ray Spectroscopy*, 3 (Springer 2006).

[24] J. Stöhr, and J. Electron. *Spectrosc. Relat. Phenom*. **75**, 253 (1995).

[25] B. Thole, P. Carra, F. Sette, and G. Van der Laan, *Phys. Rev. Lett.* **68**, 1943 (1992).

[26] T. Burnus, Z. Hu, H. H. Hsieh, V. L. J. Joly, P. A. Joy, M. W. Haverkort, H. Wu, A. Tanaka, H. J. Lin, C. T. Chen, and L. H. Tjeng, *Phys. Rev. B* **77**, 125124 (2008).

[27] C. Kao, J. B. Hastings, E. D. Johnson, D. P. Siddons, G. C. Smith, and G. A. Prinz, *Phys. Rev. Lett*. **65**, 373 (1990).

[28] J. W. Freeland, K. E. Gray, L. Ozyuzer, P. Berghuis, E. Badica, J. Kavich, H. Zheng, and J. F. Mitchell, *Nat.Mater*. **4**, 62 (2005).

[29] S. Valencia, A. Gaupp, W. Gudat, Ll. Abad, Ll. Balcells, and B. Martinez. *J. Appl. Phys*. **104**, 023903 (2008).

[30] M. Yu, J. Hattrick-Simpers, I. Takeuchi, J. Li, Z. L. Wang, J. P. Liu, S. E. Lofland, S. Tyagi, J. W. Freeland, D. Giubertoni, M. Bersani, and M. Anderle. *J. Appl. Phys.* **98**, 063908 (2005).

[31] P. Carra, B. T. Thole, and M. Altarelli, X. Wang. *Phys. Rev. Lett*. **70**, 694 (1993).

[32] C. T. Chen, Y. U. Idzerda, H. -J. Lin, G. Meigs, A. Chaiken, G.A. Prinz, and G. H. Ho, *Phys. Rev. B* **48**, 642 (1993).

[33] *Neutron News*, Vol. 3, No. 3, pp. 29-37 (1992)

[34] G. P. Felcher, R. O. Hilleke, R. K. Crawford, J. Haumann, R. Kleb, and G. Ostrowski, *Rev. Sci. Instrum*. **58**, 609 (1987).

[35] J. F. Ankner, and G. P. Felcher, *J. Magn. Magn. Mater*. **200**, 741 (2000).

[36] I. Brodie, and J. J. Muray, *The Physics of Micro/Nano-Fabrication*, (Plenum Press, 1992).

[37] M. Ohring, *The Materials Science of Thin Films* (Academic Press, 1992).

[38] F. A. Cuellar, *Magnetic Tunnel Junction Based on Complex Oxides*, Ph. D. Thesis, Universidad Complutense de Madrid (2012).

[39] L. Van der Pauw, *Philips Technical Review* **20**, 220 (1958).

3

Characterization of Multiferroic $La_{0.7}Sr_{0.3}MnO_3$/ $BaTiO_3$ Heterostructures

Multiferroics are materials where coexist at least two different ferroic orders (ferromagnetism, ferroelectricity, ferroelasticity, and ferrotoroidicity), which are often they coupled to each other [1]. The most studied multiferroic system is the one which combine ferromagnetism, and ferroelectricity, but very few of them show a finite large moment. Artificial multiferroic heterostructures combining ferromagnetic and ferroelectric thin layers have been presented as a solution to improve one-phase multiferroic properties, due to the possibility of optimize its ferroelectric and ferromagnetic properties, in addition, a large magneto-electric coupling at the interface could be engineered [2]. Among perovskite oxides systems, ferromagnetic $La_{0.7}Sr_{0.3}MnO_3$ (LSMO) and ferroelectric $BaTiO_3$ (BTO) seem to be suitable materials due to their robust ferroic orders which persist at room temperature, bringing the possibility to generate a new class of oxide devices. LSMO has been extensively studied as a possible source of spin polarized electrons at room temperature [3]. La Sr doped manganites posses a rich phase diagram as a function of hole concentration, and temperature, which include metal-insulator transition, and different magnetic phases [4]. The hole concentration can be controlled electrostatically [5] giving the possibility to change the magnetic order at the

interface with a ferroelectric [6]. BTO is a well known ferroelectric material with large spontaneous polarization. The capability of enhances its ferroelectric properties using strain engineering [7] reduce its critical thickness, achieving good ferroelectric properties at the nanoscale [8]. The recent improvement in oxides ultrathin film growth techniques open the possibility to persist ferroelectricity in a few unit cells thin layer, and the high quality sharp interfaces in oxide heterostructures brings the opportunity to combine different materials to achieve novel states at the interface [9] and large magneto-electric coupling [10].

1 Introduction

1.1 $La_{0.7}Sr_{0.3}MnO_3$

In the renaissance of the study of manganites during the 1990s, considerable emphasis was given to the analysis of $La_{1-x}Sr_xMnO_3$. Its Curie temperature as a function of doping level is above room temperature, increasing its chances for practical applications. The phase diagram and resistivity vs. temperature for this compound at several densities are shown in Figure 4.1 (a) and (b) respectively [11]. In this chapter we have used $La_{0.7}Sr_{0.3}MnO_3$. With this doping level the bulk Curie temperature is T_C = 369K, the saturation magnetization is $M_S = 3.7\mu B/at_{Mn}$ and the low temperature resistivity is $\rho = 8 \times 10^{-5}$ Ω cm. Another important property of LSMO is that it is a half-metallic ferromagnet as demonstrated by spin resolved photoemission experiments [3]. The half metallic character of LSMO means that the minority spin conduction band is empty, so the material has 100% spin polarization at low temperature. This property is also related to the saturation magnetization of LSMO at low temperatures as it matches well the spin only value expected form all 3d electrons present in manganese ions: M_S = 0.7 x Mn^{3+} (S=4/2) + 0.3 x Mn^{4+} (S=3/2) = 0.7 x $4\mu_B$ + 0.3 x $3\mu_B$ = 3.7 μ_B [12].

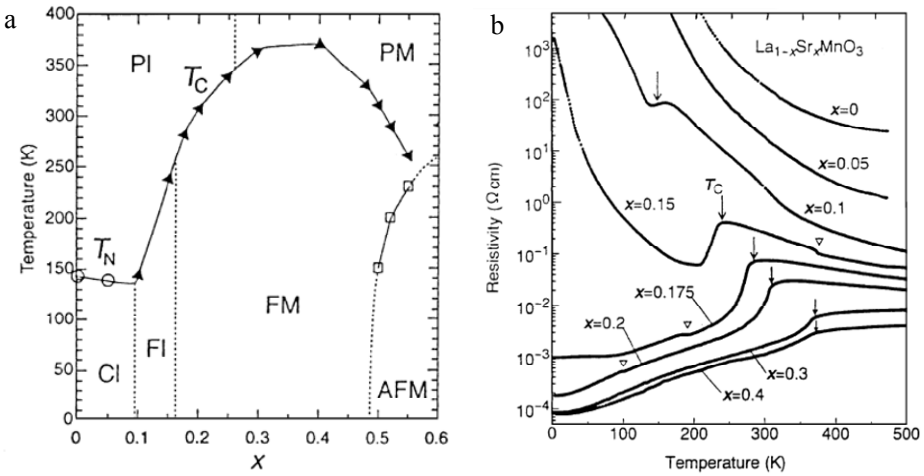

Figure 4.1. (a) Phase diagram of $La_{1-x}Sr_xMnO_3$ prepared with data from [11] and [13]. The AFM phase at large x is an A-type AF metal with uniform orbital order. PM, PI, FM, FI, and CI denote paramagnetic metal, paramagnetic insulator, FM metal, FM insulator, and spin-canted insulator states, respectively. T_C is the Curie temperature and T_N is the Neel temperature. (b) Temperature dependence of resistivity for various single crystals of $La_{1-x}Sr_xMnO_3$. Arrows indicate the Curie temperature. The open triangles indicate anomalies due to structural transitions.

A structural study of a LSMO crystal as a function of temperature shows it to be a rhombohedral perovskite above and below T_C with a=0.3876 nm and α = 90.46º at room temperature [14]. When LSMO is grown as a thin film on a cubic substrate the unit cell is distorted and it adopts a pseudocubic structure. However upon distorting the unit cell, the ratio between the in-plane (a) and out-of-plane (c) lattice parameters becomes important for the magnetic properties of the manganite. In Figure 4.2 the effect of epitaxial strain (c/a ratio) on the orbital order and consequently on the magnetotransport properties of LSMO thin films of different compositions is shown. In these orbital phase diagram the F region (orbital-disordered) is ferromagnetic and metallic, the C ($3z^2$-r^2 ordered) and A region (x^2-y^2 ordered) are insulating [15, 16].

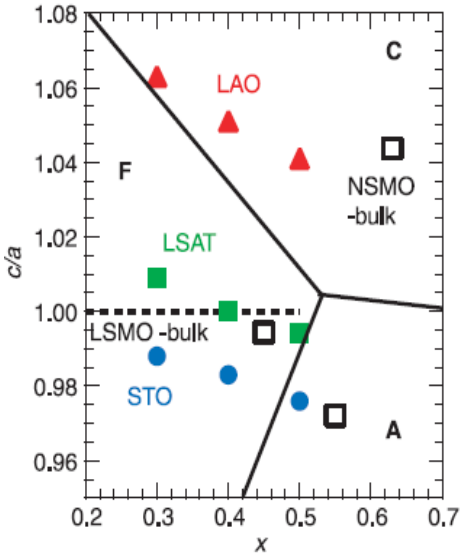

Figure 4.2. The schematic phase diagram in the plane of lattice strain c/a and doping level x. The data labeled LAO, LSAT, and STO represent the results for the coherently strained epitaxial thin films of $La_{1-x}Sr_xMnO_3$ grown on the perovskite single-crystal substrates of LaAlO3, (La, Sr)(Al, Ta)O_3, and $SrTiO_3$, respectively. LSMO-bulk and NSMO-bulk stand for the results for the bulk single crystals of $La_{1-x}Sr_xMnO_3$ and $Nd_{1-x}Sr_xMnO_3$, respectively. Adapted from [14].

Another relevant issue related to LSMO thin film growth is the existence of so-called "dead layer" or critical thickness that can be defined as the thinnest layer for which metallic as well as ferromagnetic behaviors are observed. In different studies this dead-layer thickness for thin films was estimated to be 3-4 nm depending on the substrate chosen. For thin films grown on STO the LSMO dead layer thickness is estimated to be 8 u.c. [17]. The mechanism behind the dead layer problem is still controversial. The phase-separation phenomenon at the LSMO/STO interface where ferromagnetic insulating and metallic phases separate at a scale of a few nanometers is one of the possible explanations [4]. Scanning tunneling spectroscopy [18] and ferromagnetic resonance [19, 20] supports this scenario. Another possible origin of the dead layer is the orbital reconstruction at the LSMO/STO interface. Strain induced distortion of the MnO_6 octahedra leads to crystal-field splitting of the e_g levels and lowers the $d_{3z^2-r^2}$ orbital over the $d_{x^2-y^2}$ orbital resulting in a local C-type antiferromagnetic structure at the interface [21].

1.2 $BaTiO_3$

Barium titanate is a room temperature ferroelectric band-gap insulator. It presents perovskite structure, and bellow the Curie temperature T_c= 393 K it

suffers a phase transition from paraelectric cubic structure a = b = c = 4.000 Å to ferroelectric tetragonal structure with lattice parameter a = b= 3.987 Å, and c = 4.040 Å, and a saturation polarization P_s = 25 μC·cm^{-2}. It's related with the hybridization between empty 3d titanium orbitals and 2p oxygen orbitals. Ti^{+4} ion moves its equilibrium position from the center of the oxygen octahedra giving a finite dipolar moment. Lowering temperature at T = 278 K it suffers a structural transition to orthorhombic (a= 5.704, b=3.963, c=5683, and P_s = 33 μC·cm^{-2}), and at T = 183 K to rhombohedric (a = 5.704, θ= 89.56º, and P_s = 33 μC·cm^{-2}) [22].

Doping BTO with electrons (for example oxygen vacancies), the ferroelectric should be quenched because itinerant electrons screen the long Coulomb interactions. Nevertheless these electrons partially stabilize ferroelectricity screening the strong crystal perturbation caused by oxygen vacancies [23]. Ferroelectric displacement have been observed in oxygen reduced conducting BTO [23,24], and first-principles calculations have sown that the ferroelectric instability in BTO requires only a short-range portion of the Coulomb interactions of the order of the lattice constant, under a critical doping concentration n_c = 0.11 e/u.c. [25]. Doping BTO under this concentration may enhance its range of functionalities, and open opportunities for using doped ferroelectrics in novel electronic devices.

Bulk ferroelectric properties can be enhanced in BTO thin films using strain engineering [7]. Biaxial compressive strain increases transition temperature nearly 500º C, and a remanent polarization at least 250 % higher. This biaxial compression enhances tetragonallity and assures spontaneous polarization in the c-axis. This strain engineering plays a key role to reduce ferroelectric critical thickness, in order to implement BTO as an active tunnel barrier. BTO critical thickness has been calculated to be in the range between 12 to 1 nm [26-30]. Recent PFM experiment have provided evidence of ferroelectricity in BTO ultrathin films growing on $SuRO_3$//$SrTiO_3$. Gruverman et al. [31] have shown ferroelctricity in 2.4 nm BTO films, and growing highly strained BTO on LSMO//$NdGaO_3$ V. Garcia et al. reduce the critical thickness limit down to 1.2 nm [8].

2 Sample Growth and Structural Characterization

All samples in this study were grown by RF sputtering. The pressure during deposition of the thin films and heterostructures was fixed at 3.2 mbar of pure oxygen. The substrate temperature during deposition was 900^0C. After deposition the temperature was fixed at 750^0C and the growth chamber filled with pure oxygen up to P = 900 mbar. Following the annealing step of 60 minutes the sample is cooled down at a rate of 5 K/min to room temperature. The temperature deposition and annealing times and temperature were chosen with two objectives: to obtain good structural properties and to obtain bulk-like Curie temperature and saturation magnetization. This is particularly difficult in manganites where a small amount of oxygen vacancies has a great impact on T_C and M_S.

We have analyzed the structural properties of our samples using non-destructive techniques such X-ray diffraction, X-Ray reflectometry and atomic force microscopy. We also used aberration-corrected scanning and transmission electron microscopy combined with electron energy loss spectroscopy to analyze our sample structural, chemical and electronic properties with sub-atom resolution. The notation used in this chapter for superlattices and bilayers is the following: $[LSMO_M/BTO_N]_P$ denotes a superlattice of P repetitions of a bilayer with thickness M u.c. of LSMO and N u.c. BTO.

2.1 X-ray diffraction

We have used X-ray diffraction experiments to determine the crystalline structure of LSMO and BTO heterostructures to confirm the c-axis oriented growth of the thin films. Figure 3.1 (a) and (b) display X-ray diffraction near STO (002) Bragg peak and reflectivity spectra of $[LSMO_{27}/BTO_{17}]_4$ superlattice. Superlattice Bragg peaks around the substrate (002) Bragg peak in the XRD spectra are clearly seen. Superlattice Bragg peaks are observed also in reflectivity (see arrows in Figure 3.1 (b)). This provides evidence of coherent heteroepitaxial growth with sharp interfaces. Figure 3.1 (b) and (d) display X-ray diffraction near STO (002) Bragg peak and reflectivity spectra of $[BTO_{11}/LSMO_{18}]$ bilayer. The a and c lattice parameters of BTO bulk are 3.992 and 4.036 Å, therefore epitaxial thin barium titanate films on STO (a=c=3.905 Å) suffer biaxial compressive

strain along the a and b-axis, which is reflected by the position of the (002) diffraction peak (see Fig.3.1 (c)); this peak is displaced toward lower angle indicating an enlargement of the c-axis parameter.

The observed reflectivity spectra clearly exhibit a finite size effect, reflecting the smoothness of the surface, LSMO-BTO interfaces and c-axis oriented growth of the heterostructures. The total thicknesses of the film obtained from the reflectivity spectra (see chapter 2) is 94 Å.

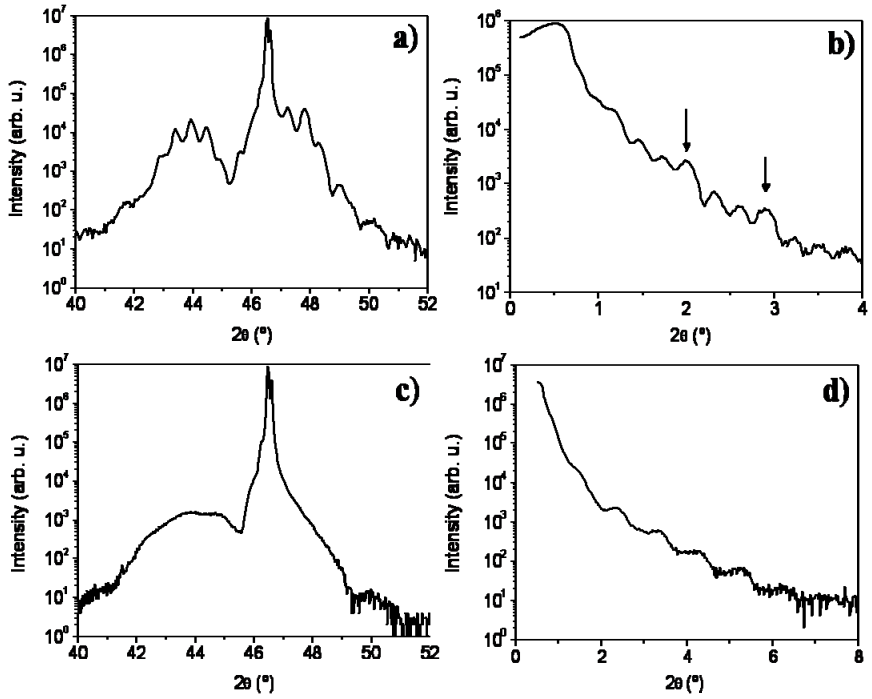

Figure 3.1. (a) X-ray reflectivity and (b) X-ray diffraction spectra of $[LSMO_{27}/BTO_{17}]_4$ superlattice. (c) X-ray reflectivity and (d) X-ray diffraction spectra of a $[BTO_{11}/LSMO_{18}]$.bilayer.

2.2 Atomic Force Microscopy. Topography

Using atomic force microscopy (AFM) we have analyzed the surface morphology of LSMO/BTO bilayers modifying BTO thicknesses. In Figure 3.2

we observed step and terraces structures at the surface of 15 nm LSMO/ 12 nm (left), and 2nm (right) BTO bilayers. Both images show surface free from precipitates. The root-mean-squared (RMS) surface roughness calculated in both samples is smaller than 1 u.c.

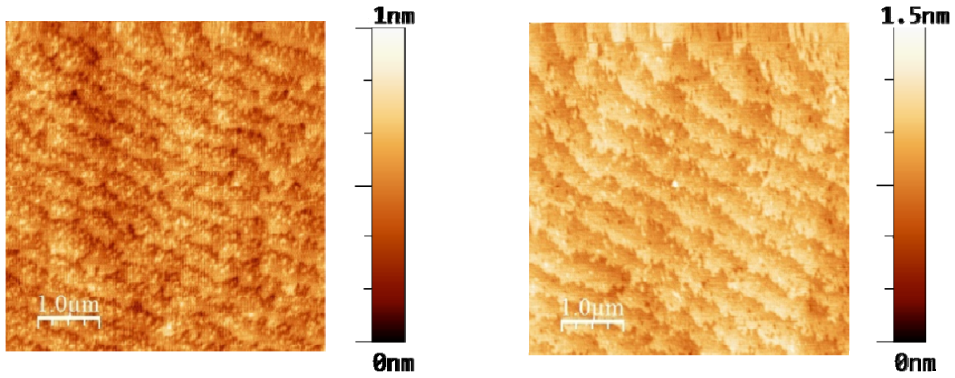

Figure 3.2. Atomic force microscopy topographic 5 µm x 5 µm images of BTO 12nm (left) and 2nm (right) on LSMO 15nm bilayers.

2.3 Scanning transmission electron microscopy

Low magnification high angle annular dark field (HAADF) image (Figure 3.3 (a)) exhibits flat and continuous layers over long lateral distances. The film is free of precipitates, and its roughness at the surface is one atom plane, according with AFM images. In HAADF image we cannot distinguish where exactly start and finish the different layers, consequently we have done a chemical composition analysis using electron energy loss spectroscopy (EELS) technique in the different elements edges. Fig 3.3 (b) shows EELS fine structure spectrum images at Ti L_{23}, Ba M_{45}, La M_{45} and Mn L_{23} edges. The elemental map shows flat layers over long lateral distances and no chemical interdiffussion across the interfaces.

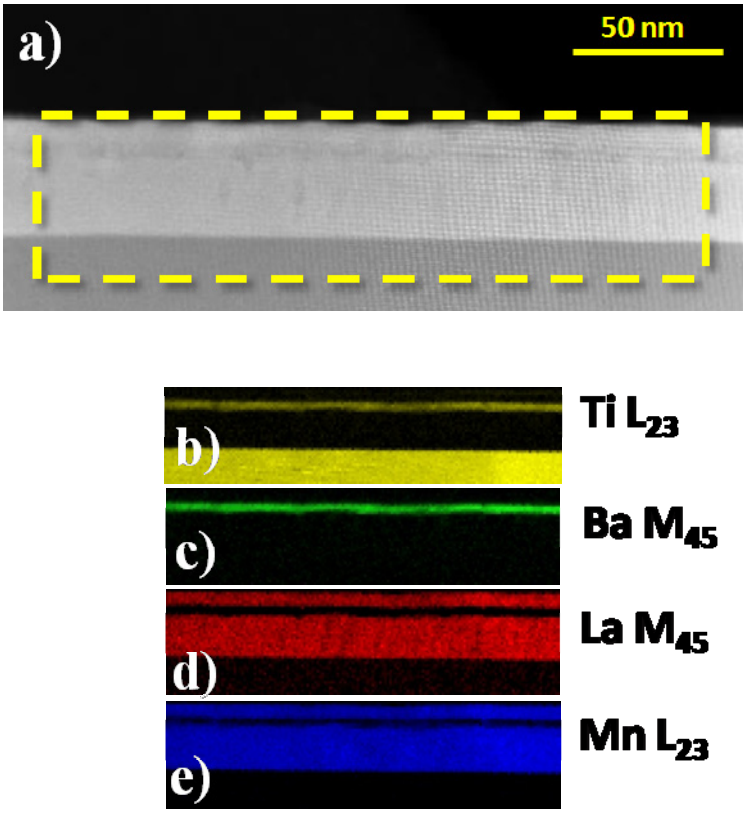

Figure 3.3. (a) Low magnification HAADF image of a LSMO/BTO/LSMO trilayer. (b-e) Atomic elemental maps corresponding to the (b) Ti L2,3, (c) Ba M4,5 (d) La M4,5, (e) Mn L2,3 signals.

The high magnification HAADF image [Figure 3.4 (a)] shows high quality epitaxial interfaces free of defects. The analysis of the the atomic positions of the BTO strained layer in the growth direction and in the plane yields average lattice parameter values c_{BTO} = 4.11 Å and a_{BTO}= 3.94 Å, which corresponds to a c/a ratio of 1.050. This tetragonallity is similar the reported values in ferroelectric nanometric BTO thin films [8, 32]. Note that a_{BTO} is slightly larger than the STO substrate constraint (a_{STO} =3.905) which means that our BTO layer is partially relaxed. EELS chemical map at La M_{45} (c), Mn L_{23} (d), Ba M_{45} and Ti L_{23} (e) edges exhibit sharp interfaces between LSMO and BTO. Both interfaces are $La_{0.7}Sr_{0.3}O$-TiO_2 terminated. $La_{0.7}Sr_{0.3}O$ plane is a positive charged polar plane, and TiO_2 plane is not charged. These symmetric polar interfaces produce two opposite electric dipoles inside the BTO layer [33] which could pinned the ferroelectric polarization producing a detrimental ferroelectric properties [34], this issue will be discussed later in chapter 5. Simultaneous annular dark field (ADF) image [Fig. 3.4 (b)] assures that there is no drifting, beam damage, or charging effects during the spectrum images captures.

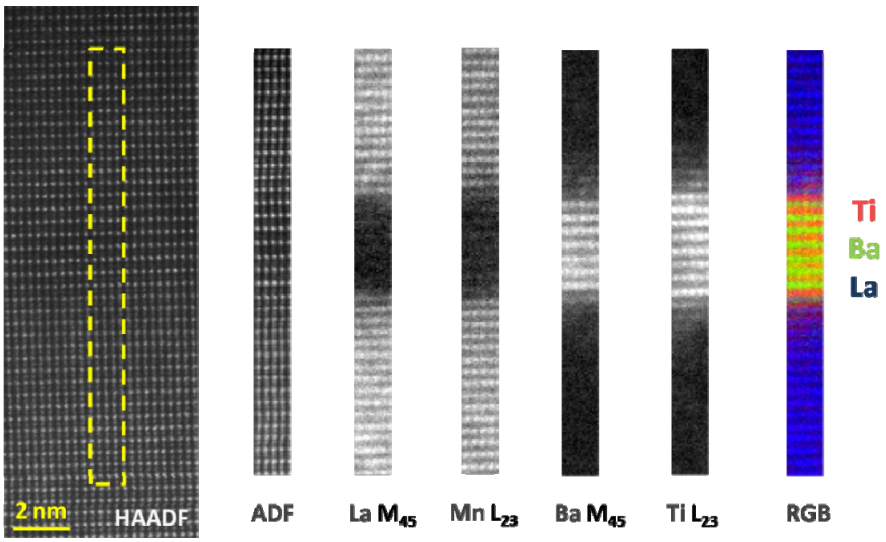

Figure 3.4. (a) High magnification HAADF image of a LSMO/BTO heterostructure. (b) Simultaneous annular dark field ADF images during spectrum images . (c-f) Atomic elemental maps corresponding to the (c) La M4,5 (d) Mn L2,3, (e) Ba M4,5, (f) Ti L2,3 signal. (g) False color image where three atomic resolution images have been overlayed: a Ti $L_{2,3}$ image in red, a La $M_{4,5}$ image in blue, and Ba $M_{4,5,}$image in green (RGB).

3 Magnetism and Electronic Transport

3.1 Magnetic properties

We have studied magnetic and transport properties of [LSMO 25 nm/ BTO 4.4 nm] and [BTO 4.4.nm/ LSMO 5 nm] bilayers, similar thicknesses as used for tunnel barrier and top and bottom electrodes in magnetic tunnel junctions (see chapter 4). Figure 3.5 shows magnetization versus temperature measurements of a [LSMO 25nm/BTO] 4.4 nm taken in a 5 kOe applied field after cooling at 5 kOe. We have extracted a Curie temperature of 350 K. Saturation magnetization increases while lowering temperature, reaching a maximum value of 3.45 μ_B/at_{Mn} at 10K. The Curie temperature is practically the same as bulk manganite (369 K), and the saturation magnetization is slightly smaller than 3.7 μ_B/at_{Mn} in bulk LSMO.

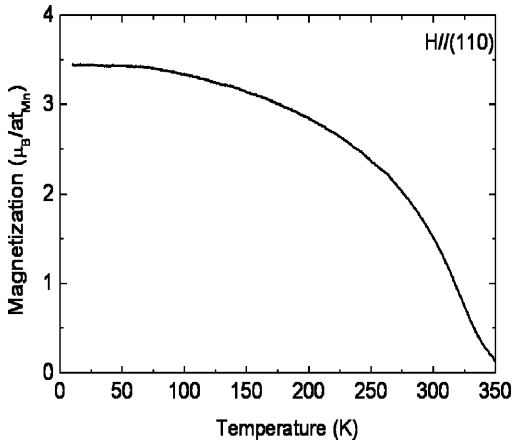

Figure 3.5. Magnetization as a function of temperature measured in 5 kOe applied field after cooling the sample with 5 kOe of a [LSMO 25 nm/ BTO 4.4 nm] bilayer.

In order to obtain high values of tunnel magnetoresistance it is important to realize a state in the magnetic tunnel junction where the top and bottom electrode are antiparallel aligned [35]. If an angle other than 180^0 exists between

the magnetization of top and bottom electrode then depressed TMR is observed. To obtain a perfect antiparallel alignment it is important then that the LSMO layers have the same easy magnetization axis.

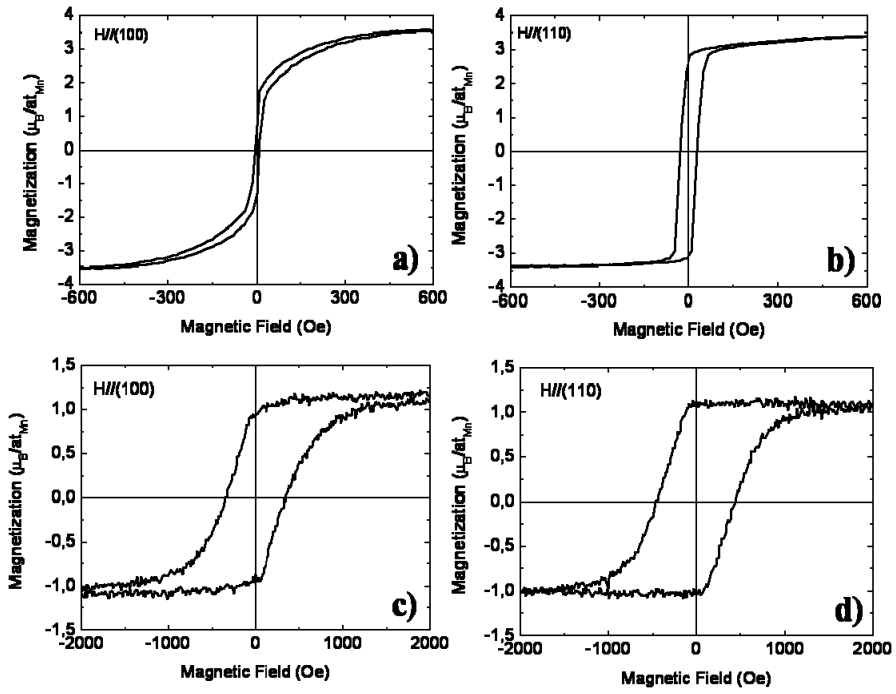

Figure 3.6. Magnetization as a function of magnetic field applied along the [100] ((a) and (c)) and the [110] ((b) and (d)) of a [LSMO 25 nm/ BTO 4.4 nm] (top figures) and [BTO 4.4. nm/ LSMO 5nm] (bottom figures) bilayers at 10 K.

Previous results on LSMO thin films shows that in samples grown on STO (001) the in-plane easy direction is along the [110] and equivalent directions, while the hard directions is along the [100] [36]. We have measured magnetization as a function of applied magnetic field in the [100] (Figure 3.6 (a), (c)) and in the [110] (Fig 3.6 (b), (d)) film direction for a [LSMO 25 nm/BTO 4.4 nm] and [BTO 4.4.nm/ LSMO 5 nm] bilayers. In bilayer with LSMO in the bottom layer ((a) and (c)), the hysteresis loop with magnetic field applied in the [110] direction has clearly remanent magnetization (M_R) and coercive fields (H_C) larger than the ones in the [100] direction. According to the Stoner-Wohlfarth model of magnetization reversal [37], larger coercivity and remanent

magnetization is in general a signature for magnetic field aligned with the easy axis. Because sample with LSMO on top is too thin (5 nm), and near the critical thickness [11], the magnetization is more depressed, and consequently the magnetic signal is weaker, and the measurement is noisier (Fig. 3.6 (b) and (d)). Hysteresis loops with magnetic field applied in the [110] direction has also a remanent magnetization (M_R) and a coercive field (H_C) larger than the ones in the [100] direction, so we can conclude that [110] are the easy axis in both configuration (LSMO on bottom and on top of BTO).

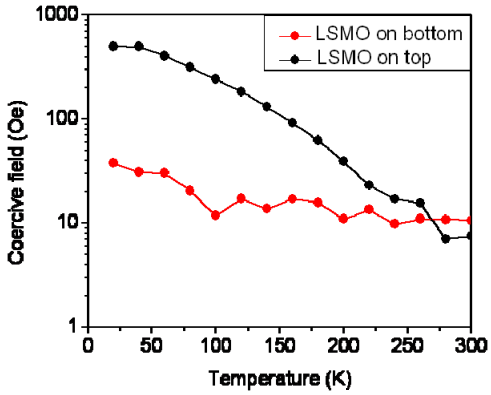

Figure 3.7. Coercive field extracted from the easy-axes magnetic hysteresis magnetic loop as a function of temperature of a [LSMO 25 nm/ BTO 4.4 nm] (red curve) and [BTO 4.4. nm/ LSMO 5nm] (black curve) bilayers.

We have extracted coercive field (H_c) from the easy axes ([110]) hysteresis magnetic loops at different temperatures for each bilayers (Figure 3.7). H_c decreases while increasing temperature for both samples. Sample with LSMO on top (black curve) has larger H_c below 275 K, above this temperature it is impossible to distinguish which H_c is larger, because 10 Oe is near the resolution of the VSM magnetometer. Although H_c from different bilayers are practically the same above 200 K, it is possible to achieve an antiparallel state for a large temperature range.

3.2 Transport properties

Resistivity measured in Van der Pauw geometry as a function of temperature of a [LSMO 25nm/BTO 4.4 nm] bilayer is shown in Figure 3.8. The sample was cool down with no applied magnetic field. It is observed a metallic behavior for the whole temperature range in good agreement with a Curier temperature higher than room temperature. The resistivity value at 10 K is $1.45 \cdot 10^{-4}$ mΩ·cm similar to bulk LSMO values [11]

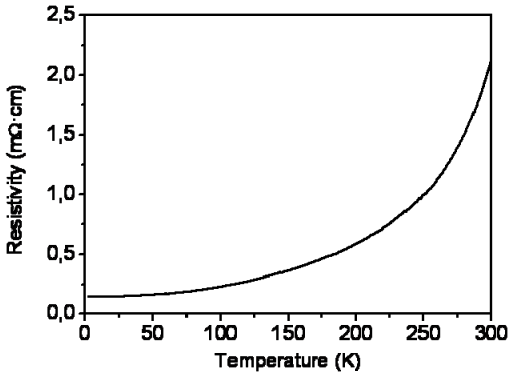

Figure 3.8. Resistivity as a function of temperature measured in Van der Pauw geometry of a [LSMO 25 nm/ BTO 4.4 nm].

4 Piezoresponse Force Microscopy

Characterizing the ferroelectric properties at the nanoscale is challenging. In thick perfect insulator ferroelectric layers with a negligible leakage current it can be measured standard ferroelectric polarization versus electric field hysteresis loops (P(E)). In films of a few nanometers, the tunnel currents is too high to characterize using this method. Only some groups have reported P(E) in nanometric ferroelectric capacitors using BTO 3.5 nm at 77 K [38], and 5nm at room temperature [39]. Piezoresponse force microscopy (PFM) is a more suitable technique to probe ferroelectricity in ultrathin films. Several recent works have demonstrated ferroelectricity at the nanoscale in different systems using PFM [40, 41, 8, 31].

We have measured local PFM hysteresis loop at room temperature, to analyze ferroelectric properties of [LSMO/BTO] bilayers varying BTO thicknesses. We have sputtered a millimeter size Pt spot in one corner of the sample to contact the LSMO electrode, and we have grounded it. During measurement it is applied a 0.7 V amplitude ac voltage at 52 kHz, and dc voltage is ramped in steps of duration t= 60 ms, and the piezoresponse is measured until the voltage is changed. Measurements have been done on contact-mode, typical applied contact forces were around 200 nN. These forces are sufficiently weak to avoid any significant local depolarization, but sufficiently high to ensure a proper contact to minimize electrostatic contributions to the PFM signal. Phase, amplitude and topography signals were recorded simultaneously. We verified that the poling doesn't influence the surface topography, and we checked the conductivity of the platinum coated tip before and after all measurements to assure that the tip was not damaged.

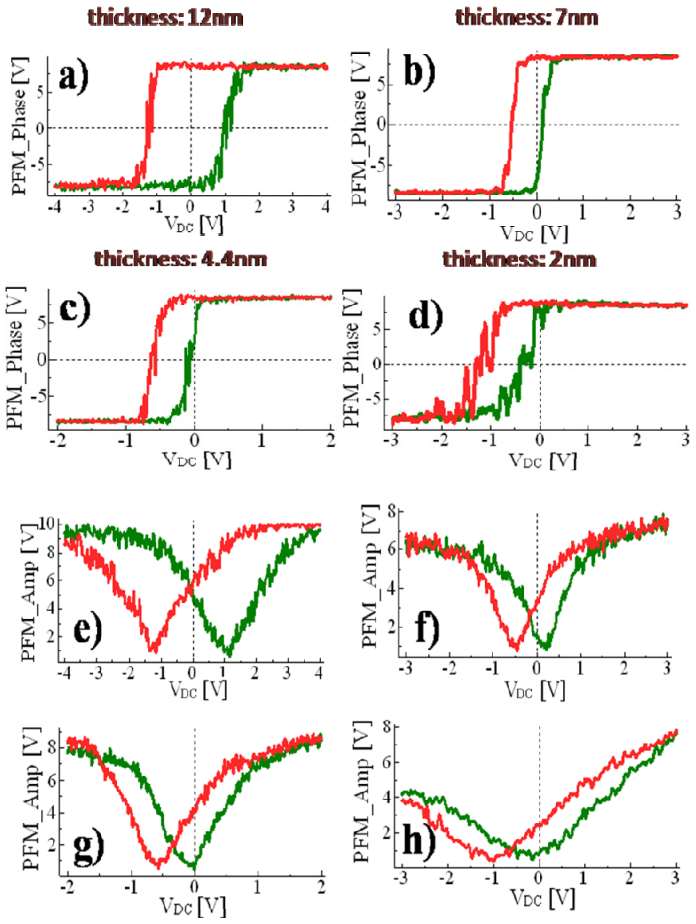

Figure 3.9 PFM phase (a-d) and amplitude (e-h) hysteresis loop for 12, 7, 4.4 and 2 nm BTO thicknesses at room temperature**.**

In figure 3.9 is shown PFM amplitude hysteresis loops for [LSMO 15nm/ BTO t nm] (t= 12 (e), 7 (f), 4.4 (g), 2 (h)). The butterfly-like shape of the loops indicates that the BaTiO3 layer is still ferroelectric at thickness of 2nm. PFM phase hysteresis loop (Fig 3.9 (a-d)) shows ferroelectric polarization reversals. Complete 180º phase contrast (from -8 V to 8 V in the looking amplifier) indicates that the polarizations are antiparallel in the two states. Decreasing BTO thickness, the hysteresis area is reduced because smaller electric fields are needed to switch polarization. It is also observed an asymmetry in the phase and amplitude loops which reveals a preferential polarization direction pointing

downward. Ferroelectric polarization preferential direction have been shown in BTO ultrathin-films grow on LSMO buffered $SrTiO_3$ substrates due to the screening of the polarization charges by the surface adsorbates [42, 43] but in these cases the preferential direction was pointing upward. An explanation of this negative imprint could be the presence of an internal built-in electric field at the BTO/LSMO interface, which is not polarization dependent and is always pointing in one direction. This internal electric field can be generated by a polar interface [34] or by the presence of oxygen vacancies at the interface [44], these oxygen vacancies generate an electron dopping effect which produces an "in-situ" screening of the ferroelectric polarization charges. Other mechanism could be the mechanical stress exerted on the BTO film by the probing tip. It is known that this compressive mechanical stress in the direction normal to the film surface can produce internal electric field in the ferroelectric ultrathin films due to the flexoelectricity effect produced by the strain gradients high enough to switch ferroelectric polarization [42]. Recent report shows that the flexoelectricity effect creates an uniaxial imprint in ferroelectric thin films assisting a preferential polarization direction [45]. The asymmetry of the boundary conditions at the top and bottom interfaces in the tip/film/electrode heterostructure could be another explanation. Although the presence of oxygen vacancies is the most probable mechanism of this switching asymmetry, the absence of a top electrode, and the impossibility of reduce the applying force, it is complicate to conclude the origin of this effect [46].

5 Summary

In summary we are able to grow high quality ferroelectric/ferromagnetic epitaxial heterostructures with sharp interfaces. Magnetic and transport properties of the LSMO layers are near the bulk ones. It is possible to achieve different coercive fields applying the magnetic field in the [110] easy-axis and growing LSMO layers with different thicknesses. Ferroelectricity in BTO ultrathin films persists down 4.4 nm thick, leading the possibility to fabricate tunnel junctions with an active barrier. The BTO ultrathin ferroelectric layers grown on LSMO buffered layer presents a preferential downward ferroelectric polarization direction indicating the presence of oxygen vacancies.

6 References

[1] N. A. Spaldin, and M. Fiebig, *Science* **309,** 391 (2005).

[2] C. A. F. Vaz, J. Hoffman, C. H. Ahn, and R. Ramesh, *Adv. Mater*. **22**, 2900 (2010).

[3] J. Park, E. Vescovo, H. Kim, C. Kwon, R. Ramesh, and T. Venkatesan, *Nature (London)* **392**, 794 (1998).

[4] E. Dagotto, T. Hotta, and A. Moreo, *Phys. Rep*. **344**, 1 (2001).

[5] C. H. Ahn, J.-M. Triscone, and J. Mannhart, *Nature* **424**, 1015 (2003).

[6] J. D. Burton, and E.Y. Tsymbal, *Phys. Rev. B* **80**, 174406 (2009).

[7] K. J. Choi, M. Biegalski, Y. L. Li A Sharan, J. Schubert, R. Uecker, P. Reiche, Y. B. Chen, X. Q. Pan, V. Gopalan, L.-Q. Chen, D. G. Schlom, and C. B. Eom, *Science* **306**, 1005 (2004).

[8] V. Garcia, S. Fusil, K. Bouzehouane, S. Enouz-Vedrenne, N. Mathur, A. Barthélémy, and M. Bibes, *Nature* **460**, 81 (2009).

[9] J. Mannhart, and D. G. Schlom, *Science* **327** 1607 (2010).

[10] W. Eerenstein, N. D. Mathur, and J. F. Scott, *Nature* **442**, 759 (2006).

[11] A. Urushibara, Y. Moritomo, T. Arima, A. Asamitsu, G. Kido, and Y. Tokura, *Phys. Rev. B* **51**, 14103 (1995).

[12] M. B. Salamon, and M. Jaime, *Rev. Mod. Phys.* **73**, 583 (2001).

[13] H. Fujishiro, M. Ikebe, and Y. Konno, *J. Phys. Soc. Jpn.* **67**, 1799 (1998).

[14] J. M. D. Coey, M. Viret, and S. von Molnar, *Adv. Phys.* **48**, 167 (1999)

[15] Y. Tokura, and N. Nagaosa, *Science* **288**, 462 (2000).

[16] Y. Konishi, Z. Fang, M. Izumi, T. Manako, M. Kasai, H. Kuwahara, M. Kawasaki, K. Terakura, and Y. Tokura, *J. Phys. Soc. Jpn.* **68**, 3790 (1999).

[17] M. Huijben, L. W. Martin, Y.-H. Chu, M. B. Holcomb, P. Yu, G. Rijnders, D. H. A. Blank, and R. Ramesh, *Phys. Rev. B* **78**, 094413 (2008).

[18] T. Becker, C. Streng, Y. Luo, V. Moshnyaga, B. Damaschke, N. Shannon, and K. Samwer, *Phys. Rev. Lett.* **89**, 237203 (2002).

[19] M. Bibes, S. Valencia, L. Balcells, B. Martinez, J. Fontcuberta, M. Wojcik, S. Nadolski, and E. Jedryka, *Phys. Rev. B* **66**, 134416 (2002).

[20] M. Bibes, L. Balcells, S. Valencia, J. Fontcuberta, M. Wojcik, E. Jedryka, and S. Nadolski, *Phys. Rev. Lett*. **87**, 067210 (2001).

[21] A. Tebano, C. Aruta, S. Sanna, P. G. Medaglia, G. Balestrino, A. A. Sidorenko, R. D. Renzi, G. Ghiringhelli, L. Braicovich, V. Bisogni, and N. B. Brookes, *Phys. Rev. Lett*. **100**, 137401 (2008)]

[22] J. J. Wang, F. Y. Meng, X. Q. Ma, M. X. Xu, and L. Q. Chen, *J. Appl. Phys.* **108**, 034107 (2010).

[23] T. Kolodiazhnyi, M. Tachibana, H. Kawaji, J. Hwang, and E. Takayama-Muromachi, *Phys. Rev. Lett*. **104**, 147602 (2010).

[24] J. Hwang, T. Kolodiazhnyi, J. Yang, and M. Couillard, *Phys. Rev. B* **82**, 214109 (2010).

[25] Y. Wang, X. Liu, J. D. Burton, S. S. Jaswal, and E. Y. Tsymbal, *Phys. Rev. Lett.* **109**, 247601 (2012).

[26] N. Sai, A. M. Kolpak, and A. M. Rappe, *Phys. Rev. B* **72**, 020101 (2005).

[27] J. Junquera, and P. Ghosez, *Nature* **422**, 506 (2003).

[28] R. Nakao, K. Ishizumi, I. Takahashi, H. Terauchi, Y. Hayafuji, and K. Miura, *Appl. Phys. Lett*. **86**, 222901 (2005).

[29] G. Gerra, A. K. Tagantsev, N. Setter, and K. Parlinski, *Phys. Rev. Lett*. **96**, 107603 (2006).

[30] X. Y. Wang, Y. L. Wang, and R. J. Yang, *Appl. Phys. Lett*. **95**, 142910 (2009).

[31] A. Gruverman, D. Wu, M. Lu, Y. Wang, H.W. Jang, C. M. Folkman, M.Y. Zhuravlev, D. Felker, M. Rzchowski, C.-B. Eom, and E.Y. Tsymbal, *Nano Letters* **9**, 3539 (2009).

[32] Y. W. Yin, J. D. Burton, Y-M. Kim, A. Y. Borisevich, S. J. Pennycook, S. M. Yang, T. W. Noh, A. Gruverman, X. G. Li, E. Y. Tsymbal, and Qi Li. *Nature Mater.* **12**, 397 (2013).

[33] C.-G. Duan, R. F. Sabirianov, W.-N. Mei, S. S. Jaswal, and E. Y. Tsymbal, *Nano Letters* **6**, 483 (2006).

[34] X. Liu, Y. Wang, P. V. Lukashev, J. D. Burton, and E. Y. Tsymbal, *Phys Rev. B* **85**, 125407 (2012).

[35] M. Bibes, J. Villegas, and A. Barthelemy, *Adv. Phys.* **60**, 5 (2011).

[36] L. M. Berndt, V. Balbarin, and Y. Suzuki, *Appl. Phys. Lett*. **77**, 2903 (2000).

[37] E. C. Stoner, and E. P. Wohlfarth, *Phil. Trans. R. Soc. London A* **240**, 599 (1948).

[38] A. Petraru, H. Kohlstedt, U. Poppe, R. Waser, A. Solbach, U. Klemradt, J. Schubert, W. Zander, and N. A. Pertsev, *Appl. Phys. Lett*. **93**, 072902 (2008).

[39] Y. S. Kim, D. H. Kim, J. D. Kim, Y. J. Change, T. W. Noh, J. H. Kong, K. Char, Y. D. Park, S. D. Bu, J.-G. Yoon, and J.-S. Chung, *Appl. Phys. Lett*. **86**, 102907 (2005).

[40] H. Bea, S. Fusil, K. Bouzehouane, M. Bibes, M. Sirena, G. Herranz, E. Jacquet, J.-P. Contour, and A. Barthelemy, *Jpn. J. Appl. Phys*. **45**, L187 (2006).

[41] Y. H. Chu, T. Zhao, M. P. Cruz, Q. Zhan, P. L. Yang, L. W. Martin, M. Huijben, C. H. Yang, F. Zavaliche, H. Zheng, and R. Ramesh, *Appl. Phys. Lett*. **90**, 252906 (2007).

[42] H. Lu, C.-W. Bark, D. Esque de los Ojos, J. Alcala, C. B. Eom, G. Catalan, and A. Gruverman, *Science* **336**, 59 (2012).

[43] H. Lu, D. J. Kim, C.-W. Bark, S. Ryu, C. B. Eom, E. Y. Tsymbal, and A. Gruverman, *Nano Lett*. **12**, 6289 (2012).

[44] A. Y. Borisevich, A. R. Lupini, J. He, E. A. Eliseev, A. N. Morozovska, G. S. Svechnikof, P. Yu, Y. -H. Chu, R. Ramesh, S. T. Pantelides, S. V. Kailinin, and S. J. Pennycook, *Phys. Rev. B* **86**, 140102(R) (2012).

[45] D. D. Fong, A. M. Kolpak, J. A. Eastman, S. K. Streiffer, P. H. Fuoss, G. B. Stephenson, C. Thompson, D. M. Kim, K. J. Choi, C. B. Eom, I. Grinberg, and A. M. Rappe, *Phys Rev Lett.* **96**, 127601 (2006).

[46] A. Gruverman, A. Kholkin, A. Kingon, and H. Tokumoto, *Appl. Phys. Lett*. **78**, 2751 (2001).

4

$La_{0.7}Sr_{0.3}MnO_3$/ $BaTiO_3$/ $La_{0.7}Sr_{0.3}MnO_3$ Magnetic Tunnel Junctions

During last decade, research on magnetic tunnel junctions (MTJs) based on transition metal-oxide has been intense due to their multifunctional properties [1]. The rich physics of transition metal oxides resulting in this wide variety of properties is related to the delicate balance between charge, spin and orbital degrees of freedom [2, 3]. The possibility of use these functionalities as "active" barrier brings the opportunity to create new concept tunnel devices. For example it has been fabricated spin-filters using a ferromagnetic insulator such $BiMnO_3$ [4] or multi-state devices using ferroelectric [5] or multiferroic oxides [6]. Many complex oxides belong to the same perovskite structural family with similar lattice parameters, allowing for the growth of high quality epitaxial heterostructures. Combining this materials can be generate novel interfacial phases which may completely differ from those of the constituent materials alone [7]. Because of the high sensitivity of tunnel conductance to the metal/insulator interface, MTJs appears as very appropriate architectures to exploit such novel interface effects in practical devices or to study the interplay between two different physical properties (i.e ferroelectricity and ferromagnetism).

1 Introduction

The first motivation to use transition-metal oxides in MTJs was obtain very large Tunnel Magnetoresistance (TMR) using highly polarized ferromagnetic electrodes such half-metallic manganites. The first TMR measurement on MTJs with manganite electrodes was reported in 1996 by Lu *et al.* [8] and Sun *et al.* [9]. A maximum TMR of 83% was found [8] (at 4.2 K), which, according to Jullière formula [10], corresponds to a spin polarization (P) of 54% for the LSMO electrodes. Later, other authors reported increased TMR. Sun *et al.* reported a TMR of ~ 400%, corresponding to P ~ 81% [11]. This was soon followed by Viret *et al.*'s paper, which independently reported a 450% TMR at 4.2 K in LSMO/STO/LSMO junctions [12]. Subsequent publications by Sun *et al.* and others reported increasingly large TMR values, up to a TMR of 1850% in an LSMO/STO/LSMO MTJ, as found by Bowen et al. in 2003 [13]. This record TMR corresponds to a spin polarization of 95%, i.e., a virtually half metallic character for LSMO.

In early manganite tunnel junctions, the TMR decreased rather rapidly with temperature and disappeared at a critical temperature T^* (typically 200 K) that is well below the Curie temperature of the electrodes (up to 360 K in LSMO). Several explanations have been invoked to explain the difference between T^* and T_C: defects in the tunnel barrier causing spin flips [14, 15] and non-optimal magnetic properties at manganite/barrier interfaces (either due to oxygen deficiency [12], or phase separation [16]. Bruno et al. have recently reported an induced Ti magnetic moment at the LSMO/STO interface [17]. This Ti magnetic moment is coupling antiferromagnetic via superexchange interaction with Mn magnetic moment. Similar magnetic reconstruction in $La_{0.7}Ca_{0.3}MnO_3/PrBa_2\ Cu_3O_7$ has been found [18]. In the last system, the induced Cu magnetic moment coupled antiferromagnetically with Mn has been demonstrated that produce a strong influence in the TMR values, and its dependence with temperature [19]. In this chapter we are going to investigate the spin dependent transport in MTJs with both LSMO ferromagnetic electrodes and BTO ferroelectric barrier, and we are going to explore the influence of the reconstruction at the LSMO/BTO interface.

2 Tunnelling current properties through a $BaTiO_3$ barrier

We have patterned [LSMO 25 nm)/BTO (x nm)/LSMO 10 nm] trilayers with BTO thicknesses x = 4.0, 4.4 and 4.8 nm into MTJs and measured their magnetotransport properties. The patterning process was carried out by standard UV photolithography techniques and Ar ion milling (see chapter 2). We have defined 8 pillars which sizes were 9x18 μm^2 and 5x10 μm^2. After completing the patterning process MTJs resistance was checked at room temperature. Between 1 and 3 junctions per sample could be measured, which means that our patterning process has a large success ratio of near 40%.

2.1 Electrode properties

Before study magneto-transport properties, we must check our LSMO/BTO/LSMO devices were not damaged during the patterning process, and verify transport tunnelling properties. Figure 4.1 (a) shows resistance vs. temperature measurements for the bottom electrode (left) in the two-contact configuration at 10 mV. We observe that the bottom electrode resistance shows metallic behavior (dR/dT>0) typical of a manganite in this temperature range (black curve). The electrode resistance decreases from ~1kΩ at room temperature to ~100 Ω at 15 K; these values scale in very good agreement with the resistivity (red curve) of a sample with the same LSMO thickness, confirming that the bottom electrode was not damaged during the patterning process. The slightly difference between resistivity and electrode resistance at low temperature could be due to a thermoelectric effect, which occurs cooling the sample during the measurement. Current as a function of voltage of LSMO bottom electrode at 20 K (Fig 4.1 (b)) shows a clear linear dependence, which means that the LSMO/Ag interface is an ohmic contact.

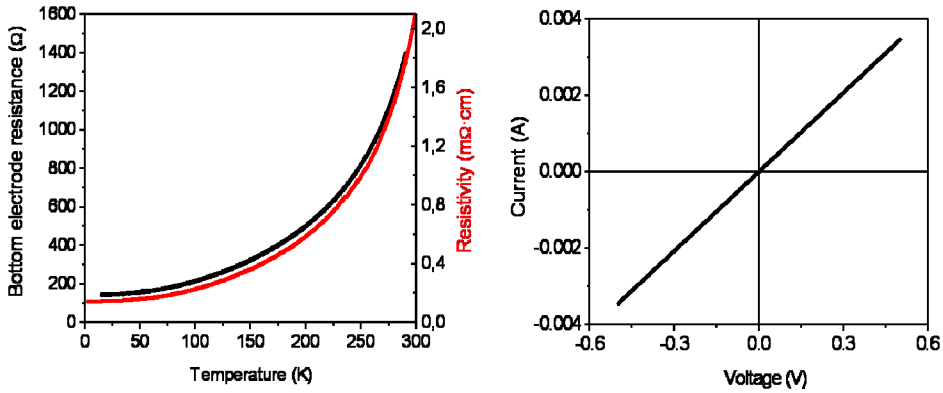

Figure 4.1 (a) Resistance versus temperature at 10mV of the 25 nm bottom electrode (black curve) measured in 2-points configurations and resistivity versus temperature of a [LSMO 25nm / BTO 4.4nm] bilayer (red curve) measured in Van der Pauw configuration. (b) Current versus applied bias voltage at 20 K of the 25 nm bottom electrode measured in the 2-points configuration.

2.2 Resistance vs. barrier thickness. Brickman model

In Figure 4.2 (right) is shown junction resistance as a function of BTO barrier thickness at 10 mV at room temperature. The junction resistance increases exponentially with barrier thickness which is an indication of tunneling transport through the BTO layer. Additional information about tunneling transport is given by the relation between tunneling current and the applied bias. Current as a function of applied voltage at low temperature for a 4.4 nm thick BTO barrier (Fig. 4.2 (left)) presents clearly non-linear behavior.

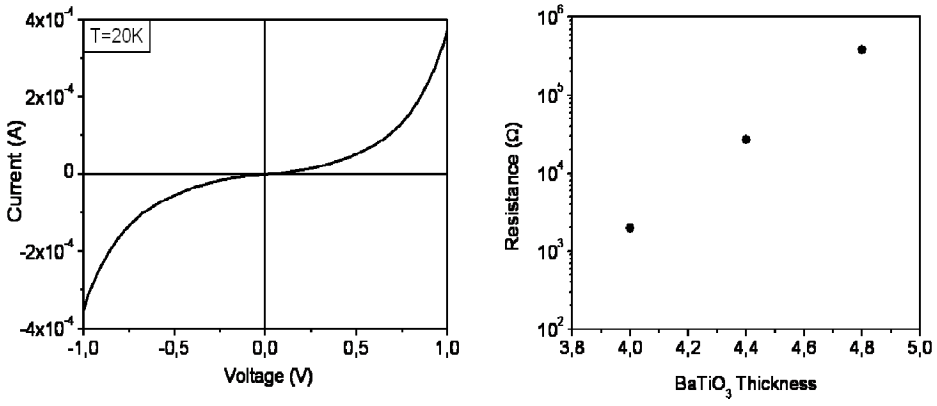

Figure 4.2. (left) Current versus applied voltage at 20 K of a 5x10 μm^2 [LSMO 25nm / BTO 4.4 nm/ LSMO 10 nm] magnetic tunnel junction. (right) Resistance as a function of nominal BTO barrier thickness at 10 mV at 300 K.

To model MTJs with ferroelectric barrier is commonly used a trapezoidal potential barrier [20]. We have used this asymmetric tunneling barrier model [21] to extract the barrier thickness, average height, and heights asymmetry. We fitted the current curves considering measurements were the applied voltage was below 80 mV. The barrier thickness obtained from the fit is between 3.7 and 3.9 nm slightly smaller than the expected value (4.4 nm). The obtained values of the barrier average height are between 0.17-0.18 eV, and the barrier height asymmetry is -0.2 eV. The fitted parameters are represented in Figure 4.3. In this picture is clearly shown a strong asymmetry probably produced by the spontaneous polarization [22] that in our case is preferentially pointing down as we have observed in the PFM measurements (see chapter 3). The effect of the ferroelectric polarization in the tunneling parameters will be discussed extensively in chapter 5. Comparable height values have been obtained in similar LSMO/BTO tunnel junctions [23], and in junction with SrTiO3 barrier [11, 24, 14, 25]. It is remarkable that although our system has a symmetric structure with both LSMO electrodes, a strong interface asymmetry have been obtained.

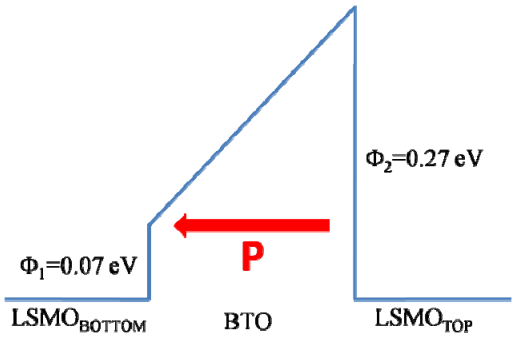

Figure 4.3. Barrier potential diagram of the LSMO/BTO/LSMO MTJ using the fitted parameters from the I(V) curves. The BTO ferroelectric polarization (P) is preferentially downward

2.3 Resistance vs. Temperature

Fig 4.4 shows resistance of a 5x10 μm^2 junction with 4.4 nm barrier thickness as a function of temperature. The sample were cool down applying a magnetic field of 4200 Oe along the electrodes easy-axis ([110] direction). Junction resistance increases while lowering temperature, showing a maximum near 155-160 K. Below this temperature the resistance drops to a final value around two times smaller being stronger at low bias. This temperature dependence is common in MTJ with both manganite electrodes [26, 27], and also have been observed in similar structure [28]. In Reference 27 it is shown that the resistance of defect-free junctions of oxygen displays a weak temperature variation (2 times or less). On the other hand, the resistance of oxygen deficient tunnel junctions presents a strong temperature variation (two orders of magnitude temperature variation). Resistance measured at 2 different voltages has different values, implying a non linear I-V characteristic for the whole temperature range. Note that the junction resistance is higher (nearly 2 orders of magnitude at low temperature) than bottom electrode resistance for the whole temperature range, so an artificial TMR values due to an inhomogeneous current injection across the barrier can be rejected.

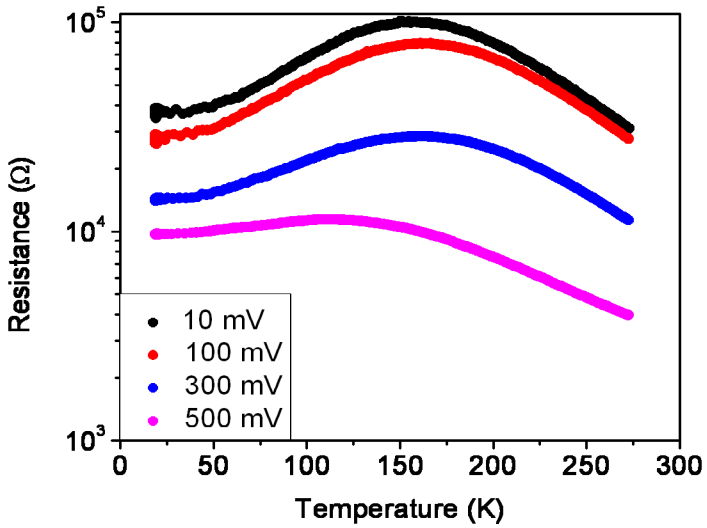

Figure 4.4. Resistance vs. temperature measured at 10 mV (black), 100 mV (red), 300 mV (blue) and 500 mV (magenta) for a 5x10 μm^2 [LSMO 25nm / BTO 4.4 nm/ LSMO 10 nm] magnetic tunnel junction.

3 Magnetotransport measurements

We have studied junction resistance as a function of magnetic field sweeps. Several junctions from different samples with identical nominal 4.4 nm thicknesses were measured at different temperatures. Figure 4.5 (left) shows resistance versus magnetic field sweeps at 14 K applying 800 mV. In this measurements the field was set to 4.2 kOe at the beginning to saturate the magnetization of both electrodes (parallel alignment) and then the magnetic field was swept following the sequence 4200→ -4200 (black curve) → 4200 Oe (red curve). In order to improve antiparallel alignment of the magnetization direction of the LSMO electrodes, the long side of the rectangle of the junction pillar was aligned in the [110] taking advantage of shape anisotropy. Resistance presents abrupt jumps when the magnetization direction of the bottom electrode reversals. For magnetic field higher than the coercive field of the bottom electrode and smaller than the coercive field of the top electrode, magnetizations of

ferromagnetic electrodes are aligned antiparallel. This state is stable, and presents larger resistance than the parallel state. Because LSMO are half metals with high positive spin polarization, this positive tunnel magnetoresistance is expected [13]. When we increase the magnetic field up the top electrode coercive field, the resistance value drops, and once again we get the parallel state. We calculate tunnel magneto-resistance (TMR) that was defined as TMR = (R_{AP} - R_P) / R_P where R_{AP} and R_P were respectively the tunnel resistances in the antiparallel (AP) and parallel (P) magnetization configurations. Applying different bias we have obtained different TMR amplitudes; we will discuss it bellow in this section. In the right part of Figure 4.5, it is shown the magnetic field dependence of the bottom electrode resistance at 14 K. Resistance values and magnetoresistive ratio are much smaller than the ones from MTJs (Fig 4.5 left).

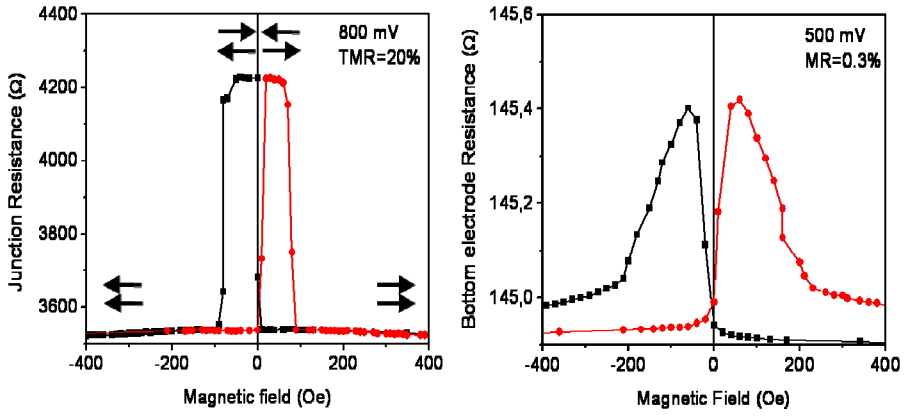

Figure 4.5. (left) Junction resistance versus applied magnetic field sweeping from 4200 Oe to -4200 Oe (black) and from -4200 Oe to 4200 Oe (red) at 14 K measured at 800 mV. Black arrows indicate magnetizations directions from top and bottom ferromagnetic electrodes. (right) Bottom electrode resistance versus magnetic field sweeping. Note that magnetoresistance is extremely small.

To better characterize the spin-dependent transport mechanisms, I(V) curves in P and AP state where measured (Figure 4.6 left). The I(V) curves are non-linear as expected for a tunneling transport mechanism; the current in P state is for the whole voltage range larger than in the AP state resulting in a positive TMR. We have obtained conductance as the

numerical derivative of current vs. voltage (Figure 4.6 right). Ideally, the conductance of a tunnel junction has a parabolic dependence on voltage at low bias [29], but in our case we observe staircase dependence, and it seems to be more intense in the AP state. This unusual behavior could be related with the Coulomb blockade charging effect [30, 31]. Coulomb blockade effect appears in systems with two main electrodes, and a metallic grain embedded inside an insulating barrier. If the capacitance of the grain is small enough (nanometer size), a discretization of charging energy arises. When an electron tunnels into the grain, the grain energy increases $e^2/2C$, where e is the electron charge and C is the grain capacitance. Under this condition the current flow is blocked unless the bias voltage overcomes charging energy. This provides an oscillatory behavior in tunneling conductance. This effect is stronger at low temperatures and at low applied bias. Coulomb blockade was very extensively studied in nonmagnetic system such single electron transistors devices [32]. Interplay between spin dependent transport and the Coulomb Blockade was theoretically studied in system with at least one magnetic electrode and a magnetic grain [30], or two magnetic electrodes and a non magnetic grain [31, 33], in both cases an oscillatory TMR due to the different tunnel conductance in the parallel and antiparallel state is predicted. The oscillations amplitude decreases with increasing voltage, and it also decreases with increasing temperature, disappearing when the thermal energy is of the order of the charging energy. This magnetoresistance behavior has been observed in granular CoAlO nanobridges [34] and in epitaxial Fe nanoparticles sandwiched between MgO insulator barriers with Fe and Co ferromagnetic electrodes double magnetic tunnel junctions [35].

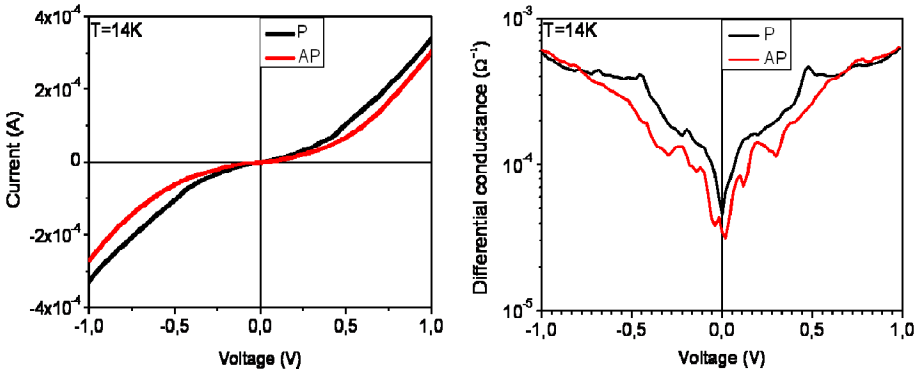

Figure 4.6 (left) Tunnelling current as a function of applied bias at parallel (black curve) and antiparallel (red curve) magnetic state at 14 K. (right) Differential conductance obtained as the numerical derivative of current vs. voltage at parallel (black curve) and antiparallel (red curve) magnetic state at 14 K.

We have calculated TMR from I(V) characteristic as TMR= $(I_p-I_{ap})/I_{ap}$, where I_{ap} (I_p) is the tunnelling current in the antiparallel (parallel) magnetic state. We have also obtained TMR from resistance vs. magnetic field sweeps (R(H)) and we have represented them as a function of applied bias (Figure 4.7). TMR values from R(H) (red symbols) are in excellent agreement with TMR from I(V) (black symbols). Figure 4.7 shows an oscillatory dependence of the TMR with bias, with a large suppression at very low bias at 14 K. The maximum TMR value at this temperature is near 100% at 50 mV. The oscillation amplitude is reduced when bias voltage is increased as it is expected in a Coulomb blockade scenario [30]. The TMR low bias suppression may be is also related with spin filtering effect as we will discuss in chapter 5.

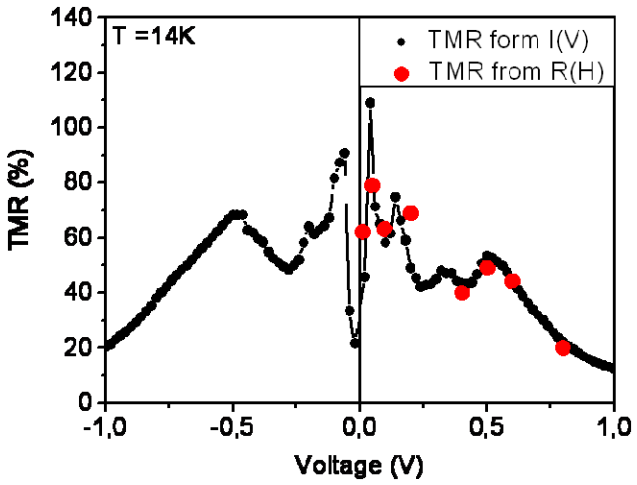

Figure 4.7. Tunnel magnetoresistance (TMR) versus applied bias at 14K obtained from I-V curves (black curve) and from resistance versus magnetic field sweeps (red points).

In order to explore the temperature dependence of this oscillation, we have calculated TMR (Fig 4.8 a-d) and conductance (Fig 4.9 e-h) from I(V) curves at different temperatures. In both cases when temperature increases the oscillations amplitude decrease strongly and they practically vanish at 100 K, this means that both oscillatory behaviour should be related. The TMR and conductance oscillatory behavior as a function of applied bias and temperature are in good agreement with the Coulomb blockade scenario. It is also remarkable that while increasing temperature, the low bias suppression disappears, reaching at 100 K TMR values larger than 200%. This TMR values are as large as the largest obtained with manganite electrodes at this temperature [13] according with the half-metallicity nature of the LSMO electrodes. This high spin polarization at the interface reflects the good interface quality of our samples.

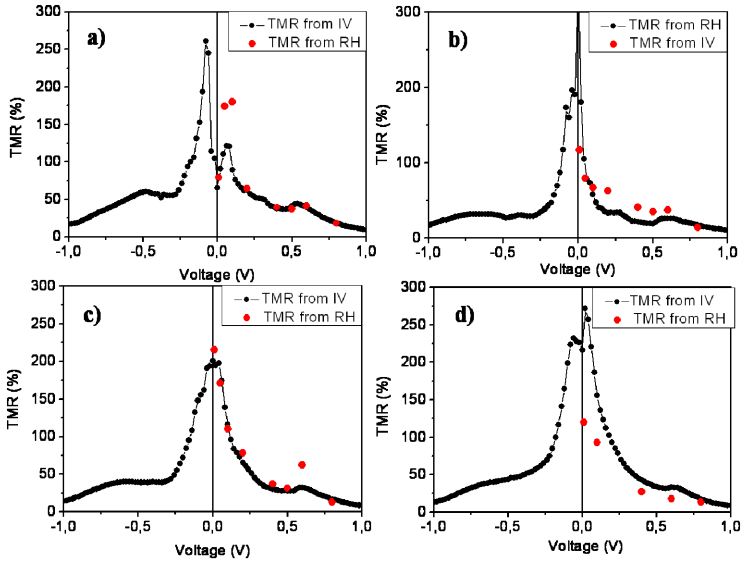

Figure 4.8. Tunnel magnetoresistance (TMR) versus applied bias at 40 K (a), 60 K (b), 80 K (c) and 100 K (d) obtained from I-V curves (black curve) and from resistance versus magnetic field sweeps (red points).

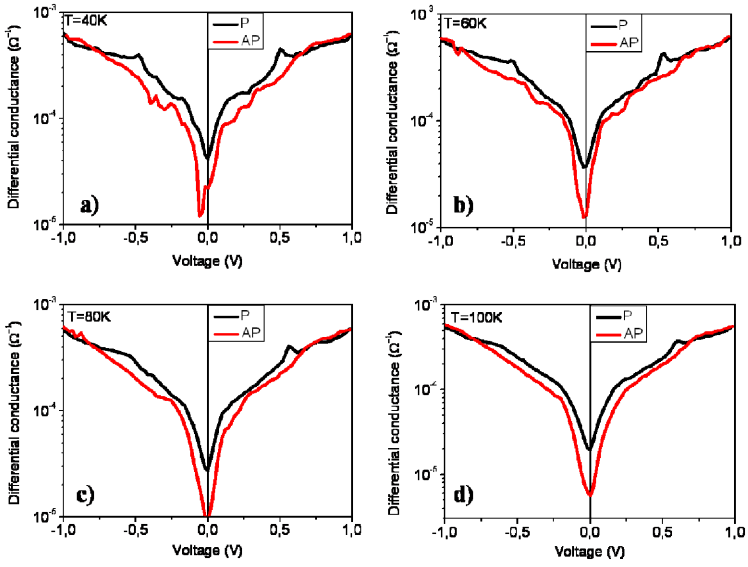

Figure 4.9. Differential conductance obtained as the numerical derivative of current vs. voltage at parallel (black curve) and antiparallel (red curve) magnetic state at 40 K (a), 60 K (b), 80 K (c) and 100 K (d).

In another junction of the same sample we have found none or negligible low bias TMR suppression at low temperatures, obtaining values near 800 %. TMR values drop quickly with applied bias, at 100 mV TMR= 400% and for larger bias TMR near 50 % are achieved (Figure 4.10). Using Julliere formula [10] we can calculate the spin polarization of our system assuming that both electrodes has the same spin assymetry. TMR=786% correspond a high spin polarization of 89% characteristic of half metallic systems [13]. Unfortunately we couldn't characterize properly because this junction stopped to work after few measurements.

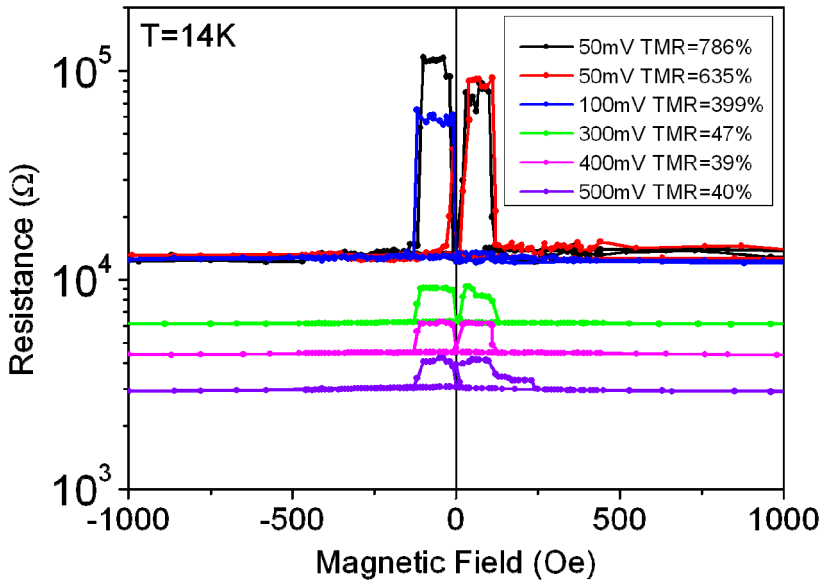

Figure 4.10. Junction resistance versus applied magnetic field sweeping at 14 K measured at 50 mV (black and red), 100 mV (blue), 300 mV (green), 400 mV (magenta), 500 mV (violet).

Although the Coulomb blockade scenario explains most of the magnetotransport properties, it is clearly unexpected in these systems. Because it requires metallic cluster embedded in the insulator barrier, we should found more experimental facts that complement these results.

4 STEM EELS oxygen vacancies analysis

Metallic clusters must be small enough, so that charging energy $e^2/2C$ overcomes thermal energy. The typical size to achieve this condition is a few nanometers, so we should employ a technique with nanometric or subnanometric resolutions. STEM with simultaneous EELS is a suitable technique because it has high spatial resolution and it provides chemical contrast. Three possible mechanism could contribute to originate metallic clusters, chemical diffusion into the BTO layer (i.e. La doping), charge transfer from manganite electrodes into the titanate layer, or BTO self-doping via oxygen vacancies. In chapter 3 (Figure 3.3) we have demonstrated that chemical interdiffusion is negligible, so we have can reject this mechanism. Charge leakage from manganite to titanate have been probed in different system such LaMnO3/SrTiO3 [36] and in La0.7Sr0.3MnO3/SrTiO3 [16]. In both cases the origin of the charge transfer seems to be the extra La-O or $La_{0.7}Sr_{0.3}O$ extra plane at both interfaces. These extra layers have, on average, a donor character reducing the Ti oxidation state. In Figure 4.11 (c) we show Ti oxidation state profile across a 4.4 nm BTO layer sandwiched between two LSMO of a $[\text{LSMO 7 nm/ BTO 4.4nm}]_{x4}$ superlattice. This profile has been obtained as the average of the spectrum image red extracted from the selected area of the ADF image (Fig 4.11 (b)). The growth direction is from the right side of the plot to the left side, this means that the right side corresponds to the BTO/LSMO bottom interface, and the left side correspond to the LSMO/BTO top interface. We have utilized a method based on the spatial-difference technique [37] where the measured Ti $L_{2,3}$ edge is refined through a multiple linear least-squares fit (MLLS) to the reference spectra of $LaTiO_3$ (Ti^{+3}) and $BaTiO_3$ (Ti^{+4}). The MLLS fit coefficients through the EELS images represent the respective Ti^{+3}/Ti^{+4} weights, allowing spatial mapping of the Ti oxidation state [38]. In figure 4.11(b) we can see a clear reduction in the bottom interface from nominal +4 to +3.9. It's important to remark that although we have the same symmetric interfaces the charge is localized at the bottom one, this means that another source of doping agent in BTO must be involved. We have analyzed the oxygen K edge signal, which is proportional to the number of oxygen atoms in the same area (Figure 4.11 (d)) obtaining a clear decrease of the intensity in the bottom interface which can be related to the existence of oxygen vacancies at this interface. Although the reduction in Ti oxidation state is systematic in these

samples, the decreasing of the oxygen K edge signal isn't always observed. It doesn't mean that there are not oxygen vacancies but the amount of them is not large enough to resolve with the STEM-EELS technique. Note that the oscillations of both plots (Figure 4.11 (c) and (d)) are due to the atomic resolution of the EELS spectrum image and the actual are correspond to the maxima. The increasing of oxygen vacancies at the bottom interface is in good agreement with the reduction of Ti at the same interface because one oxygen vacancy adds two electrons to the empty conduction band of the BTO reducing the nominal Ti^{+4} state. Oxygen vacancies cluster have been predicted in different complex oxides [39], and experimentally observed [40]. If the vacancy correlations are larger than the interaction length of the electron gas the cluster configuration is more stable than a homogeneous distribution [40]. We couldn't resolved directly vacancy clusters, probably because the oxygen vacancy is less than 1% [40], but may be because the oxygen vacancies are not homogeneously distributed, a cluster configuration could be stabilize.

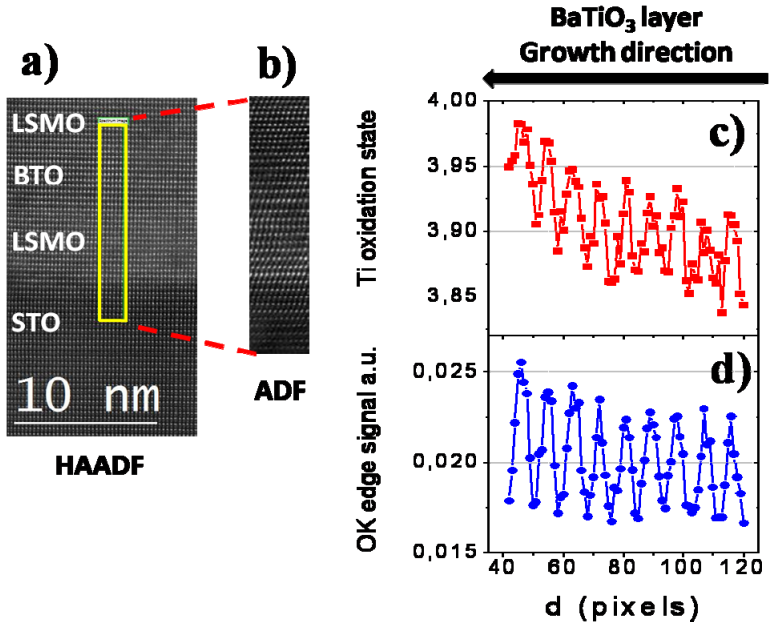

Figure 4.11. (a) High magnification HAADF image of a [LSMO 7 nm / BTO 4 nm]x4 superlattice. (b) Simultaneous annular dark field ADF images during spectrum images. (c) Ti oxidation state profile across the BTO layer, obtained from Ti L_{23} EELS edge. (d) Oxygen K edge EELS signal across the BTO layer.

We have studied the tunneling transport in a [LSMO 25 nm)/BTO 4.4 nm/ Ag] tunnel junction (more details about the fabrication process of this device are in chapter 5 section 5). Junction resistance of a LSMO/BTO bilayer as a function of temperature is represented in figure 4.12. The temperature dependence of the junction resistance is similar to the same that was found in LSMO/BTO/LSMO magnetic tunnel junction (Figure 4.4), with a metal-insulator transition of the manganite [5] at 150 K. Because tunneling conductance only depends on the interface properties, this metal insulator transition is directly related with the interfacial LSMO bottom electrode Curie temperature. We have shown the bottom electrode resistance (in plane measurement) as a function of the temperature revealing a metallic behavior for the whole temperature range which means that T_C is higher than room temperature in good agreement with the magnetic characterization of LSMO thin films in chapter 3. On the other hand the tunneling transport in figure 4.12 reveals that the LSMO close to the BTO has a

Curie temperature strongly depressed which is a direct evidence of oxygen vacancies at such interface.

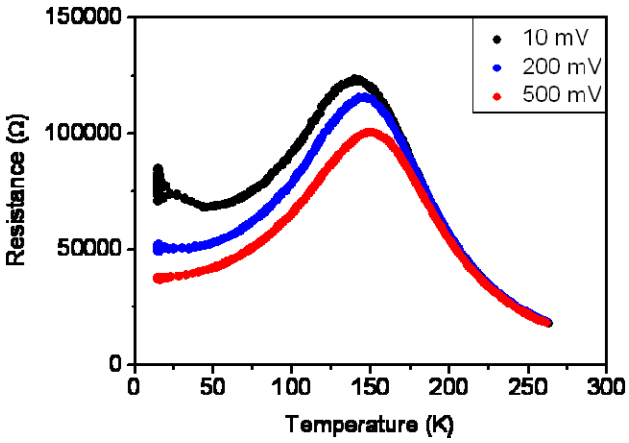

Figure 4.12. Resistance vs. temperature measured at 10 mV (black), 200 mV (blue), 500 mV (red) for a 5x10 μm^2 [LSMO 25nm / BTO 4.4 nm/ Ag] tunnel junction.

5 X-Ray Magnetic Circular Dichroism

Because oxygen vacancies add electrons to the Ti 3d conduction band, they could have an important influence in the magnetic properties at the LSMO/BTO interface. We have investigated interfacial magnetism using X-Ray magnetic circular dichroism (XMCD) technique. X-Ray absorption measurements with polarization analysis were performed at I10 beamline of the Diamond Light Source and at the 4-ID-C beamline of the Advanced Photon Source (Argonne National Laboratory). The XMCD measurements were carried out using a Total Electron Yield (TEY) detection method and X-Ray Magnetic Scattering (XRMS). To obtain the XMCD signal we have subtracted the absorption spectra obtained with positive and negative circularly polarized light with a 5 T magnetic field applied parallel to the X-ray beam direction and normal to the sample surface. X.ray Absorption Spectroscopy (XAS) is obtained as the average of the absorption spectra with right and left-polarized X-ray, with 5T magnetic field parallel to the propagation vector. Because TEY signal decreases exponentially with depth, and extracting electrons from an insulator at low temperatures (high resistivity) is more difficult. In order to increase the Ti TEY

dichroic signal, we have chosen a [LSMO 25nm/ BTO 1.2 nm] bilayer with ultra-thin (3 u.c.) BTO layer.

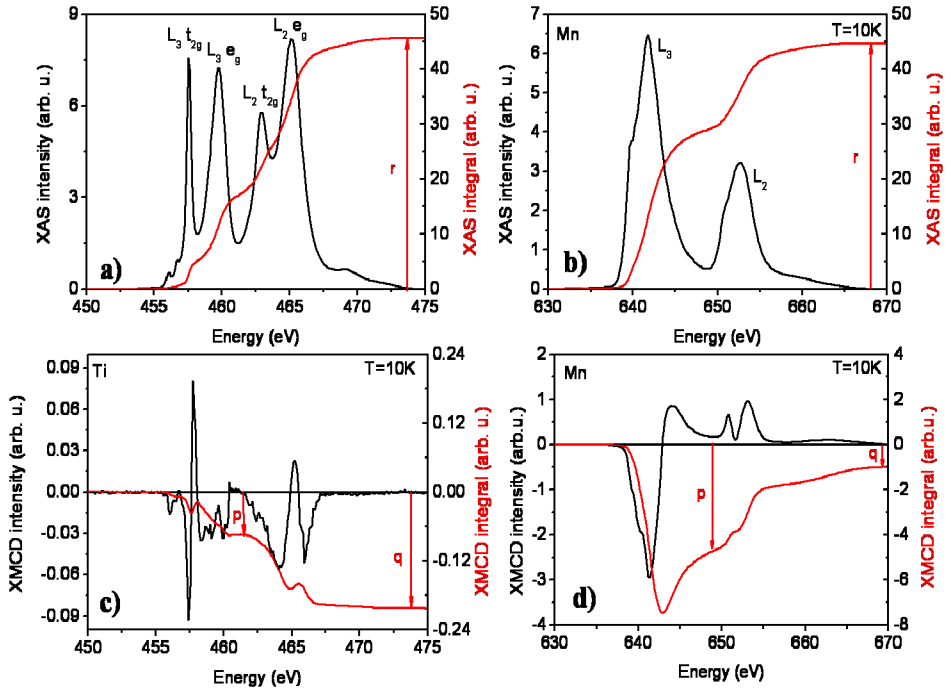

Figure 4.13. (a), (b) X-ray absorption (black) spectra of a [LMSO 25 nm/BTO 1.2 nm] bilayer corresponding to Mn and Ti, the integrated signal r (red) is indicated. (c), (d) X-ray magnetic circular dichroism Mn and Ti signal of a [LMSO 25 nm/BTO 1.2 nm] bilayer respectively. The integrated X-ray magnetic circular dichroism signal (q) is indicated as well as the L_3 edge integrated signal (p). All the spectra are measured at T = 10 K and with 5 T applied magnetic field.

Figure 4.13 (a) and (b) display XAS TEY energy scans (black line) and the integrated XAS intensity (red line) for Mn and Ti L_3 and L_2 absorption edges respectively. In Figure 4.13 (c) and (d) we show XMCD spectra (black line) and the integrated XMCD intensity (red line) for Mn and Ti respectively. It is clearly shown a weak dichroic signal in Ti (4.13 (c)) demonstrating magnetism in BTO layer. Although we know that the 2p spin-orbit splitting of the light transition metal ions is not large enough to obtain accurate spin moment (s_z) values from the sum rules, we use them anyway to obtain a rough estimate and to determine the spin moment orientation [41, 42]. We can obtain from Figure 4.12 the values

of integrals of the XAS spectra (r), the XMCD spectra (q), and the XMCD signal of the L_3 edge (p). Sum rules for spin and orbital moment are [43].

$$s_z = -\frac{(3p-2q)}{r} n_k \tag{4.1}$$

$$l_z = -\frac{2q}{3r} n_k \tag{4.2}$$

where n_h is the number of holes in d shells (9 and 6 for Ti and Mn respectively). The obtained values for the [LSMO 25 nm /BTO 1.2 nm] sample are s_z=1.6 μ_B/at_{Mn} and l_z=0.09μ_B/at_{Mn}. From the bulk magnetism measurements we know that the magnetic moment is 3.5μ_B/at_{Mn}, so sum rules are underestimating the spin magnetic moment. The orbital moment is near 0 if you compare it with $s_{z(Mn)}$, this in good agreement with the fact that the orbital moment is quenched in manganites. The XMCD signal of Ti is far weaker but we can still apply sum rules and obtain s_z=-0.04μ_B/at_{Ti}, here the negative value indicates that the orientation of the spin magnetic moment is contrary to the applied magnetic field and to the Mn magnetic moment. The orbital moment l_z=0.03μ_B/at_{Ti} is comparable and antiparallel to spins. Orbital magnetism is expected in orbitally degenerate system such as titanates, and was observed before in managanite titanates system [44].

Next we discuss the magnetic hysteresis loop obtained in reflectivity mode. In our experiment the energy of the X rays was set at 641.7 eV for the Mn L_3-edge and at 466.0 eV for the Ti L_3-edge with the beam oriented always parallel to the external field and making an angle of 10 degrees with the sample surface to ensure deep penetration of the x-ray beam. There are two main reasons for using reflectivity instead of TEY in this kind of experiment. The first is that sweeping a magnetic field has a strong influence on the secondary electrons which are free to move into the sample. These electrons would move on spirals with H-dependent radii, resulting in an odd shape of the TEY hysteresis loop, which makes the identification of the coercive fields almost impossible [45]. The second reason is the much stronger, free of noise, signal obtained from reflectivity. To get an adequate reflectivity signal from the Ti edge we summed over a large number of subsequent reflectivity loops.

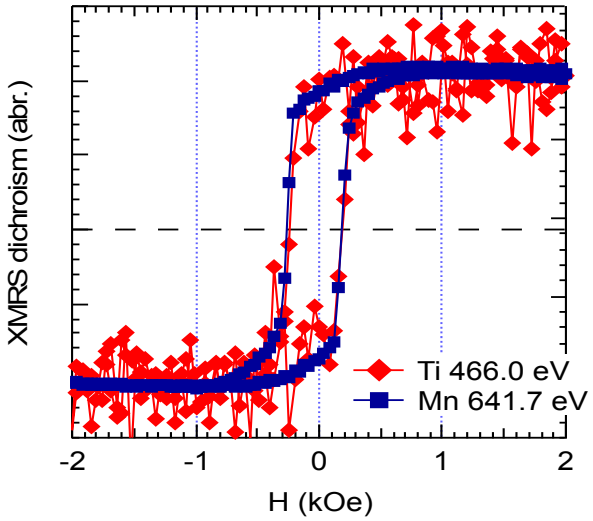

Figure 4.14. Normalized XMCD hysteresis loop taken at the Mn edge (blue) and at the Ti edge (red) for [LSMO 10nm / BTO 1.2 nm] sample. The field was applied along the [100] direction. Temperature was T=30K.

Normalized XRMS XMCD magnetic hysteresis loop measured at the energies which XMCD signal is maxima (Fig. 4.14). Note that only a qualitative analysis can be made on these kind of measurements since the absolute value of reflectivity does not provide a value for the magnetic moment upon varying the photon energy (around the same absorption edge), the applied field or the incidence angle of the beam. In contrast to the absorption (XAS) spectroscopy, the reflectivity signal is also sensitive to dispersive parameters. Nevertheless the relative change of the intensity along the same field sweep is associated to changes in the magnetization orientation giving a qualitative picture of the magnetization reversal process. The loops show that Ti dichroism signal follows the Mn's one during magnetization reversal, it implies that the Ti and Mn magnetic moments are coupled, i.e. they have the same coercive and saturation field.

6 Polarized Neutron Reflectometry

We have also investigated Polarized Neutron Reflectometry (PNR) to get the magnetic depth profile of LSMO/BTO/LSMO trilayers with the same MTJs

thicknesses. These measurements were performed at the polarized neutron reflectometer POLREF in ISIS at the Rutherfod Appleton Laboratory. All the measurements have been performed applying the field in the plane of the sample and along the [110] direction. The first PNR measurement was made at a saturating field of H= 7000 Oe (P state), and the second measurement was made at H=140 Oe (see the arrow in Figure 4.15 (top)) after saturation in H=-7000 Oe (AP state). Both measurements have been done at a temperature of 10K. Figure 4.15 (bottom) shows the R^{++} (neutron beam polarization parallel to the applied field before and after reflection) and R^{--} (neutron beam polarization antiparallel to the applied field before and after reflection), with the best fitting curves (straight line) in both P and AP states.

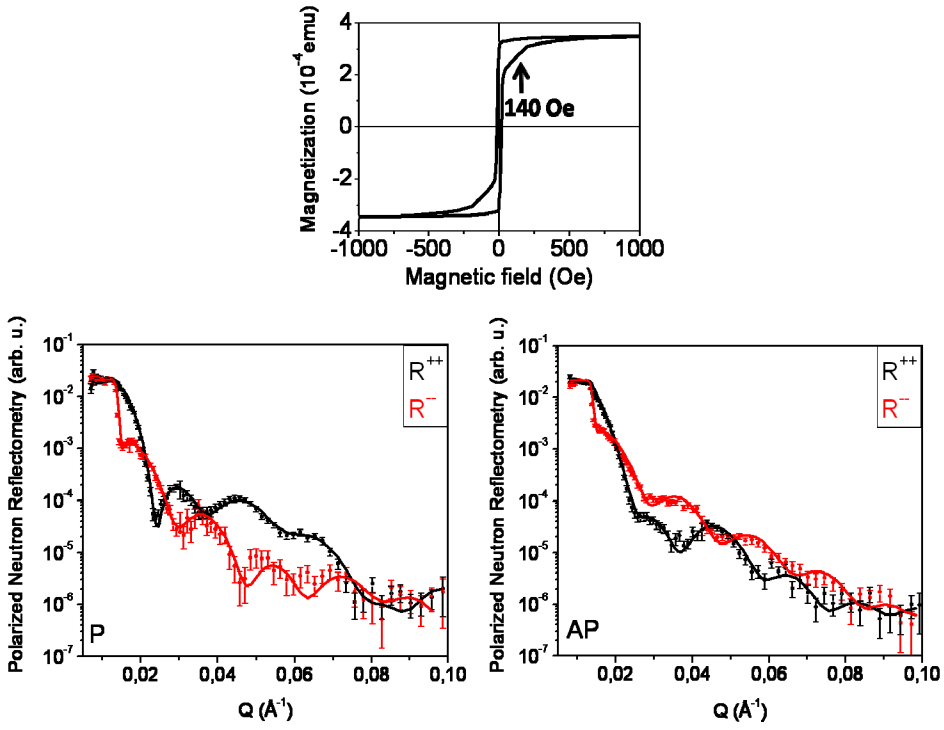

Figure 4.15. (top) Magnetic hysteresis loop of a [LSMO 24nm/BTO 4.4nm/LSMO 7nm] trilayer at 10 K. The arrow shows the magnetization at 140 Oe after saturate at -1000 Oe. (bottom left) PNR data taken at 10 K aplying H=7000 Oe (saturation) for a [LSMO 24nm/BTO 4.4nm/LSMO 7nm] trilayer. (bottom right) PNR data taken at 10 K applying a field of 140 Oe after saturate at -70000 Oe along the [110] axis. The fit to the data is represented by a line.

The best fitted parameters to the data are shown in Table 4.1 and in Table 4.2. The fitted parameters were neutron scattering length (b), the inverse of the volume of the unit cell (N), the thickness and the magnetization for each layer. Polly software is a very simple program for the simulation and analysis of polarized neutron reflectometry data, which provides constant parameter values (scattering length density, magnetization, nuclear scattering length,…) for each defined layer. However, it yields a rough picture of the magnetic depth profile which could reveal important information. For the P state we have defined four different layers (Table 4.1), one for each LSMO (bottom and top) and two for the BTO barrier. Top and bottom LSMO have different magnetization probably due to the different in-plane strain or because of the thin thickness of the top LSMO layer. This magnetization values are in good agreement with the VSM magnetometry of LSMO/BTO bilayers (see chapter 3). While the top part of the BTO layer hasn't induced magnetization, for the bottom part we have obtained -0.14μ_B/at$_{Ti}$. This magnetization at the bottom part of the BTO layer is antiferomagnetically coupled to the LSMO$_{BOTTOM}$,(3.49μ_B/at$_{Mn}$) and it is consistent with the existence of oxygen vacancies at the BTO/LSMO bottom interface and with the XMCD results. For the AP (Table 4.2) state we also have had to divide the LSMO$_{BOTTOM}$ in two layers. Although it has reduced the magnetic moment, the LSMO$_{TOP}$ layer is still antiparallel to the applied magnetic field and to the LSMO$_{BOTTOM}$ layer magnetization direction. It means that LSMO$_{BOTTOM}$ has lower coercive field and it reversals first that it is expected because the lower coercive field of the LSMO$_{BOTTOM}$ (see chapter 3). The reduced value of the magnetization of the LSMO$_{BOTTOM}$ closer to the BTO could be related with a magnetic coupling with LSMO$_{TOP}$ electrode, or with a non perfect alignment of the applied magnetic field with the [110] direction. Once again the BTO top part is not magnetic, and the bottom part has magnetic moment antiferromagnetically coupled with the LSMO$_{BOTTOM}$. The decreased of the N values for all the layers could be related with the lower magnetic signal that is produced for the sample in the AP state.

Layer	b (fm)	N (cm^{-3})	Thickness (nm)	Magnetization (μ_B/atm)
LSMO$_{TOP}$	21.55	1.63	6.7 nm	2.14
BTO	19.0	1.26	2.9 nm	0.00
BTO	19.0	1.32	2.3 nm	-0.15

$LSMO_{BOTTOM}$	21.55	1.49	23.0 nm	3.49
$STO_{SUBSTRATE}$	20.9	1.79	100.0 nm	0.00

Table 4.1. Fitted parameter from PNR data at 10 K applying 7000 Oe (saturation) for a [LSMO 24nm/BTO 4.4nm/LSMO 7nm] trilayer.

Layer	b (fm)	N (cm^{-3})	Thickness (nm)	Magnetization (μ_B/atm)
$LSMO_{TOP}$	21.55	1.63	6.9 nm	-1.78
BTO	19.0	1.26	2.5 nm	0.00
BTO	19.0	1.32	2.1 nm	-0.11
$LSMO_{BOTTOM}$	21.55	1.49	3.8 nm	2.25
$LSMO_{BOTTOM}$	21.55	1.67	19.3 nm	3.61
$STO_{SUBSTRATE}$	20.9	1.79	100.0 nm	0.00

Table 4.2. Fitted parameter from PNR data at 10 K applying 140 Oe after saturate at -7000 Oe for a [LSMO 24nm/BTO 4.4nm/LSMO 7nm] trilayer**.**

7 Magneto-electric coupling experiment

If the sample's easy axis is not perfectly align with the magnetic field anisotropic effects may occur. Fig 4.15 shows resistance of a different junction from a different LSMO/BTO/LSMO sample as a function of applied magnetic field at 20 K, at 10 mV, slightly disoriented from easy-axis. In this configuration the AP presents a slope which means that the two electrodes are not perfectly align, and at least one of them is rotating during the magnetic field sweep. There are two resistance jumps before achieve P state, the first one occurs at 350 Oe near the coercive field measure in the magnetic characterization of the sample (see chapter 3), the second one occurs at 600 Oe. We have calculated TMR from I(V) characteristic and from resistance vs. magnetic field sweeps (R(H)) and represent it vs. applied bias (Fig 4.16 (b)). TMR from R(H) (red symbols) is in good agreement with TMR from I(V) (black symbols). In this case the oscillatory dependence with bias is smaller without TMR suppression at very low bias. TMR values are smaller due to the non perfect AP alignment of the ferromagnetic electrodes.

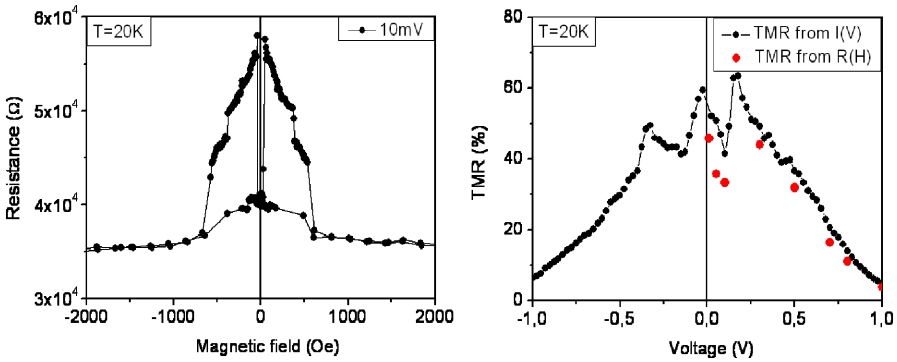

Figure 4.15. (left) Junction resistance versus applied magnetic field sweeping at 20 K measured at 10 mV. (right) Tunnel magnetoresistance (TMR) versus applied bias at 20K obtained from I-V curves (black curve) and from resistance versus magnetic field sweeps (red points).

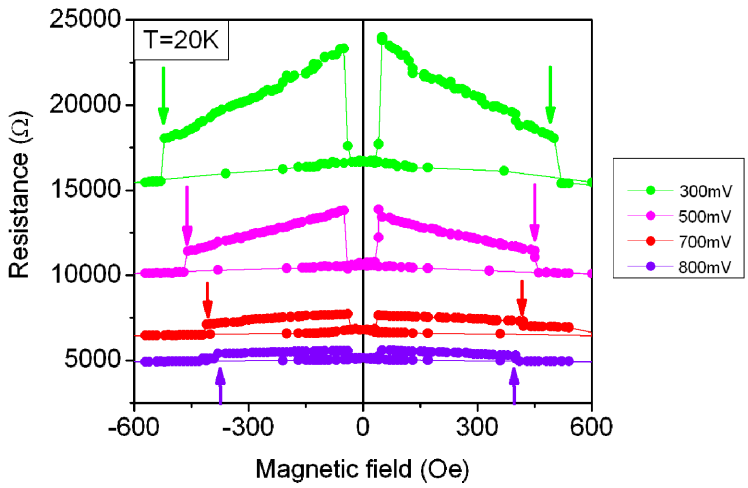

Figure 4.16. Junction resistance versus applied magnetic field sweeping at 20 K measured at different applied bias.

We have observed a decrease of the coercive field from top layer while increasing applied voltage in the resistance vs. magnetic field sweeps at different bias (see arrows in fig 4.16), evidencing an effect of the external applied electric field in the magnetic anisotropy of the ferromagnetic top LSMO electrode. We have studied these effects as a function of temperature for different applied bias.

In Figure 4.17 is shown that this effect is stronger at low temperatures (a) and it doesn't appear in the bottom layer (b). This magneto-electric effect allows us to control the magnetic state from AP state to P state using external electric fields. We have stabilized AP state sweeping magnetic field as we did in resistance vs. magnetic field measurements. Then we measured the resistance applying 10 mV several times verifying that this magnetic states is stable. When we apply a voltage of 1 V and measure again the resistance at 10 mV, this value has changed, and the new one corresponds to the value in the P state. This process is irreversible because we couldn't recover the AP state using electric fields. If we apply a voltage pulse of -1V, we don't achieve the AP state (fig 4.17). This results evidence the possibility of control magnetic anisotropy in magnetic tunnel junctions with ferroelectric barrier using electric fields. This magneto-electric effect doesn't occur only at the ferroelectric/ferromagnetic interface, because the whole LSMO layer (10 nm) changes its magnetization directions.

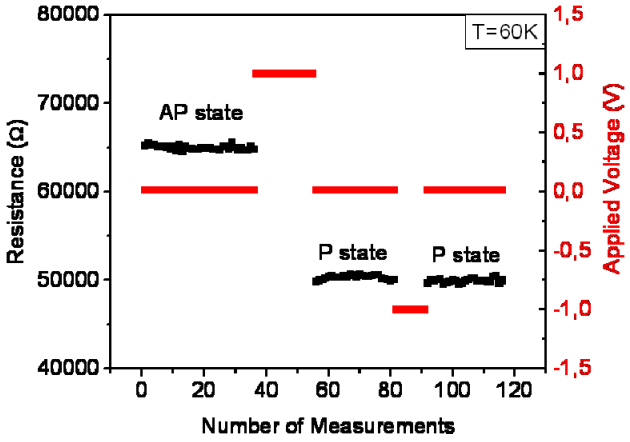

Figure 4.17. Junction resistance as a function of the number of measurements (black dots). The applied voltage during the measurement is 10 mV to read the resistance, and ±1 V to switch the magnetic state (red dots).

8 Summary

In this chapter we have studied spin dependent transport in magnetic tunnel junctions with ferroelectric barrier. We have obtained large TMR values

consistent with the half-metallicity of the LSMO electrodes. We have observed unusual oscillations in the tunnel conductance and in the TMR values as a function of applied voltages. We have also found a strong suppression of TMR amplitude at low bias. These results have been explained in terms of a Coulomb blockade charging effect due to magnetic metallic clusters embedded in the tunnel barrier. We have demonstrated the existence of oxygen vacancies at the LSMO/BTO bottom interface, which doped with electrons such interface, reducing the Ti oxidation state. We have verified that these Ti^{+3} reduced atoms have induced magnetic moment which is antiferomagnetically coupling to LSMO Mn atoms by XMCD and PNR measurements. This magnetic and electronic reconstruction could lead to a magneto-electric coupling. We have found an electric field control of the $LSMO_{TOP}$ electrode anisotropy. We are able to change the relative magnetizations alignment of the LSMO ferromagnetic electrodes from AP to P state applying voltage pulses. This process is irreversible because we could not recover the AP state using electric fields.

9 References

[1] M. Bibes, J. Villegas, and A. Barthelemy, *Adv. Phys.* **60**, 5 (2011).

[2] M. Imada, A. Fujimori, and Y. Tokura, *Rev. Mod. Phys*. **70**, 1039 (1998).

[3] E. Dagotto, and Y. Tokura, *MRS Bull*. **33**, 1037 (2009).

[4] M. Gajek, M. Bibes, A. Barthélémy, K. Bouzehouane, S. Fusil, M.Varela, J. Fontcuberta, and A. Fert, *Phys. Rev. B* **72** (2005).

[5] V. Garcia, M. Bibes, L. Bocher, S. Valencia, F. Kronast, A. Crassous, X. Moya, S. Enouz-Vedrenne, A. Gloter, D. Imhoff, C. Deranlot, N. D. Mathur, S. Fusil, K. Bouzehouane, and A. Barthélémy, *Science* **327**, 1106-1110 (2010).

[6] M. Gajek, M. Bibes, S. Fusil, K. Bouzehouane, J. Fontcuberta, A. Barthelemy, and A. Fert, *Nat. Mater*. **6**, 296 (2007).

[7] A. Ohtomo, and H.Y. Hwang, *Nature* **427**, 423 (2004).

[8] Y. Lu, X. Li, G. Gong, G. Xiao, A. Gupta, P. Lecoeur, J. Sun, Y. Wang, and V. Dravid, *Phys. Rev. B* **54**, R8357(1996).

[9] J. Z. Sun, W. J. Gallagher, P. R. Duncombe, L. Krusin-Elbaum, R. A. Altman, A. Gupta, Y. Lu, G. Q. Gong, and G. Xiao, *Appl. Phys. Lett*. **69**, 3266 (1996).

[10] M. Julliere, *Phys. Lett. A* **54**, 225 (1975).

[11] J. Z. Sun, L. Krusin-Elbaum, P. Duncombe, A. Gupta, and R. Laibowitz, *Appl. Phys. Lett.* **70**, 1769 (1997).

[12] M. Viret, M. Drouet, J. Nassar, J. P. Contour, C. Fermon, and A. Fert, *Europhys. Lett*. **39**, 545 (1997).

[13] M. Bowen, M. Bibes, A. Barthelemy, J.-P. Contour, A. Anane, Y. Lemaitre, and A. Fert, *Appl. Phys. Lett*. **82**, 233 (2003).

[14] T. Obata, T. Manako, Y. Shimakawa, and Y. Kubo, Appl. Phys. Lett. **74**, 290 (1999)

[15] J. O'Donnell, A. Andrus, S. Oh, E. Colla, and J. Eckstein, *Appl. Phys. Lett*. **76**, 1914 (2000).

[16] M. Jo, N. Mathur, N. Todd, and M. Blamire, *Phys. Rev. B* **61**, 14905 (2000).

[17] F. Y. Bruno, J. Garcia-Barriocanal, M. Varela, N. M. Nemes, P. Thakur, J. C. Cezar, N. B. Brookes, A. Rivera-Calzada, M. Garcia-Hernandez, C. Leon, S. Okamoto, S. J. Pennycook, and J. Santamaria, *Phys. Rev. Lett*. **106**, 147205 (2011).

[18] F. A. Cuellar, Y. H. Liu, J. Salafranca1, N. Nemes, E. Iborra, G. Sanchez-Santolino, M. Varela, M. Garcia-Hernandez, J. W. Freeland, M. Zhernenkov, M. R. Fitzsimmons, S. Okamoto, S. J. Pennycook, M. Bibes, A. Barthélémy, S. G. E. te Velthuis, Z. Sefrioui, C. Leon, J. Santamaria. Submitted.

[19] Yaohua Liu, F. A. Cuellar, Z. Sefrioui, J. W. Freeland, M. R. Fitzsimmons, C. Leon, J. Santamaria, and S. G. E. te Velthuis. *Phys. Rev. Lett*. **111**, 247203 (2013).

[20] A. Gruverman, D. Wu, M. Lu, Y. Wang, H.W. Jang, C. M. Folkman, M.Y. Zhuravlev, D. Felker, M. Rzchowski, C.-B. Eom, and E. Y. Tsymbal, *Nano Letters* **9**, 3539 (2009).

[21] W. F. Brinkman, R. C. Dynes, and J. M. Rowell, *J. Appl. Phys.* **41**, 1915 (1970)

[22] M. Y. Zhuravlev, R. F. Sabirianov, S. S. Jaswal, and E. Y. Tsymbal, *Phys. Rev. Lett.* **94**, 246802 (2005).

[23] Y. W. Yin, J. D. Burton, Y-M. Kim, A. Y. Borisevich, S. J. Pennycook, S. M. Yang, T. W. Noh, A. Gruverman, X. G. Li, E. Y. Tsymbal, and Qi Li. *Nature Mater*. **12**, 397 (2013).

[24] I. J. Vera Marún, F. M. Postma, J. C. Lodder, and R. Jansen, *Phys. Rev. B* **76**, 064426 (2007).

[25] E. T. Wertz, and Q. Li, *Appl. Phys. Lett.* **90**, 142506 (2007)]

[26] J. S. Noh, T. K. Nath, C. B. Eom, J. Z. Sun, W. Tian, and X. Q. Pan, *Appl. Phys. Lett* **79** 233 (2001).

[27] I. J. Veran Marun, F. M, Postma, J. C. Lodder, and R. Hansen, *Phys. Rev. B* **76**, 064426 (2007).

[28] J. Z. Sun, K. P. Roche, and S. S. P. Parkin *Phys. Rev. B* **61**, 11244 (2000)

[29] J. Bland, and B. Heinrich, *Ultrathin Magnetic Structures III: Fundamentals of Nanomagnetism* (Springer Verlag, 2005).

[30] J. Barnas, and A. Fert, *Phys. Rev. Lett.* **80**, 1058 (1998).

[31] H. Imamura, S. Takahashi, and S. Maekawa , *Phys. Rev. B* **59**, 6017 (1999).

[32] H. Grabert, and M. H. Devoret, *Single Charge tunneling* (Plenum Press,1992).

[33] J. Barnas, A. Fert, *J. Magn. Mag. Mater*. **192**, L-391 (1999).

[34] K. Yakushiji, S. Mitani, K. Takanashi, S. Takahashi, S. Maekawa, H. Imamura, and H. Fujimori, *Appl. Phys. Lett* **78**, 515 (2001).

[35] F. Ernult, K. Yamane, S. Mitani, K. Yakushiji, K. Takanashi Y. K. Takahashi, and K. Hono, *Appl. Phys. Lett* **84**, 3106 (2004)

[36] J. Garcia-Barriocanal, F. Y. Bruno, A. Rivera-Calzada, Z. Sefrioui, N. M. Nemes, M. Garcia-Hernandez, J. Rubio-Zuazo, G. R. Castro, M. Varela, S. J. Pennycook, C. Leon, and J. Santamaria, *Adv. Mat*. **22**, 627 (2010)

[37] S. D. Berger, and S. J. Pennycook, *Nature* **298**, 635 (1982)

[38] A. Ohtomo, D. A. Muller, J. L. Grazul, and H. Hwang, *Nature* **419,** 378 (2002).

[39] D. D. Cuong, B. Lee, K. M. Choi, H.-S. Ahn, S, and Han, J. Lee, *Phys. Rev. Lett.* **98**, 115503 (2007).

[40] D. A. Muller, N. Nakagawa, A. Ohtomo, J. L. Grazul, and H. Y. Hwang, *Nature* **430**, 657 (2004).

[41] C. Chen, Y. Idzerda, H. Lin, N. Smith, G. Meigs, E. Chaban, G. Ho, E. Pellegrin, and F. Sette, *Phys. Rev. Lett*. **75**, 152 (1995).

[42] C. Piamonteze, P. Miedema, and F. M. F. de Groot, *Phys. Rev. B* **80**, 184410 (2009).

[43] C. Chen, Y. Idzerda, H. Lin, N. Smith, G. Meigs, E. Chaban, G. Ho, E. Pellegrin, and F. Sette, *Phys. Rev. Lett*. **75**, 152 (1995).

[44] J. Garcia-Barriocanal, J. C. Cezar, F. Y. Bruno, P. Thakur, N. B. Brookes, C. Utfeld, A. Rivera-Calzada, S. R. Giblin, J. W. Taylor, J. A. Duffy, S. B. Dugdale, T. Nakamura, K. Kodama, C. Leon, S. Okamoto, and J. Santamaria, *Nature Comm*. **1**, 82, (2010).

[45] E. Goering A. Fuss, W. Weber, J. Will, and G. Schütz, *J. Appl. Phys*. **88**, 5922 (2000).

5

Effects of Ferroelectricity in $La_{0.7}Sr_{0.3}MnO_3$/ $BaTiO_3$ Tunnel Junctions

The recent discovery of ferroelectricity at the nanoscale opened up the implementation of ferroelectric material as a barrier in a tunnel junction devices, the so-called ferroelectric tunnel junction (FTJ). Films as thin as 4 nm of $Pb(Zr_{0.2}Ti_{0.8})O_3$ [1], 2 nm of $BiFeO_3$ [2, 3] or $(La,Bi)MnO_3$ [4], and ~1 nm of $PbTiO_3$ [5], P(VDF-TrFE) [6], and $BaTiO_3$ [7] have been reported to be ferroelectric. Functional properties of FTJs can be extended by replacing normal metal electrodes with a ferromagnetic material. This artificial multiferroic tunnel junctions (MFTJ) presents simultaneously tunnel magnetoresistance due to the modulation of the tunnel conductance produced by the relative alignment of the magnetizations directions of the ferromagnetic electrodes and tunnel electroresistance (TER) due to the modulation of the tunnel conductance produced by the ferroelectric polarization reversal [8, 9]. The interplay between ferroelectric and ferromagnetic properties in MFTJ may affect the electronic and magnetic properties of the interface leading to large magneto-electric effects which could reveal new physics to design novel functional devices.

1 Introduction

1.1 Ferroelectric Tunnel Junctions

A ferroelectric tunnel junction (FTJ) is composed of a few-unit-cell ferroelectric thin film sandwiched between two electrodes. The basic idea was originally formulated in 1971 by Esaki et al. [10]. Until recent years the conception of FTJ has not been achieved because the growth of ultrathin films of FE materials is challenging, and also because of the collective nature of ferroelectricity that is not always conserved at the nanometer scale required for operating in the tunneling regime. Moreover, it was believed that the critical thickness for ferroelectricity in thin films was much larger than the thickness necessary for tunneling to take place. Nevertheless, recent theoretical and experimental advances on perovskite ferroelectric oxide thin films demonstrate clearly that in some conditions ferroelectricity persists down to at least 1 nm [11, 7]. Tunneling through ferroelectrics is not only interesting from a fundamental point of view but it could also be of great potential for applications in the field of data storage, based on devices in which the information is encoded by the direction of the ferroelectric polarization, and read nondestructively. Applying an electric field across the ferroelectric film enables the reversal of the ferroelectric polarization, giving rise to two logic states with polarization pointing either up or down. Switching the ferroelectric polarization is predicted to give rise to large changes in the tunnel resistance, an effect called giant tunnel electroresistance (TER) [12].

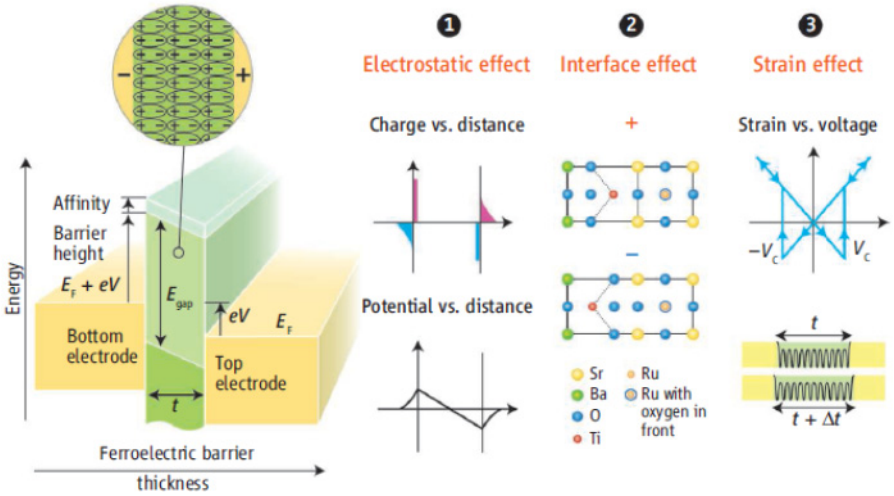

Figure 5.1. A ferroelectric tunnel junction. Schematic diagram of a tunnel junction, which consists of two electrodes separated by a nanometer-thick ferroelectric barrier layer (E_{gap} is the energy gap. E_F is the Fermi energy, V is the applied voltage, V_c is the coercive voltage, t is the barrier thickness, and Δt is the thickness variation under an applied field) from [13].

Three possible mechanisms describe the modulation of the tunnel conductance by the reversal of polarization in the ferroelectric barrier have been summarized by Tsymbal and Kohlstedt [13]. In Figure 5.1 is illustrated the effects of the ferroelectric polarization in the interface transmission function by changing (1) the electrostatic potential across the junction, (2) interface bonding strength, and/or (3) strain associated with the piezoelectric response. These mechanism are explained bellow:

1. When a ferroelectric film is sufficiently thin but still maintains its ferroelectric properties, the ferroelectric polarization surface charges are not completely screened by the adjacent metals and therefore the depolarizing electric field in the ferroelectric is not zero [14]. This depolarizing electric field depends on the direction of the electric polarization. If the metal electrodes have different screening lengths, this produced an asymmetry in the potential profile associated with the depolarizing electric field for the opposite polarization directions. This asymmetry in the potential profile for the two polarization directions leads to a change in the average height of the tunnel barrier modulating the tunnel conductance a few orders of magnitude [7]. An interesting

way to increase this effect, based on composite tunnel barriers combining a ferroelectric film with a nonpolar dielectric material, has recently been proposed [15], the dielectric layer serves as a switch that changes its barrier height from a low to a high value when the polarization of the ferroelectric is reversed.

2. The ferroelectric polarization reversal changes the direction of the ionic displacements in the ferroelectric barrier. This modifies the interfacial bonding and therefore the interfacial density of states of the electrodes which is related with the tunnel transmission probability [16, 17].

3. Because all ferroelectrics are piezoelectric, the distortions along the axis of the junction, caused by applied bias, change the barrier thickness. Since the tunnel current depends exponentially on the barrier width, a substantial modulation of the current can indeed be expected [18].

Experimentally, it is a challenge to demonstrate that the observed resistive switching is controlled by ferroelectricity. Indeed, bias-induced resistive switches have been observed in non-FE oxides [19]. A first breakthrough in FTJs was the demonstration of hysteretic I(V) curves in the $SrRuO_3$/ $BaTiO_3$(6 nm)/ $SrRuO_3$ [20] and $SrRuO_3$/ $PbZr_{0.2}Ti_{0.8}O_3$ (PZT) (6 nm)/ $SrRuO_3$ [21] Kohlstedt and co-workers showed that I(V) curves alone are not sufficient for the identification of the resistive switching mechanism, as they could be affected by the formation of local conductive channels across a ferroelectric film. Scanning probe microscopy (SPM) techniques combining piezoresponse force microscopy (PFM) and conducting atomic force microscopy (C-AFM) allows to correlate changes in the tunneling current with the ferroelectric polarization [22]. Using this method many groups have probed independently tunnel electro resistance (TER) in FTJ controlled by the ferroelectric polarization [7, 23- 27] reaching in many cases very large electroresistance values. Replacing one of the metal electrodes with a highly doped semiconductor in a FTJ Zheng Wen et al. have been achieved larger electroresistance ratio near 10^4 [28]. Controlling the ferroelectric domains dynamics Chanthbouala and co-workers have recently probe that the resistance in a FTJ can be continuously and reversibly modified, demonstrating that FTJ can be used as meristive devices [29] with applications in

multilevel nonvolatile memories ans adaptive networks that requires synapse-like functions [30]. Very large resistance changes and memristive effects have also been reported in system with the recently discovered polymorph of $BiFeO_3$ as a tunnel barrier [31].

1.2 Multiferroic Tunnel Junctions

A multiferroic tunnel junction (MFTJ) is a FTJ with ferromagnetic electrodes, o equivalently, a MTJ with a ferroelectric barrier. This artificial multiferroic device presents simultaneously TER and TMR effects making MFTJ a 4-resistance-state device where the resistance can be switched with both electric and magnetic fields [32]. In MFTJs, the spin-dependent and ferroelectricity-related contribution to the transport properties is, in first approximation, physically separated. However, at the ferroelectric/ferromagnetic interface can be produced an electronically driven magneto-electric effects leading to magnetic reconstructions at such interfaces which modify strongly the tunnel conductance.

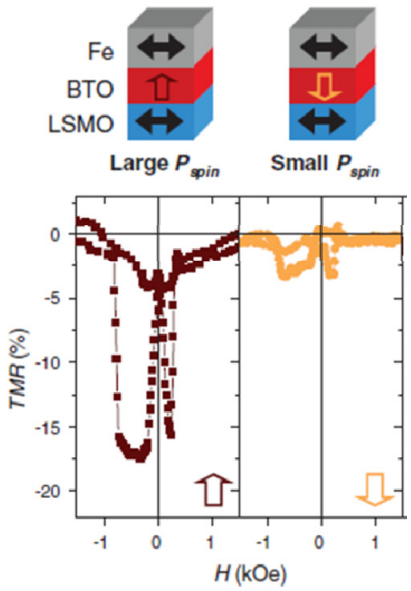

Figure 5.2. TMR as a function of magnetic field sweeps measured at –50 mV and at T = 4.2 K after poling the ferroelectric up (VP+) and down (VP–). From [33].

The first demonstration of ferroelectric control of the interfacial spin polarization was observed by V. Garcia and co-workers [33]. They fabricated LSMO/BTO/Fe MFTJ obtaining a significant change in the TMR amplitude with the ferroelectric polarization reversal (Figure 5.2). The observed change in TMR is consistent with the predicted change of the spin polarization at the Fe/$BaTiO_3$ interface [16] and the induced magnetic moment on the interface Ti atoms [34]. In LSMO/PZT/Co tunnel junctions it has been observed that TMR changes from positive to negative values depending on the direction of the ferroelectric polarization of the PZT due to a modification of the spin density of states at the PZT/Co interface [35]. Other MFTJ systems have been reported using $BiFeO_3$ [36] and $Ba_{0.95}Sr_{0.05}TiO_3$ tunnel barriers [37] The strong magneto-electric coupling effect at the ferroelectric/ferromagnetic interface in a FTJ could also produce magnetic phase transitions [38]. Yin et al. fabricated LSMO/BTO/ $La_{0.5}Ca_{0.5}MnO_3$ (LCMO)/LSMO MFTJ [39]. The ultra-thin (from 1 u.c. to 5 u.c.) LCMO layer can be tuned from the ferromagnetic metallic phase to the antiferromagnetic anisotropic insulate phase. This produces an enhancement of the TER driven by a modulation of the effective barrier thickness, and a large variation of the TMR.

5

2 Piezoresponse Force Microscopy (PFM)

Before study the effect of ferroelectric polarization reversal on the tunneling transport, we have to check that the ultrathin (4.4 nm) BTO sandwiched between LSMO electrodes is still ferroelectric after the patterning process. PFM trough the top electrode usually has higher signal, no electrostatic parasitic contributions, but it could have problems due to the strong sensitivity tip-electrode electrical contact. Adding a top electrode on an ultrathin ferroelectric layer the boundary conditions change strongly (screening charges, chemical bonding or interfaces reconstructions). It was predicted that the interface bonding at the ferroelectric-metal interfaces influences the ferroelectric state through the formation of intrinsic dipole moments at the interfaces, as determined by the chemical constituents and interfacial metal-oxide bonds [40]. For some interfaces, these dipole moments are switchable and may enhance the ferroelectric instability of the thin film [41]. For other interfaces, however the effect of interface bonding is detrimental and leads to the “freezing” of polar

displacements in the interfacial region, thus resulting in a ferroelectrically inactive layer near the interface [40]. In addition, ferroelectricity is a cooperative phenomena and it should be is easier to reversal the ferroelectric polarization in a small area like in the local mode or depositing a nano-size metal spot [27]. Nevertheless it's been reported ferroelectricity in oxide tunnel junction with around 100 μm^2 area [39].

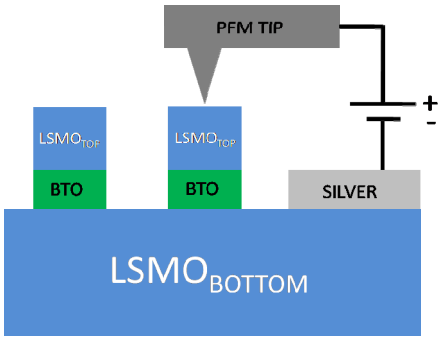

Figure 5.1.Schematic of the piezoresponse force microscope (PFM) measurement setup.

We have defined pillar with similar sizes that our MTJs using UV optical micro-lithography and Ar ion milling. The top LSMO electrode of the pillar is exposed, and we have evaporated silver electrode on the bottom LSMO electrode (Figure 5.1). We looked for the position of tunnel junctions with an optical microscope, and then we scanned the junction vicinity area using the largest field of view of the AFM. Finally we reduced the field of view in order to have good resolution of the pillars (Figure 5.2).

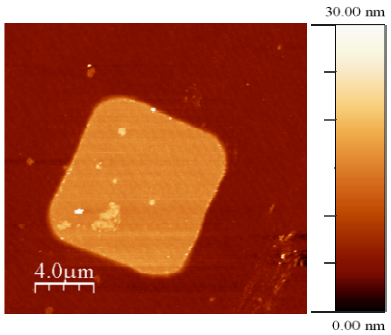

Figure 5.2. Atomic force microscopy topographic 25 µm x 25 µm image of a 10x10μm^2 [LSMO 24nm/ BTO 4.4 nm/ LSMO 8nm] tunnel junction.

We have measured several PFM hysteresis loops in different tunnel junctions at room temperature. We have checked the junction conductivity and topography before and after doing the PFM measurement to be sure that the tip wasn't damaged. Figure 5.3 (left) shows the PFM phase hysteresis loop of a $10x10\mu m^2$ [LSMO 24 nm/ BTO 4.4 nm/ LSMO 8 nm] tunnel junction. The measurement setup was similar to the one that we did in LSMO/BTO bilayers (see chapter 3). PFM phase presents a huge asymmetry in voltage, and it is large enough to produce only one ferroelectric polarization state stable (pointing downward). As we discussed in chapter 3 this asymmetry could be produced by different mechanism. Because we applied similar forces and the BTO layer is under a LSMO layer, this huge imprint due to a flexoelectric polarization produced by the mechanical stress in the BTO film is improbable. In chapter 3 (Figure 3.4) we have found that our LSMO/BTO/LSMO trilayers have symmetric $La_{0.7}Sr_{0.3}O/TiO_2$ interfaces. These polar interfaces serve as a doping layer donating electrons at the interface that compensates the ionic charge of the positively charged $(La_{0.7}Sr_{0.3}O)^+$ monolayer. This interface ionic charge creates an intrinsic electric field at the interface which can pin the polarization near the interface [42] but this effect shouldn't produce any preferential directions because it appears in both interfaces. The negative charge density generated by the oxygen vacancies at the bottom interface can pin the ferroelectric polarization assisting the ferroelectric downward direction. In the PFM hysteresis amplitude loop (Figure 5.3 (right)) we couldn't avoid the parasitic surface electrostatic component, due to the small ferroelectric signal, o because the large area that we are switching. These undesirable conditions don't allow us to obtain convincing results neither to conclude the ferroelectric analysis of our tunnel junctions using this technique.

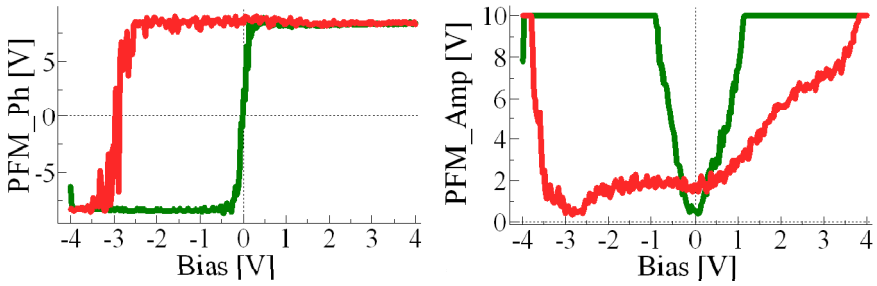

Figure 5.3. PFM phase (left) and amplitude (right) hysteresis loop for a 10x10μm^2 [LSMO 24nm/ BTO 4.4 nm/ LSMO 8nm] tunnel junction.

3 STEM Ionic displacement mapping

In ferroelectric ABO_3 perovskite structure, the ionic B-O displacement is directly related with the macroscopic polarization. We have used structural imaging aberration-corrected STEM to map the Ti-O in BTO and Mn-O LSMO ionic displacement. The positions of the different atoms are directly determined from the Annular Bright Field (ABF) images (Figure 5.4) using statistical method. We have defined dz as the relative distance between the B cation (positively charged) and the oxygen, therefore positive dz means ionic polarization pointing upward, and negative dz means ionic polarization pointing downward. In order to reduce statistical errors, we have done a 50 lateral unit cells average.

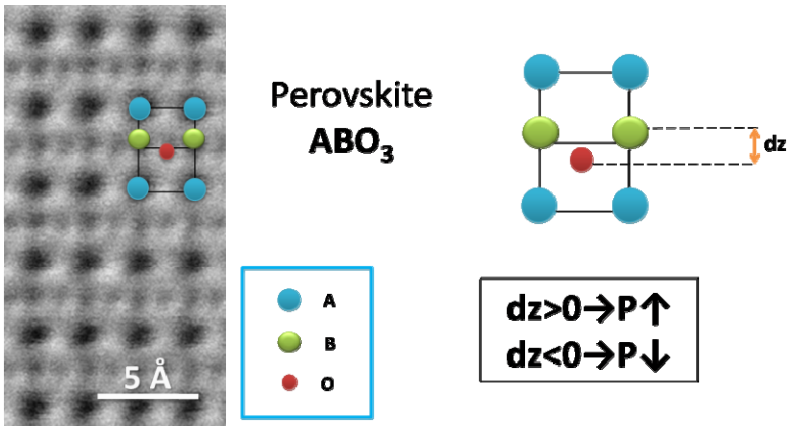

Figure 5.4. Annular bright field image of a ABO_3 perovskite structure. We have defined dz as the relative distance between the B cation and O (oxygen). dz > 0 means ionic polarization pointing upward and dz < 0 means ionic polarization pointing downward.

Figure 5.5 shows ionic displacements for LSMO and BTO near the two interfaces of a [LSMO 24nm/BTO 4.4 nm/ LSMO 8nm] trilayer. It's clearly shown that despite the fact that the polarization is not completely homogeneous, there is a spontaneous ferroelectric polarization in the absence of an external electric field which is pointing downward like the case of the LSMO/BTO bilayers (see chapter 3). This ferroelectric polarization should be switchable because if it is interfacially pinned by polar interfaces, both BTO ferroelectric polarization should point in the direction away from the interface generating a head-to-head domain wall inside the BTO layer (see figure 3.d. from Reference 42). The largest ferroelectric displacement obtained is -0.15 Å in good agreement with ferroelectric displacements reported in electron doped BTO grown on STO substrate [43, 44]. The ionic displacement profile inside the BTO layer shows a non homogeneous ferroelectric polarization showing a detrimental of the ferroelctricity probably due to the strong effect of the depolarizing field due to the BTO small thickness. The ferroelectric displacements are smaller near the LSMO/BTO bottom interface which could be related with a small reduction of the ferroelectricity due to the presence of oxygen vacancies. Figure 5.5 also shows a clear penetration of the ionic polarization into both LSMO electrodes over a distance of several unit cells in response to the BTO ferroelectric polarization. The BTO ferroelectric polarization and both LSMO ionic displacement are collinear and the interface is formed by a stable head-to-tail arrangement. Therefore the effect of the depolarizing field created by the

polarization charges at the interfaces is strongly reduced generating a very efficient mechanism of polarization screening.

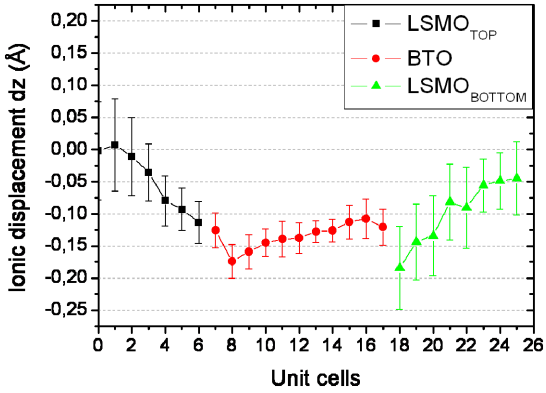

Figure 5.5. Ionic displacements near the LSMO/BTO interfaces of a [$LSMO_{BOTTOM}$ 24nm/ BTO 4.4 nm/ $LSMO_{TOP}$ 8nm] trilayer.

We have also measured in the same region of the sample the out of plane lattice parameter (c) through the two interfaces. In Figure 5.6 it is clearly shown a strain gradient in the BTO unit cells closer to the interfaces. In the bottom interface there are more unit cells involved in this deformation, and the strain gradient is slightly stronger, these results are in good agreement with the coexistence of oxygen vacancies which provide a larger deformability of the lattice structure. A strain gradient produces an electric field due to the flexoelectricity [45]. This electric field is proportional to the strain gradient and it could be strong enough to create a strong imprint in uniaxial, perfectly oriented ferroelectric thin films [46]. In BTO the flexoelectricity coefficient is negative [47], and according to the direct relation between the electric field produced by the flexoelectricity and the strain gradient, this electric field points to the LSMO in both interfaces. Furthermore it's possible that this electric field produced by the strain gradient could compensate the electric fields produced by polar interfaces avoiding the ferroelectric pinning effect at polar interfaces and stabilizing ferroelectricity in our BTO nano-layer.

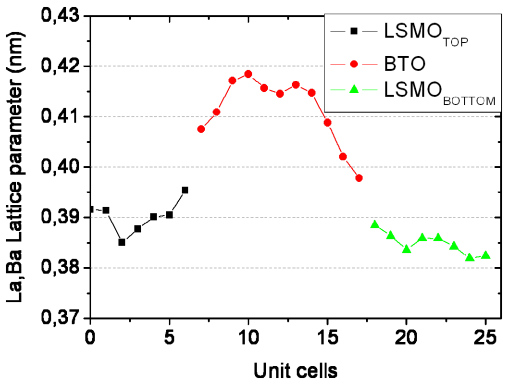

Figure 5.6. Out of plane lattice near the LSMO/BTO interfaces of a [$LSMO_{BOTTOM}$ 24nm/ BTO 4.4 nm/ $LSMO_{TOP}$ 8nm] trilayer.

4 Magnetotransport measurements

In order to investigate resistive switching due to the ferroelectric polarization reversal of the BTO barrier, we have measured current vs. voltage curves (Fig 5.7 left) in the magnetic P (blue) and AP (magenta) state, by cycling the bias voltage between -2 and +2 V at 14 K. Tunneling current is clearly reversible, and no effect due to a ferroelectric polarization switch is detected. Although Coulomb blockade oscillations intensity is weaker than other samples, there is still a clear "staircase" bias dependence in the calculated differential conductance (Fig. 5.7 right). The reduction of Coulomb blockade effect could be related with a reduction of the oxygen vacancies in this sample.

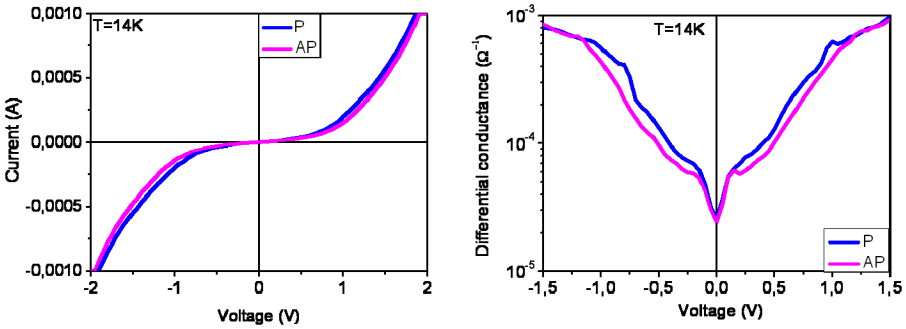

Figure 5.7. Tunnelling current as a function of applied bias at parallel (blue curve) and antiparallel (magenta curve) magnetic state at 14 K. (right) Differential conductance obtained as the numerical derivative of current vs. voltage at parallel (blue curve) and antiparallel (magenta curve) magnetic state at 14 K.

In Fig 5.8 is shown TMR calculated from I(V) curves as a function of applied bias at 14 K. TMR doesn't present oscillatory behavior because of the weak Coulomb blockade charging effect, but it still has a strong low bias suppression, therefore these two effects (charging Coulomb blockade effect and the low bias suppression) compete in the TMR bias dependence. The low bias suppression of the TMR observed is similar to the one observed in spin filtering devices [48]. Spin-filter tunneling occurs in devices with a FM electrode/FM barrier/normal metal. In these devices the exchange splitting of the conduction band creates two different tunnel barrier heights. Because the tunnel current density depends exponentially on the corresponding barrier heights, even with a modest difference in barrier heights, the tunnel probability for spin-up and spin-down electrons will be very different thus producing big MR effects. In our system, this anomalous voltage dependence behavior can be attributed to the competition between the positive spin polarization of the manganite contacts and the negative spin-filter effect from the interface-induced Ti magnetization detected by XMCD (see chapter 4) [49].

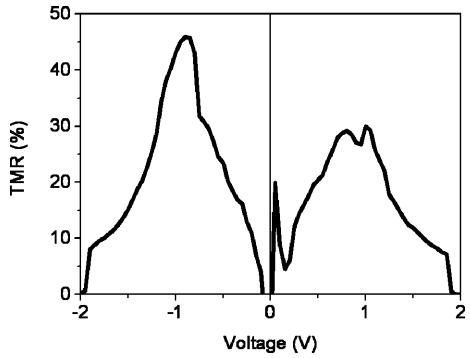

Figure 5.8. Tunnel magnetoresistance (TMR) versus applied bias at 14K obtained from I-V curves.

Below 40 K any evidence of resistive switching has been found. At this temperature, a noticeable hysteresis is observed cycling the bias voltage between -2 and +2 V in current vs. voltage curves for both parallel and antiparallel magnetizations alignment (Fig 5.9 (a) and (b)). In our experimental setup (Figure 5.10) if is applied a positive voltage higher than the switching voltage, it should produce that the ferroelectric polarization points upward ($P_{\uparrow}$), therefore if is applied a negative voltage higher than the negative switching voltage it produces a ferroelectric polarization reversal, stabilizing the ferroelectric down direction ($P_{\downarrow}$). The switching voltages are -1.25 V and 1.70 V as indicated by the convergence point of the current branches. The asymmetry in the switching voltages could be related with an internal built-in electric field probably generated by the oxygen vacancies. The huge difference between these switching voltages, and the ones measured with PFM could be due to a strong dependence of this coercive voltage values with temperature or a measurement artifact in the PFM measurements. In both cases (P and AP magnetic states) tunneling current is larger for a given voltage between switching voltages, when the voltage is swept from -2 V to +2 V (red curves), than the one from +2 V to -2 V (blue curves), achieving two bistable resistance states. For voltages larger than switching voltages, tunneling current is the same. Both current branches present nonlinearity, indicating that the electron tunneling dominates the transport process. In addition they exhibit no discontinuities and highly symmetry, in opposition with I-V curves from other resistive switching mechanism [50, 51]. Hysteretic I-V curves predicted for symmetric tunnel junctions are identified by the lack of the crossing of two ramifications and by the same conductance jumps

at the positive and negative switching voltages [18], however, our measurements are in good agreement with the expected behavior for asymmetric tunnel junction. In addition, when switching to a low resistance state occurs at one voltage polarity and switching back to a high-resistance state takes place at the opposite polarity, switching is called bipolar [19], which must have some asymmetry in the system structure (different electrodes, interfaces, voltage polarity asymmetry during the initial electroforming step).

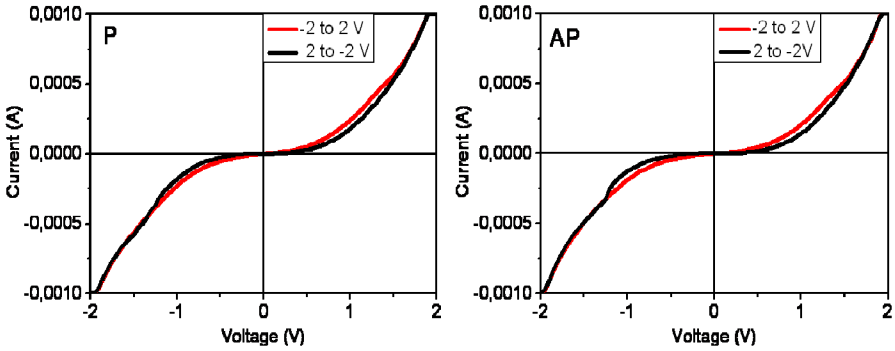

Figure 5.9. Tunnelling current as a function of applied bias hysteresis loops from -2 to 2 V (red curve) and from 2 to -2 V (black curve) at parallel P (left) and antiparallel AP (right) magnetic state at 40 K.

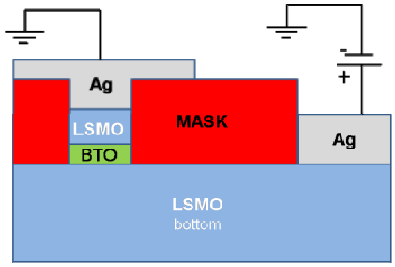

Figure 5.10. Schematic of the tunnel junction measurement setup. The LSMO top electrode is grounded.

We have obtained conductance as the numerical derivative of current vs. voltage in both $P_{\uparrow}$ (red curves) and $P_{\downarrow}$ (red curves) ferroelectric states for each magnetic states P (Fig 5.11 (c)), and AP (Figure 5.11 (d)). There is a strong change (more than 10 times) in differential conductance between the two

ferroelectric polarization states at low bias. Note that the conductance amplitude oscillations are much weaker than the case at 14 K, not only for the higher temperature (compare the amplitude difference between this two temperatures in Fig 4.6 (right) and Fig 4.9 (a)), but also for another mechanism that should be related with the ferroelectric polarization.

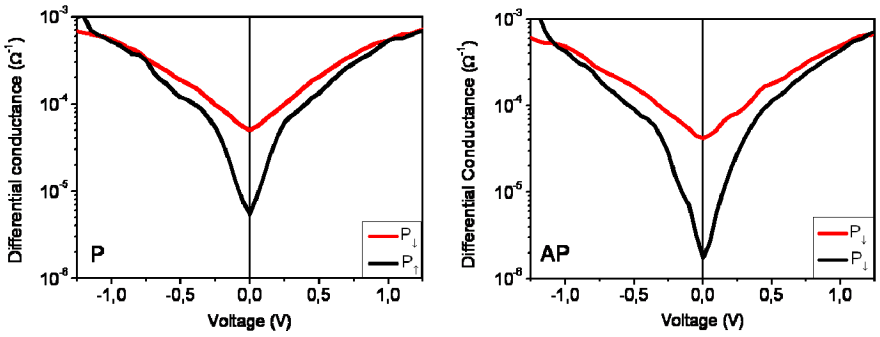

Figure 5.11. Differential conductance obtained as the numerical derivative of current vs. voltage for $P_{\downarrow}$ (red curve) and $P_{\uparrow}$ (black curve) at parallel P (left) and antiparallel AP (right) magnetic state at 40 K.

We have calculated tunnel electro-resistance (TER) that was defined as TER = $(I_{P\downarrow} - I_{P\uparrow}) / I_{P\uparrow}$ (Fig. 5.12) where $I_{P\uparrow}$ and $I_{P\downarrow}$ were respectively the tunnel current when the ferroelectric polarization is pointing up ($P_{\uparrow}$) and when the ferroelectric polarization is pointing down ($P_{\downarrow}$) in both P (blue) and AP (magenta) magnetic configurations. We have obtained positive TER values for the whole voltage range between coercive voltages. At low bias TER reach large values near 1000% for both magnetic states. Large or giant electroresistance has been predicted [12], and experimentally has been found [27, 39] only in ferroelectric tunnel junction with asymmetric electrodes. On the other hand small TER amplitudes (around 40%) have been reported in tunnel junctions fabricated with both LSMO electrode and BTO as a tunnel barrier [39]. In our system we have shown that we have symmetric LSMO/BTO/LSMO structure with identical $La_{0.7}Sr_{0.3}O/TiO_2$ interfaces, on the other hand, the oxygen vacancies localized at the bottom interface produce a chemical and electronic asymmetry. The low temperature range where we measured resistive switching could block ionic displacement such oxygen vacancies rejecting this mechanism. If these oxygen vacancies are "frozen" at the bottom interface during the ferroelectric

polarization reversal, it is possible to measure a huge variation of tunnel conductance with ferroelectric polarization reversal. Although our devices suggest ferroelectric polarization reversal as the resistive switching mechanism, electrochemical reaction at the interfaces due to the high applied voltages [52, 22, 53] cannot be excluded.

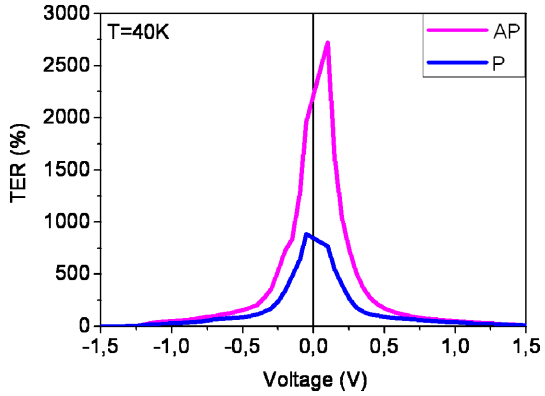

Figure 5.12. Tunnel electroresistance (TER) versus applied bias at 40K calculated from I-V curves for both magnetic states P (blue curve) and AP (magenta curve).

The variation of the TER amplitude with the relative alignment of the magnetization direction of the LSMO electrodes must be related with a modulation in the TMR amplitude due to the reversal of ferroelectric polarization. Ferroelectric control of the TMR has been predicted in different multiferroic tunnel junction systems [32, 8, 9], and recently experimentally observed [33, 36, 35] produced by the change in the spin–dependent density of states (DOS) of electrodes at the ferroelectric/ferromagnetic interface. Because LSMO is a half metal, interfacial modifications of the spin-dependent DOS are not expected, because there aren't states for the minority spins up to around 350 meV above the Fermi level E_F [54]. Another possible mechanism is to produce an interfacial magnetic transition in the La and Sr doped manganite [55]. Ferroelectric polarization for an ultrathin BTO layer constricted to the $SrTiO_3$ lattice parameter (3.905 Å) is 26 $\mu C \cdot cm^{-2}$ [42] which produces 0.25 e^-/u.c. at the BTO/LSMO interface. LSMO has a screening length of around 1 nm (3 u.c.) [56, 57], so the total doping level in the interfacial LSMO is 0.08 cm^{-3}. This doping

level is not enough to produce a magnetic transition in the $La_{0.7}Sr_{0.3}MnO_3$ (see Figure 3.1 in chapter 3). The large TER and the strong modulation of the TMR amplitude are clearly unexpected results in our LSMO/BTO/LSMO MTJs.

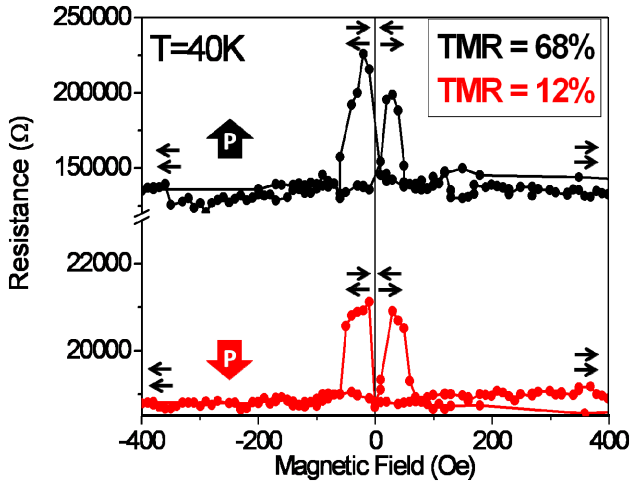

Figure 5.13. Junction resistance versus applied magnetic field sweeping measured at 40 K at 100 mV after applied a voltage pulse of 2 V (black curve) and –2V (red curve). Black arrows indicate magnetizations directions from top and bottom ferromagnetic electrodes, and the arrows with the letter "P" inside indicate the ferroelectric polarization direction $P_{\uparrow}$ (black) and $P_{\downarrow}$ (red).

An alternative method to check these results is to measure resistance vs. magnetic field sweeps after applied 100 ms voltage pulse $V_{PULSE} = \pm 2$ V (Fig 5.13). Taking account our measuring setup (Fig 5.10) after pole with positive 2 V must lead to a ferroelectric polarization pointing upward ($P_{\uparrow}$), and after pole with a negative -2 V must lead to a ferroelectric polarization pointing downward ($P_{\downarrow}$). Resistance measured at 100 mV at the saturating magnetic field presents high-resistance/low-resistance ratio of 10, when the ferroelectric polarization points toward $LSMO_{TOP}$ ($P_{\uparrow}$) or $LSMO_{BOTTOM}$ ($P_{\downarrow}$) in very good agreement with the TER calculated from I(V) curves. We have also found a strong TMR amplitude modulation. TMR is 4 times larger in $P_{\uparrow}$. The coexistence of TER and TMR effects in this tunnel junction make it a four-resistive device as was predicted by Zuralev *et al.* and Velev *et al.* [8, 9, 32]. These results reveal the possibility of use these tunnel junctions for the application in multilevel non volatile memories,

tunable electric and magnetic field sensors, and multifunctional resistive switches.

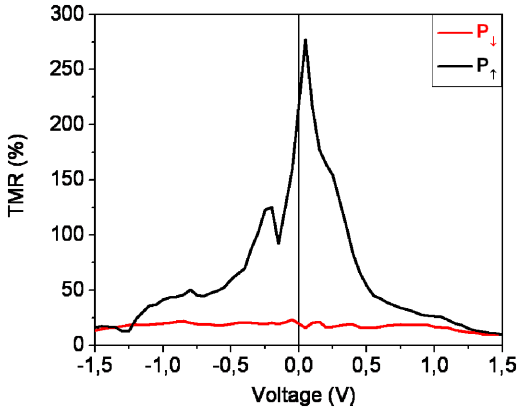

Figure 5.14. Tunnel magnetoresistance (TMR) versus applied bias at 14K obtained from I-V curves for both ferroelectric polarization states P↑ (black) and P↓ (red).

To have a better understanding of this TMR amplitude modulation we have calculated TMR as a function of voltage for the two ferroelectric polarization states ($P_{\uparrow}$ and $P_{\downarrow}$). Figure 5.14 shows completely different TMR bias dependence. For ferroelectric polarization pointing upward (black curve) the TMR low bias suppression has completely disappeared reaching very large TMR values near 300%. TMR decrease monotonically and strongly with increasing applied bias suggesting that inelastic scattering by magnon excitations at the LSMO/BTO interface controls the bias voltage [58, 59]. On the other hand, for ferroelectric polarization pointing downward (red curve) TMR presents a weak bias dependence and a non-monotonically decrease. We have compared the TMR bias dependence at 14 K at the virgin state (before pole), and 40 K and 100 K for polarization pointing downward (Figure 5.15). It is clearly observed that the three curves present similar behaviors with a TMR local maximum near 0.9 V. Therefore our LSMO/BTO/LSMO MTJs in the virgin state and with the ferroelectric polarization of the BTO pointing down are in the same ferroelectric

state. This result is expected due to the preferential downward ferroelectric polarization direction that we have previously observed.

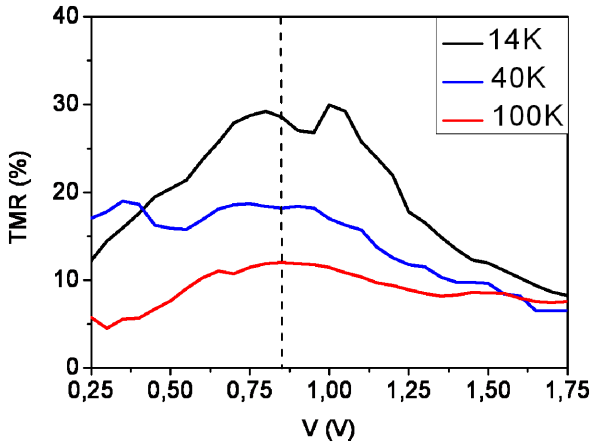

Figure 5.15. Tunnel magnetoresistance as a function of applied voltage at different temperatures. For T= 14K the junction is in virgin state, and for T= 40 K and 100K the ferroelectric polarization is poled down. The dashed line indicates the TMR local maximum near 0.9 V.

According with this last result and assuming that the junction that we have measured with no-TMR-low-bias suppression (see in chapter 4 Figure 4.10) is in $P_{\uparrow}$ state, we can plot TMR as a function of temperature for the two ferroelectric polarization directions. Figure 5.16 shows TMR measured at 100 mV as a function of temperature for $P_{\uparrow}$ (black points) and $P_{\downarrow}$ (red points) for different junctions (represented with different symbols), the solid lines (black and red) are guides to the eye. In $P_{\uparrow}$ state TMR measured at 100 mV decrease with increasing temperature. As temperature increases, the spin polarization of the ferromagnetic LSMO normally decreases [60] and the spin-flip scattering increases [61, 62], both mechanisms yield to an enhancement of the TMR at low temperature, as usually reported [63]. On the other hand, for $P_{\downarrow}$ state, the TMR decrease while lowering temperature. This anomalous behavior has been recently demonstrated that is related with spin filtering complex oxide magnetic tunnel junctions with an interfacial induced moment antiferromagnetically coupled to the Mn [49]. The observed interfacial Ti magnetization indicates that the spin-degeneracy in the BTO conduction band is lifted and the tunnel barrier becomes

spin-selective. While lowering the temperature, the induced magnetic moment becomes stronger and the exchange splitting in the BTO becomes larger enhancing its negative spin-filtering properties. The negative spin-filter effect produces a large suppression of the TMR at low bias which increases while decreasing temperature. At some temperatures we were not able to switch the polarization to $P_{\uparrow}$. This result reflects that the ferroelectric polarization direction pointing downward is more stable according that we observed in PFM and STEM measurements (Figure 5.3 and 5.5). The insets in this picture show TMR bias dependence for selected temperatures and ferroelectric polarization directions. It is clearly shown that when the ferroelectric polarization is pointing upward the TMR decreases monotonically while increasing the bias voltage, and when the ferroelectric polarization is pointing downward the TMR has a non monotonic bias dependence with a strong low bias suppression. Both TMR bias dependence converge at a temperature T=100 K, that it was the highest temperature that we observed TER. The absence of TER for temperatures above 100 K could be due to the migration of oxygen vacancies produced by the high electric fields combining with a high enough temperature which produces the oxygen vacancies thermal activation. When the oxygen vacancies can move the asymmetry in the system is broken and the ferroelectric control of the tunnel conductance vanishes. Another reason could be the pinning of the ferroelectric polarization in the oxygen vacancies defects after many poling cycles.

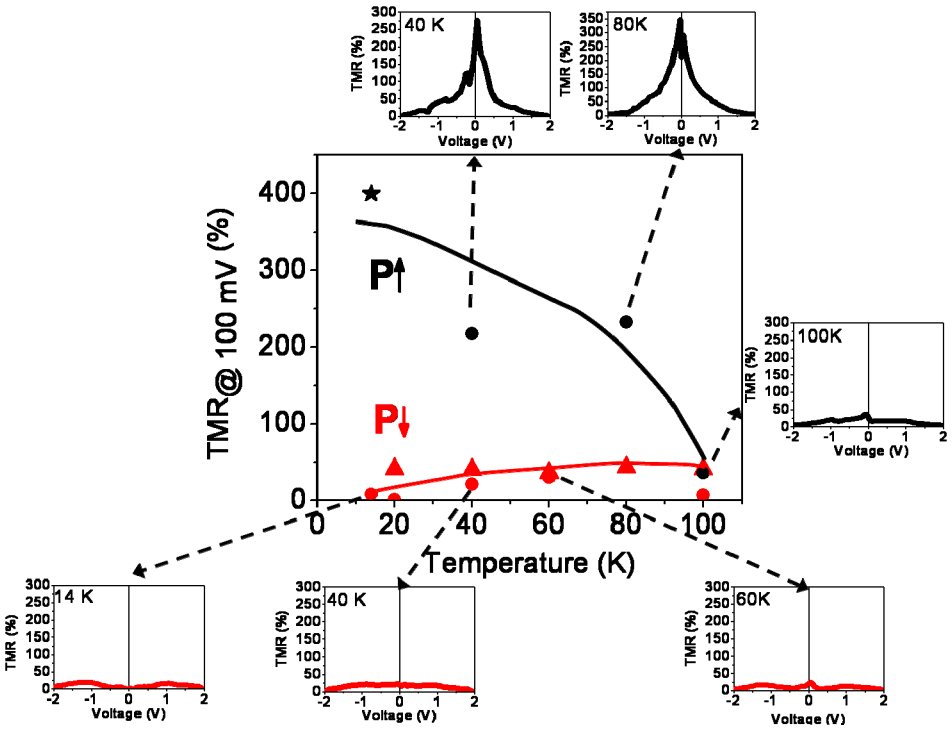

Figure 5.16. TMR measured at 100 mV as a function of temperature when the ferroelectric polarization in pointing upward (black curve) and when is pointing downward (red curve). The insets are TMR as a function of the applied bias for selected temperatures when the ferroelectric polarization in pointing upward (black curves) and when is pointing downward (red curves).

We have fitted the I(V) curves in the two ferroelectric polarization states for different temperature using the trapezoidal potential barrier tunneling model [24, 64]. Although this method is commonly used to analyze roughly the tunnel parameters, it could bring us a possible scenario which explains our results. We fitted the current curves considering measurements were the applied voltage was below 150 mV. The most noticeable result from these fits is that the barrier thickness for $P_{\uparrow}$ state is around 4.0 nm nearly the nominal 4.4 nm, but the barrier thickness for the $P_{\downarrow}$ state is strongly reduced to 2.4 nm. The obtained values of the barrier average height are between 0.2-0.3 eV for $P_{\uparrow}$ and is higher (between 0.5-0.6 eV) for $P_{\downarrow}$ state. The electron affinity of BTO is around 4.2 eV and the work function of LSMO is near 4.7 eV [65], so the barrier height should be around 0.4-0.5 eV in absence of ferroelectricity. It's known that the screening of

the polarization charges at the metal/ferroelectric interface changes the average height of the tunnel barrier [12]. In addition, the oxygen vacancies produce highly doped n-BTO at the bottom interface, and this electron density can be controlled with the ferroelectric polarization reversal [44]. We propose a possible scenario where the effective thickness of the tunnel barrier can be modified modulating the charge density produced by the oxygen vacancies at the LSMO/BTO bottom interface with the reversal of ferroelectric polarization.

We have represented this model considering the fitted parameters in Figure 5.17. When the ferroelectric polarization is pointing down (Figure 5.17 (top)) the positive polarization charges are self-screening by the electrons generated by the oxygen vacancies in such interface. This situation increases the average barrier height, and reduces the effective barrier thickness in good agreement with the fitted parameters. When the polarization is pointing upward (Figure 5.17 (bottom)) the positive charges at the top interface are screened by the accumulation of electron charge density at the LSMO interface, which reduces the average barrier height. The negative polarization charges at the bottom interface repulse the electrons generated by the oxygen vacancies. It produces charge depletion in the BTO layers recovering the nominal thickness of near 4.4 nm. This situation is clearly more unstable than the other ferroelectric polarization direction because the screening of the polarization charges at the bottom interface by the immobile ionized donors [66, 67] is less efficient than the self-screening when the polarization is pointing downward. Note that in both cases and for both interfaces the screenings of the polarization charges are more efficient due to the ionic displacements in the LSMO electrodes (Figure 5.5). The variation of the effective barrier thickness with the ferroelectric polarization reversal modifies dramatically the tunnel conductance because it depends exponentially on the barrier thickness leading to large TER values. Although the barrier average height increases while the barrier thickness decreases, in the Brickman model the tunnel conductance depends on the barrier thickness more strongly than on the barrier average height [64].

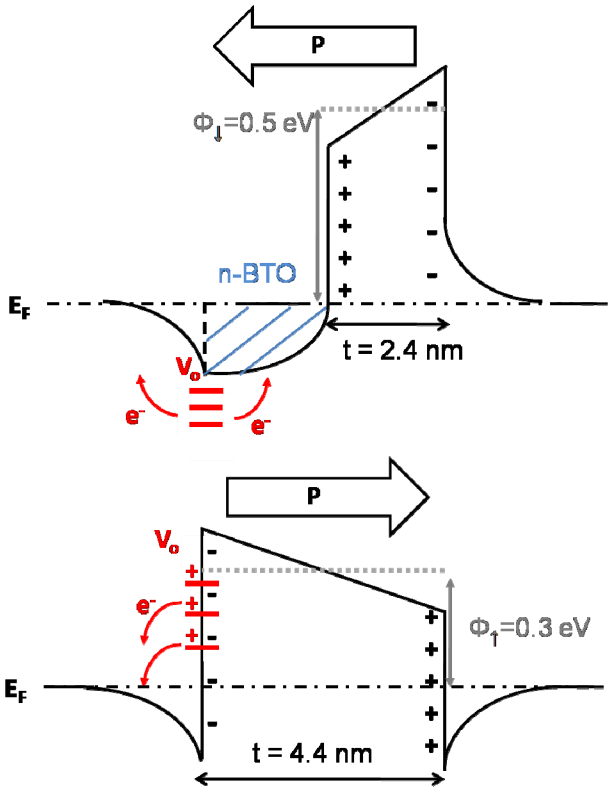

Figure 5.17. Barrier potential diagram of the LSMO/BTO/LSMO MTJ using the fitted parameters from the I(V) curves for both ferroelectric polarization pointing downward (top) and pointing downward (bottom). The defect levels of the oxygen vacancies (Vo) are represented in red, and the higly doped n-BTO region is represented in blue.

Another important consequence of this charge density modulation is the modulation of the TMR amplitude and the TMR bias dependence. We have observed in chapter 4 an induced magnetic moment in Ti that is directly related with the electrons generated by the oxygen vacancies which are localized in the Ti conduction band. The effect of this magnetic moment antiferromagnetically coupled to the Mn is reduce the effective spin polarization at the LSMO/BTO interface [49], which strongly reduces TMR values at low bias (Figure 5.8). The depletion of the charge density in the BTO when the ferroelectric polarization is pointing upward suppresses the induced magnetic moment. Therefore the negative spin-filtering effect is cancelled obtaining a normal TMR bias dependence with large TMR values at low bias (Figure 5.16). When the

ferroelectric polarization is pointing downward the induced magnetic moment is recovered and the TMR at low bias is strongly suppressed.

5 Transport measurements in LSMO/BTO/Ag tunnel junction

We have patterned 5x10 μm^2 [LSMO 25 nm)/BTO 4.9 nm/ Ag] using similar fabrication process of the LSMO/BTO/LSMO MTJs. The junctions are fabricated defining micros-size holes in the resist mask which was deposited on the top of a LSMO/BTO bilayer, and evaporating polycrystalline silver which fill these holes. The bottom electrode is made scratching the sample surface in one of the sample corners and evaporating silver on it. The schematic of the device is shown in Figure 5.18. Because Ag is a not magnetic metal, we have only measured the effect of the ferroelectric polarization reversal in the tunnel conductance. Figure 5.19 shows the current as a function of applied bias for both ferroelectric polarization directions. When the ferroelectric polarization direction is pointing down ($P_{\downarrow}$), the current shows a weak non linear bias dependence typically for tunneling transport. However when the ferroelectric polarization is pointing upward ($P_{\uparrow}$) the currents shows a strong non-linear bias dependence. This strong dependence is common in transport across metal/semiconductors Schottky barriers. This ferroelectric control of the conductance mechanism in this LSMO/BTO/Ag junctions leads to a giant electro resistance of near 300000% at 500 mV.

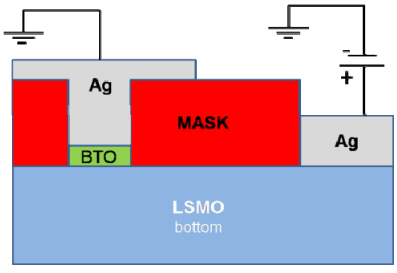

Figure 5.18. Schematic of the [LSMO 25 nm/BTO 4.4 nm/ Ag] tunnel junction measurement setup. The LSMO top electrode is grounded.

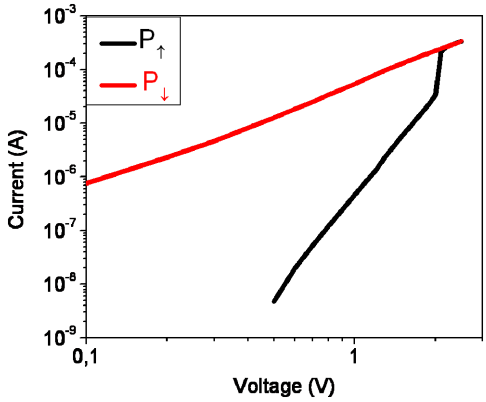

Figure 5.19. Current as a finction of the applied biasfor a 5x10μm^2 [LSMO 25nm/BTO 4.4nm/ Ag] tunnel junction for ferroelectric polarization pointing upward (black curve) and pointing downward (red curve) measured at 20 K.

Polarization control of transport mechanism has been predicted in electron doped BTO (0.06 electrons per BTO u.c.) with $SrRuO_3$ (SRO) electrodes obtaining a five order of magnitude in the conductance with the ferroelectric reversal [44]. When the ferroelectric polarization is pointing away the SRO/BTO interface is created a depletion layer generating a Schottky barrier at the interface of 1nm thick (figure 5.20 (a)). When the ferroelectric polarization is pointing to the interface, the accumulation of charge density at the interface generates an ohmic contact (figure 5.20 (b)). The work function of LSMO and Ag are 4.6 eV and 4.26 eV [68] respectively and the electron affinity of the BTO is around 4.2 eV. The Schottky barrier at the BTO/Ag interface is much smaller than the Schottky barrier at the LSMO/BTO interface. Therefore, a change in the transport mechanism should be produced at the LSMO/BTO interface. When the BTO ferroelectric polarization is pointing upward the depletion of the charge density (generated by the oxygen vacancies) produces a Schottky barrier at LSMO/BTO interface. If the ferroelectric polarization switches the accumulation of the charge density pushes the BTO conduction band bellow the Fermi level producing a LSMO/BTO ohmic contact which leads to a tunnel transport across the undoped BTO similar to the LSMO/BTO/LSMO tunnel junctions with the ferroelectric polarization pointing down.

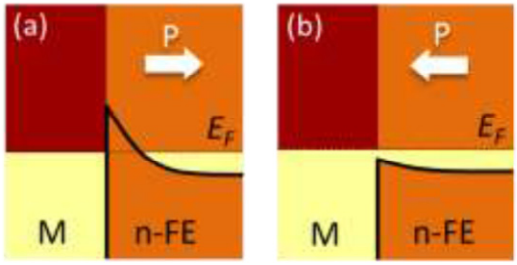

Figure 5.20. Polarization controlled band alignment at in the interface between a metal (M) and electron-doped ferroelectric (*n*-FE). Arrows indicate the polarization direction. (a) Polarization pointing away from the interface leads to electron depletion, pulling the *n*-FE conduction band upward. (b) Polarization pointing into the interface leads to electron accumulation, pushing the *n*-FE conduction band down. In the case shown here, polarization reversal leads to a transition from a Schottky tunnel barrier (a) to an Ohmic contact (b) between M and *n*-FE. [44].

We have analyzed the temperature dependence of the current for both polarization directions. When the polarization is pointing upward the current depends strongly on temperature in good agreement with the Schottky regime where the current depends exponentially on temperature. On the other hand, when the polarization is pointing downward the current practically doesn't depend on temperature in good agreement with tunneling regime. It's remarkable that the slope of the I(V) curve in $P_{\uparrow}$ state change for temperature above 120 K. This could be related with migration of oxygen vacancies above this temperature. Because LSMO/BTO/Ag is an asymmetric system we couldn't distinguish the effect of ferroelectric polarization reversal or a migration of the oxygen vacancies.

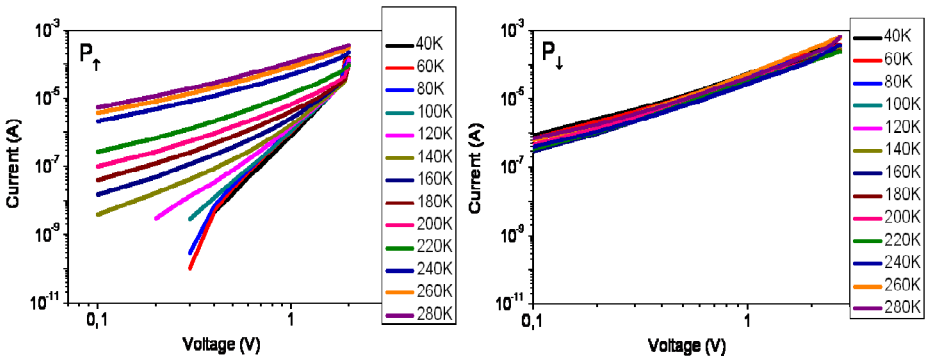

Figure 5.20 Current as a function of the applied biasfor a 5x10μm^2 [LSMO 25nm/BTO 4.4nm/ Ag] tunnel junction for ferroelectric polarization pointing upward (left) and pointing downward (right) measured from 20 K to 280 K.

6 Summary

We have investigated $La_{0.7}Sr_{0.3}MnO_3/BaTiO_3/La_{0.7}Sr_{0.3}MnO_3$ multiferroic tunnel junctions and, despite their symmetric structure, we have found very large tunnel electroresistance (TER) close to 1000% at low temperatures. This is interpreted in terms of a variation of the effective barrier thickness due to a large modulation of electron density charge at the BTO/LSMO bottom interface that is induced by the switching of ferroelectric polarization in BTO. Moreover, for the orientation of ferroelectric polarization that leads to the larger conductance value, the bias and temperature dependence of the tunnel magnetoresistance (TMR) is consistent with a depolarization (spin filtering) of the tunneling current. This behavior might be related to the presence of an induced Ti magnetic moment in BTO interface, antiparallel to that of Mn in LSMO, as detected by XMCD measurements. We have also investigated $La_{0.7}Sr_{0.3}MnO_3/BaTiO_3/Ag$ tunnel junction observing a giant electro resistance of near 100000% at 500 mV. We explain this electroresitance in terms of a change of the transport mechanism from Schottky to tunnel across the BTO layer. Our results reveal the possibility to tune spin dependent transport by an electric field through the reversal of the ferroelectric polarization of the barrier.

7 References

[1] T. Tybell, C. H. Ahn, and J.-M. Triscone, *Appl. Phys. Lett*. **75**, 856 (1999).

[2] H. Bea, S. Fusil, K. Bouzehouane, M. Bibes, M. Sirena, G. Herranz, E. Jacquet, J.-P. Contour and A. Barthelemy, *Jpn. J. Appl. Phys*. **45**, L187 (2006).

[3] Y. H. Chu, T. Zhao, M. P. Cruz, Q. Zhan, P. L. Yang, L. W. Martin, M. Huijben, C. H. Yang, F. Zavaliche, H. Zheng and R. Ramesh, *Appl. Phys. Lett*. **90**, 252906 (2007).

[4] M. Gajek, M. Bibes, S. Fusil, K. Bouzehouane, J. Fontcuberta, A. Barthelemy, and A. Fert, *Nat. Mater*. **6**, 296 (2007).

[5] D. D. Fong, G. B. Stephenson, S. K. Streiffer, J. A Eastman, O. Auciello, P. H. Fuoss, and C. Thompson, *Science* **304**, 1650 (2004).

[6] A. V. Bune, V. M. Fridkin, S. Ducharme, L. M. Blinov, S. P. Palto, A. V. Sorokin, S. G. Yudin, and A. Zlatkin, *Nature* **391**, 874 (1998).

[7] V. Garcia, S. Fusil, K. Bouzehouane, S. Enouz-Vedrenne, N. Mathur, A. Barthélémy, and M. Bibes, *Nature* **460**, 81 (2009).

[8] M. Y. Zhuravlev, S. S. Jaswal, E. Y. Tsymbal, and R.F. Sabirianov , *Appl. Phys. Lett.,* **87**, 222114 (2005).

[9] M. Y. Zhuravlev, S. Maekawa, and E.Y. Tsymbal, *Phys. Rev. B* **81**, 104419 (2010).

[10] L. Esaki, R. B. Laibowitz, and P. J. Stiles, *IBM Tech. Disclos. Bull*. **13**, 2161 (1971).

[11] J. Junquera, and P. Ghosez, *Nature* **422**, 506 (2003).

[12] M. Y. Zhuravlev, R. F. Sabirianov, S. S. Jaswal, and E. Y. Tsymbal, *Phys. Rev. Lett.* **94**, 246802 (2005).

[13] E. Y. Tsymbal, and H. Kohlstedt, *Science* **313**, 181 (2006).

[14] T. M. Shaw, S. Trolier-McKinstry, and P. C. McIntyre, *Annu. Rev. Mater. Sci.* **30**, 263 (2000).

[15] M. Y. Zhuravlev, Y. Wang, S. Maekawa, and E. Y. Tsymbal, *Appl. Phys. Lett.* **95**, 052902 (2009).

[16] C. G. Duan, S. S. Jaswal, and E. Y. Tsymbal, *Phys. Rev. Lett.* **97**, 047201 (2006).

[17] J. P. Velev, C.-G. Duan, K. D. Belaschenko, S. S. Jaswal, and E. Y. Tsymbal, Phys. Rev. Lett. **98**, 137201 (2007).

[18] H. Kohlstedt, N. A. Pertsev, J. Rodriguez-Contreras, and R. Waser, *Phys. Rev. B* **72**, 125341 (2005).

[19] R. Waser, and M. Aono, Nature Mater. **6**, 833 (2007).

[20] H. Kohlstedt, N. A. Pertsev, and R. Waser, *Mater. Res. Symp. Proc*. 688, C6.5.1 (2002).

[21] J. Rodriguez Contreras, H. Kohlstedt, U. Poppe, R. Waser, C. Buchal, and N. A. Pertsev, *Appl. Phys. Lett*. **83**, 4595 (2003).

[22] H. Kohlstedt, A. Petraru, K. Szot A. Rüdiger, P. Meuffels, H. Haselier, R. Waser, and V. Nagarajan, *Appl. Phys. Lett.* **92**, 062907 (2008).

[23] P. Maksymovych, S. Jesse, P. Yu, R. Ramesh, A. P. Baddorf, and S. V. Kalinin, *Science* **324**, 1421 (2009).

[24] A. Gruverman, D. Wu, H. Lu, Y. Wang, H. W. Jang, C. M Folkman, M Y. Zhuravlev, D. Felker, M Rzchowski, C.-B. Eom, E. Y. Tsymbal, *Nano Lett*. **9**, 3539 (2009).

[25] A. Crassous, V. Garcia, K. Bouzehouane, S. Fusil, A. H. G. Vlooswijk, G. Rispens, B. Noheda, M Bibes, and A. Barthelemy, *Appl. Phys. Lett.*, **96**, 042901 (2010).

[26] D. Pantel, S. Goetze, D. Hesse, and M. Alexe, *ACS Nano* **5**, 6032 (2011).

[27] A. Chanthbouala, A. Crassous, V. Garcia, K. Bouzehouane, S. Fusil, X. Moya, J. Allibe, B. Dlubak, J. Grollier, S. Xavier, C. Deranlot, A. Moshar, R.

Proksch, N. D. Mathur, M. Bibes, and A. Barthelemy, *Nature Nanotechnol* **7**, 101 (2012).

[28] Z. Wen, C. Li, D. Wu, A. Li, and N. Ming. *Nature Mater.* **12**, 617 (2013).

[29] A. Chanthbouala, V. Garcia, R. Cherifi, K. Bouzehouane, S. Fusil, X. Moya, S. Xavier, H. Yamada, C. Deranlot, N. D. Mathur, M. Bibes, A. Barthélémy, and J. Grollier. *Nature Mater.* **11**. 860 (2012).

[30] S. D. Ha, and S. Ramanathan, *J. Appl. Phys.* **110,** 071101 (2011).

[31] H. Yamada, V. Garcia, S. Fusil, S. Boyn, M. Marinova, A. Gloter, S. Xavier, J. Grollier, E. Jacquet, C. Carretero, C. Deranlot, M. Bibes, and A. Barthelemy. *ACS Nano* **7**, 5385 (2013).

[32] J. Velev, C.-G. Duan, J. D. Burton, A Smogunov, M. K. Niranjan, E. Tosatti, S. S. Jaswal, and E. Y. Tsymbal, *Nano Letters* **9**, 427 (2009).

[33] V. Garcia, M. Bibes, L. Bocher, S. Valencia, F. Kronast, A. Crassous, X. Moya, S. Enouz-Vedrenne, A. Gloter, D. Imhoff, C. Deranlot, N. D. Mathur, S. Fusil, K. Bouzehouane, and A. Barthélémy, *Science* **327**, 1106-1110 (2010).

[34] S. Valencia, A. Crassous, L. Bocher, V. Garcia, X. Moya, R. O. Cherifi, C. Deranlot, K. Bouzehouane, S. Fusil, A. Zobelli, A. Gloter, N. D. Mathur, A. Gaupp, R. Abrudan, F. Radu, A. Barthélémy, and M. Bibes, *Nature Mater*. **10**, 753 (2011).

[35] D. Pantel, S. Goetze, D. Hesse, and M. Alexe, *Nature Mater.* **11**, 289 (2012).

[36] M. Hambe, A. Petraru, N. A. Pertsev, P. Munroe, V. Nagarajan, and H. Kohlstedt Adv. Funct. Mater. 2010, 20, 2436–2441]

[37] Y. W. Yin, M. Raju, W. J. Hu, X. J. Weng, and X. G. Li, *J. Appl. Phys*. **109**, 07D915 (2011).

[38] J. D. Burton, and E.Y. Tsymbal, *Phys. Rev. Lett* **106**, 157203 (2011).

[39] Y. W. Yin, J. D. Burton, Y-M. Kim, A. Y. Borisevich, S. J. Pennycook, S. M. Yang, T.W. Noh, A. Gruverman, X. G. Li, E. Y. Tsymbal, and Qi Li. *Nature Mater*. **12**, 397 (2013).

[40] C.-G. Duan, R. F. Sabiryanov, W. N. Mei, S. S. Jaswal, and E. Y. Tsymbal, *Nano Lett*. **6**, 483 (2006).

[41] M. Stengel, D. Vanderbilt, and N. A. Spaldin, *Nature Mater*. **8**, 392 (2009).

[42] X. Liu, Y. Wang, P. V. Lukashev, J. D. Burton, and E. Y. Tsymbal, *Phys Rev. B* **85**, 125407 (2012).)

[43] Y. Wang, M. K. Niranjan, K. Janicka, J. P. Velev, M. Ye. Zhuravlev, S. S. Jaswal, and E. Y. Tsymbal, *Phys. Rev. B* **82**, 094114 (2010).

[44] X. Liu, Y. Wang, J. D. Burton, and E. Y. Tsymbal, *ArXiv* 1306.5763 [cond-mat.mtrl-sci] (2013).

[45] P. Zubko, G. Catalan , A. Buckley ,P. R. L. Welche, and J. F. Scott. *Phys. Rev. Lett.* **99**, 167601 (2007).

[46] D. Lee, A. Yoon, S.Y. Jang, J.-G. Yoon, J.-S. Chung, M. Kim, J. F. Scott, and T.W. Noh1, *Phys. Rev. Lett*. **107**, 057602 (2011).

[47] J. Hong, G. Catalan, J. F. Scott, and E. Artacho, *J. Phys. Condens. Matter* **22**, 112201 (2010).

[48] J. Moodera, T. Santos, and T. Nagahama, *J. Phys.: Condens. Matter* **19**, 165202 (2007).

[49] Yaohua Liu, F. A. Cuellar, Z. Sefrioui, J. W. Freeland, M. R. Fitzsimmons, C. Leon, J. Santamaria, and S. G. E. te Velthuis. *Phys. Rev. Lett*. **111**, 247203 (2013).

[50] K. Szot, W. Speier, G. Bihlmayer, and R. Waser. *Nature Mater.* **5**, 312 (2006).

[51] R. Oligschlaeger, R. Waser, R. Meyer, S. Karthauser, and R. Dittmann, *App. Phys. Lett.* **88**, 042901, (2006).

[52] J. Z. Sun, K. P. Roche, and S. S. P. Parkin *Phys. Rev. B* **61**, 11244 (2000).

[53] J. Choi, J. S. Kim, I. Hwang, S. Hong, I. S. Byun, S. W. Lee,S. O. Kang, and B. H. Park, *Appl. Phys. Lett*. **96**, 262113 (2010).

[54] M. Bowen, A. Barthelemy, M. Bibes, E. Jaquet, J.-P. Contour, A. Fert, F. Ciccacci, L. Duo, and R. Bertacco, *Phys. Rev. Lett* **95**, 137203 (2005).

[55] J. D. Burton, and E. Y. Tsymbal, *Phys. Rev. B* **80**, 174406 (2009).

[56] M. Dzero, L. P. Gorkov, and Z. Kresin, *Int. J. Mod. Phys. B* **10**, 2095 (2003).

[57] X. Hong, A. Posadas, and C. H. Ahn, *Appl. Phys. Lett*. **86**, 142501 (2005).

[58] S. Zhang , P. M. Levy, A. Marley, and S. S. P. Parkin, *Phys. Rev. Lett.* **79** 3744 (1997).

[59] J. S. Moodera, J. Nowak, and R. J. M. van de Veerdonk, *Phys. Rev. Lett*. **80** 2941 (1998).

[60] V. Garcia, M. Bibes, A. Barthélémy, M. Bowen, E. Jacquet, J. P. Contour, and A. Fert, *Phys. Rev. B* **69**, 052403 (2004).

[61] M. Julliere, Physics Letters A **54**, 225 (1975)

[62] A. Vedyayev, D. Bagrets, A. Bagrets, and B. Dieny, Phys. Rev. B **63**, 064429 (2001).]

[63] M. Bowen, M. Bibes, A. Barthelemy, J.-P. Contour, A. Anane, Y. Lemaitre, and A. Fert, *Appl. Phys. Lett*. **82**, 233 (2003).

[64] W. F. Brinkman, R. C. Dynes, and J. M. Rowell, *J. Appl. Phys.* **41**, 1915 (1970).

[65] M. P. de Jong, V. A. Dediu, C. Taliani, and W. R. Salaneck, *J. Appl. Phys*. **94**, 7292 (2003).

[66] S. Mathews, R. Ramesh, T. Venkatesan, and J. Benedetto, *Science* **276**, 238 (1997).

[67] S. L. Miller, and P. J. McWhorter, *J. Appl. Phys*. **72**, 5999 (1992).

[68] H. B. Michaelson, *J. Appl. Phys*. **48**, 4729 (1977).

6 Conclusions

The main finding of this thesis are summarized here. We have investigated artificial multiferroic heterostructures based on transition metal oxide emphasizing in the interfacial properties. We have used tunnel junction architecture due to the huge sensitivity of the tunnel conductance to the interface properties. We have explored the interplay between ferromagnetism and ferroelectricity, the electronic and magnetic interfacial reconstruction, and the influence of the oxygen vacancies in these artificial multiferroic heterostructures.

We used ferromagnetic manganite $La_{0.7}Sr_{0.3}MnO_3$ as electrodes and ferroelectric $BaTiO_3$ as tunnel barrier. We demonstrate that our heterostructures are ferromagnetic and ferroelectric at the nanoscale. In adittion we probe ferroelectricity in ultrathin BTO layers down 4.4 nm, making it possible to implement BTO ultrathin films as active tunnel barrier. We have fabricated micron size tunnel junctions using standard optical lithography and Ar ion milling techniques. The transport across the BTO ultrathin layer (4.4 nm) presents tunneling properties probing that our LSMO/BTO/LSMO devices are in the tunneling regime. The magnetotransport measurement reveals an abrupt jump of the junction resistance when the relative alignment of the magnetization direction turns from parallel (P) to antiparallel (AP). The high resistance state corresponds to the AP configuration and the low resistance state corresponds to

the P configurations. These two stable resistance states are in good agreement with the positive spin polarization of the both LSMO electrodes. We have measured large tunnel magneto resistance (TMR) according with the half-metallic character of the ferromagnetic electrodes. TMR measured at low bias presents a non monotonic voltage bias dependence with a strong TMR low bias suppression similar to the TMR found in spin-filter systems indicating a possible magnetism in the tunnel barrier. This effect is stronger at low temperatures.

The LSMO/BTO/LSMO multiferroic tunnel junctions devices present four different stable resistance states due to the simultaneous presence of the TMR produced by the relative alignment of the directions of the magnetizations of the ferromagnetic LSMO electrodes and the tunnel electroresistance (TER) produced by the ferroelectric polarization reversal. It's remarkable the large TER found near 1000% at low bias which reveals an interfacial asymmetry in the LSMO/BTO/LSMO tunnel junction. We found that the ultrathin BTO barrier has a preferential ferroelectric polarization direction indicating the possible presence of oxygen vacancies at the LSMO/BTO bottom interface. The in-plane transport measurement of the LSMO bottom electrode reveals a Curie temperature larger than room temperature that is in good agreement with the magnetometry characterization, on the other hand, in the tunneling transport of a LSMO/BTO bilayer tunnel junctions appears a metal-insulator transition near 150K revealing a strong depression of the interfacial manganite bottom electrode Curie temperature which is a direct evidence of the existence of oxygen vacancies in such interface. Using aberration corrected STEM-EELS technique we found a reduction of the Ti oxidation at the LSMO/BTO bottom interface according with the presence of oxygen vacancies, because these defects has a doping effect by the associated electron charge density. We explain these large TER values in term of the modulation of this electron charge density generated by the oxygen vacancies at the LSMO/BTO bottom interface. The ferroelectric polarization of the BTO produces charge density depletion (accumulation) when it is pointing upward (downward). This charge density modulation inside the BTO layer produces a change in the effective tunnel barrier thickness. Because the tunneling conductance depends exponentially on the barrier thickness, this effect produces a strong variation of the tunneling current with the ferroelectric polarization reversal.

We also observed in the LSMO/BTO/LSMO tunnel junctions a modulation of the TMR values with the ferroelectric polarization reversal. The half-metallic character of the LSMO ferromagnetic electrode doesn't allow the variation of the interfacial spin polarization with the ferroelectric polarization reversal. Furthermore, a magnetic transition of the optimal dope LSMO is also rejected because the polarization charges don't create a strong enough field effect which could dope the LSMO electrodes I order to produce a magnetic phase transition (from ferromagnetic metal to antiferromagnetic insulator). In order to look for the origin of this TMR amplitude modulation we have analyzed the interfacial magnetic properties of the LSMO electrodes. We found an interfacial induced magnetic moment at the Ti edge in LSMO/BTO bilayers detected with X-ray magnetic circular dichroism. We probed that this Ti induced magnetic moment follows Mn magnetic moment and they are antiferromagnetically coupled. The interfacial magnetism produces a negative spin-filtering because it depolarized the spin tunneling current according with the TMR low bias suppression. Because the interfacial Ti magnetism is directly related with the electron charge density in such interface it should be modified by the ferroelectric polarization reversal. When this electron charge density is depleted (ferroelectric polarization pointing upward) the Ti induced magnetic moment disappears cancelling the spin filtering-effect and achieving large TMR values at low bias and a monotonic decrease of TMR with the applied bias voltage. This TMR low bias amplitude modulation produced by the ferroelectric polarization reversal reveals a strong interfacial magneto-electric coupling mediated by the oxygen vacancies.

Both TER and the modulation of the TMR disappear at 100 K probably due to the pinning of the ferroelectric polarization in the oxygen vacancies defects after many poling cycles, or due to the activation of the oxygen vacancies which breaks the asymmetry in the system. In this temperature range when the ferroelectric polarization is pointing down the TMR presents low bias suppression and an increasing of its amplitude while increasing temperature. These results evidence a negative spin-filter effect produced by the induced magnetism at the BTO barrier. On the other hand when the ferroelectric polarization is pointing upward the TMR at low bias is large and it decreases while increasing temperature like the standard magnetic tunnel junctions with no magnetic barrier. Furthermore, the negative spin-filter effect, or in other words,

the barrier magnetism, can be controlled by the ferroelectric polarization reversal revealing a new kind of magnetoelectric effect that have never been observed in multiferroic tunnel junctions.

Throughout this thesis we have explored the interfaces properties between functional oxides using tunnel junction architecture exploring the variation of the spin dependent transport by an electric field through the reversal of the ferroelectric polarization of the barrier. Our results reveal the importance of oxygen vacancy at the interfaces in complex oxide heterostructure, and its huge effect in tunneling transport. These defects produce not only variations in ferroelectric properties such pinning, fatigue or preferential ferroelectric polarization direction, but it has a huge influence in the interfacial magneto-electric coupling between the ferromagnetism of the electrodes and ferroelectricity of the tunnel barrier. Furthermore, the oxygen vacancies produce an asymmetry in the LSMO/BTO/LSMO system enhancing the tunnel electroresistance in our multiferroic tunnel junctions. We demonstrated that it is crucial to take account the presence of this common defect in transition metal oxides heterostructures. Moreover, the influence of oxygen vacancies in ultrathin ferroelectric layer where the interface effects has a large influence in ferroelectric properties it is also crucial. Pinning of the ferroelectric polarization, interfacial dopping effect or strain gradients could be produced by the presence of small amounts of these effects, so it is decisive to take account this defects to conclude experimental results in multiferroic tunnel junction. The interfacial properties observed in our LSMO/BTO/LSMO multiferroic tunnel junctions are not only interesting from fundamental point of view but are also important to design novel functional spintronic devices.

7 Summary

1 Introduction

Materials and structures with coupled magnetic and electric characteristics have recently attracted significant interest due to intriguing physical properties and potential applications [1-3]. In heterostructures composed with ferromagnetic and ferroelectric transition metal oxides thin layers a strong magneto-electric coupling could occurs across interfaces. Because of the high sensitivity of tunnel conductance to the metal/insulator interface, magnetic tunnel junctions with a ferroelectric insulating barrier appear as very appropriate architectures to study the interplay between the two ferroic orders, or possible magnetic or electronic interfacial reconstructions [4]. In these artificial multiferroic devices thus display four different resistance states by switching the relative magnetizations alignment of the ferromagnetic electrodes for both directions of the ferroelectric polarization [5]. It has been recently observed magneto-electric effects due to the ferroelectric polarization reversal of the tunnel barrier, such interfacial spin polarization control [6, 7], and magnetic phase transition [8]. The origin of the resistive switching in multiferroic tunnel junctions or ferroelectric tunnel junction is still controversial. Resistive switching is a well-known phenomena in complex oxides

metal-insulator-metal junctions. In these systems this phenomena is commonly explained in terms of the electrochemical migration of oxygen vacancies [9]. Because ferroelectric domains walls motion is faster than the speed of oxygen vacancies [10] short voltage pulses are applied in order to pole the tunnel barrier avoiding oxygen vacancies activation. Working at low temperatures where the oxygen vacancies are "frozen" is another possibility to reduce oxygen vacancies migration. A method to distinguish ferroelectric resistive switching from non-ferroelectric resistive switching consists in combine PFM with conducting tip AFM [11]. By comparing the ferroelectric coercive field with that needed to switch the device resistance, it can be easily deduced whether ferroelectricity and resistive switching are correlated, however, more complex resistive switching mechanisms involving electrochemical interface reactions associated with ferroelectric polarization reversal cannot be excluded. Although the oxygen vacancies activation could be negligible as resistive switching mechanism small amount of these defects can produce huge effect in ferroelectric properties such pinning ferroelectric polarization or fatigue [12]. Moreover, in multiferroic tunnel junction it is never been explored the effects oxygen vacancies in the ferroelectric polarization reversal of the barrier and its influence in the tunnel conductance.

In this thesis we explored the spin-dependent transport in complex oxide-based magnetic tunnel junction with a $BaTiO_3$ ferroelectric barrier and $La_{0.7}Sr_{0.3}MnO_3$ ferromagnetic electrodes. We took advantages of the large sensitivity of the tunnel conductance to the interface properties in order to study magnetic and electronic reconstructions at the $La_{0.7}Sr_{0.3}MnO_3/BaTiO_3$ interface, the interplay between ferroelectricity and ferromagnetism and the oxygen vacancies influence. We found that the oxygen vacancies at the LSMO/BTO interface play an important role in the tunneling transport producing and enhancement of the tunnel electroresistance, and a strong interfacial magneto-electric effect. We correlated these results using interfacial sensitive techniques such aberration corrected scanning transmission electron microscopy combining with electron energy loss spectroscopy or X-ray magnetic circular dichroism.

2 Objectives

- Produce high quality $La_{0.7}Sr_{0.3}MnO_3/BaTiO_3$ samples which present magnetism and ferroelectricity simultaneously at nanometric thickness scale using high oxygen pressure sputtering technique.

- Fabricate tunnel junction devices using optical lithography and Ar ion milling techniques.

- Characterize magnetotransport properties of the tunnel junction devices

- Explore the magnetic and electronic reconstruction and the interplay of ferromagnetism and ferroelectricity at the $La_{0.7}Sr_{0.3}MnO_3/BaTiO_3$ interface.

3 Results and Conclusions

We started in chapter 3 by characterizing the physical properties of $La_{0.7}Sr_{0.3}MnO_3/BaTiO_3$ heterostructures. We demonstrate that we are able to grow high quality LSMO/BTO epitaxial heterostructures. The slow deposition ratio of the high oxygen pressure sputtering technique enables the control of the thin-film growth at the unit-cell level. The samples present no chemical interdiffussion and they are free of defects over long lateral distances. The LSMO thin-films present magnetic properties similar to the LSMO bulk. We studied the magnetic easy axis of the LSMO of different thicknesses grown on $SrTiO_3$ substrates and on $BaTiO_3$ buffered layer, proving that is possible to achieve an antiparallel alignment of the magnetization of two LSMO thin films separated by a BTO ultrathin film. The ferroelectricity persists down 4.4 nm in our BTO ultrathin-films grown on LSMO buffered layer making it possible to implement BTO ultrathin films as active tunnel barrier. We found a preferential downward ferroelectric polarization direction which probably be related with the presence of oxygen vacancies at the LSMO/BTO interface.

In the next chapter we studied the spin dependent transport in LSMO/BTO/LSMO magnetic tunnel junctions. We observed sharp resistance jumps when the magnetic configuration turns from parallel alignment of the magnetization directions of the ferromagnetic electrodes to the antiparallel alignment. The antiparallel state is stable with higher resistance value evidencing the positive spin polarization of the LSMO electrode. The measured tunnel magneto resistance values are larger than 100% evidencing the half-metallic character of the LSMO ferromagnetic electrodes. We found a low suppression of the TMR at low bias and an oscillatory dependence of the tunnel conductance as a function of applied bias that are stronger at lower temperatures. We explain this result in terms of a Coulomb blockade charging effect due to the presence of metallic cluster embedded into the BTO tunnel barrier. We explored the origin of these metallic cluster finding oxygen vacancies at the LSMO/BTO bottom interface. Although in-plane transport measurement of the LSMO bottom electrode reveals a Curie temperature larger than room temperature that is in good agreement with the magnetometry characterization, in the tunneling transport of a LSMO/BTO bilayer tunnel junctions appears a metal-insulator transition near 150K revealing a strong depression of the interfacial manganite bottom electrode Curie temperature which is a direct evidence of the existence of oxygen vacancies in such interface. These oxygen vacancies at the highly strained BTO/LSMO bottom interface encompass a doping effect by the associated electron density. We found that this interfacial charge density presents an induced magnetic moment, demonstrated by X-ray magnetic circular dichroism and polarized neutron reflectometry measurements. We found that this Ti induced magnetic moment is antiferromagnetically coupled to the Mn magnetic moment. This interfacial magnetism could lead to a negative spin-filtering effect in good agreement with the TMR low bias suppression. We also found an electric field control of the LSMO top electrode anisotropy. Modifying the LSMO top electrode coercive field we are able to switch the relative magnetizations alignment of the LSMO ferromagnetic electrodes from AP to P state applying voltage pulses; however, this process is irreversible because we could not recover the AP state using electric fields.

Finally in chapter 5 we explored the effect of the ferroelectric properties of the BTO barrier in the tunneling transport. We found large tunnel electro resistance of near 1000% switching the direction of the ferroelectric polarizations

revealing an asymmetry in the LSMO/BTO/LSMO tunnel junction. This is interpreted in terms of a variation of the effective barrier thickness due to a large modulation of electron density at the BTO/LSMO interface. The reversal of the ferroelectric polarization of the BTO causes accumulation or depletion of the electron density generated by the oxygen vacancies at the bottom interface to screen the polarization charges giving rise to a significant modulation of the width of the tunneling barrier. Furthermore, for the down-polarization, for which lower resistance values are found, tunnel magnetoresistance (TMR) is also strongly depressed, as a result of a depolarization of the tunneling current. This TMR modulation should be related to the presence of an induced Ti magnetic moment in BTO at the interface, antiferromagnetically coupled to that of Mn in LSMO, as detected by X-ray magnetic circular dichroism (XMCD) measurements. When the ferroelectric polarization is pointing upward the magnetic moment disappears because the charge density at the bottom interface is depleted cancelling the negative spin filter effect and reaching larger TMR values at low bias. Due to the interfacial charge density generated by the oxygen vacancies, the ferroelectric polarization reversal produces a large modulation of the TMR at low bias revealing a strong magneto-electric coupling in our LSMO/BTO/LSMO heterostructures. We also found a giant electro resistance of near 100000% in $La_{0.7}Sr_{0.3}MnO_3/BaTiO_3/Ag$ tunnel junction. We explain this electroresitance in terms of a change of the transport mechanism from Schottky injection to tunnel across the BTO layer.

Throughout this thesis we have explored the interfaces properties between functional oxides using tunnel junction architecture exploring the variation of the spin dependent transport by an electric field through the reversal of the ferroelectric polarization of the barrier. Our results reveal the importance of oxygen vacancy at the interfaces in complex oxide heterostructure, and its huge effect in tunneling transport. We verified that it is possible to modify the spin-dependent transport using electric fields due to the ferroelectric character of the tunnel barrier. We demonstrated that these interfacial properties in all-oxide multiferroic tunnel junction are not only interesting from fundamental point of view but are also important to design novel functional spintronic devices.

4 References

[1] M. Fiebig, *J. Phys. D: Appl. Phys*. **38**, R123 (2005).

[2] W. Eerenstein, N. D. Mathur, and J. F. Scott, *Nature* **442**, 759 (2006).

[3] R. Ramesh, and N. A. Spaldin, *Nat. Mater*. **6** 21 (2007).

[4] M. Bibes, J. Villegas, and A. Barthelemy, *Adv. Phys.* **60**, 5 (2011).

[5] J. Velev, C.-G. Duan, J. D. Burton, A Smogunov, M. K. Niranjan, E. Tosatti, S. S. Jaswal, and E. Y. Tsymbal, *Nano Letters* **9**, 427 (2009).

[6] V. Garcia, M. Bibes, L. Bocher, S. Valencia, F. Kronast, A. Crassous, X. Moya, S. Enouz-Vedrenne, A. Gloter, D. Imhoff, C. Deranlot, N. D. Mathur, S. Fusil, K. Bouzehouane, and A. Barthélémy, *Science* **327**, 1106-1110 (2010).

[7] D. Pantel, S. Goetze, D. Hesse, and M. Alexe, *Nature Mater.* **11**, 289 (2012).

[8] Y. W. Yin, J. D. Burton, Y-M. Kim, A. Y. Borisevich, S. J. Pennycook, S. M. Yang, T.W. Noh, A. Gruverman, X. G. Li, E. Y. Tsymbal, and Q. Li. *Nature Mater*. **12**, 397 (2013).

[9] R. Waser, and M. Aono, Nature Mater. **6**, 833 (2007).

[10] N. Ng, R. Ahluwalia, and D. J. Srolovitz, *Phys. Rev. B* **86**, 094104 (2012).

[11] H. Kohlstedt, A. Petraru, K. Szot A. Rüdiger, P. Meuffels, H. Haselier, R. Waser, and V. Nagarajan, *Appl. Phys. Lett.* **92**, 062907 (2008).

[12] M. Dawber, K. M. Rabe, and J. F. Scott, Rev. Mod. Phys. **77**, 1083 (2005).

Resumen en Español

1 Introducción

El acoplamiento magneto-eléctrico en interfases de heteroestructuras que combinan laminas ultra-delgadas de materiales ferromagnéticos y ferroeléctricos, han generado recientemente un gran interés debido a la posibilidad de controlar propiedades magnéticas usando campos eléctricos [1-3]. En concreto la propiedad de revertir la imanación usando únicamente campos eléctricos permitiría solventar el principal problema a la hora de miniaturizar las memorias magnéticas de acceso aleatorio (magnetic random access memories MRAM), ya que en estos dispositivos, comúnmente usados en los discos duros, la operación de escritura requiere altas densidades de corriente eléctrica para producir campos magnéticos. Gracias a la alta sensibilidad que posee la conductancia túnel a los efectos interfaciales, las uniones túnel con barrera ferroeléctrica, también llamadas uniones túnel multiferroicas, son sistemas idóneos para el estudio la interacción entre ferromagnetismo y ferroelectricidad, así como las posibles reconstrucciones electrónicas y magnéticas en las interfases entre dichos materiales [4]. Estos dispositivos de carácter multiferroico presentan cuatro estados estables de resistencia al cambiar el alineamiento relativo de las imanaciones de los electrodos ferromagnéticos, y la dirección de la polarización ferroeléctrica [5]. Al invertir la dirección de la polarización ferroeléctrica de la

barrera túnel se ha observado recientemente que se puede controlar la polarización de espín interfacial de los electrodos ferromagnéticos [6, 7], o su estado magnético [8], demostrando un fuerte acoplamiento magneto-eléctrico. El origen de está electroresistencia túnel en estos dispositivos multiferroicos no está completamente clara y todavía es fuente de debate. En óxidos de metales de transición, la electroresistencia que aparece en uniones metal/aislante/metal es un fenómeno bien conocido [9], que se debe fundamentalmente a la migración de vacantes de oxígeno y a las reacciones electroquímicas en la interfase metal/aislante envueltas en este proceso. Debido a que la dinámica de dominios ferroeléctricos es mucho más rápida que la velocidad de las vacantes de oxígeno [10], se pueden aplicar pulsos cortos de voltaje que evitan la activación de vacantes de oxígeno, o trabajar a bajas temperaturas donde las vacantes son inmóviles. Un método comúnmente usado para comprobar si la electroresistencia túnel es debido a la inversión de la polarización ferroeléctrica consiste en combinar microscopía de fuerzas atómicas con punta conductora (CT-AFM) y microscopía de piezorrespuesta (PFM) [11]. Si el campo coercitivo ferroeléctrico coincide con el campo eléctrico al que se la resistencia salta de valor ambos se pueden correlacionar, sin embargo, otros mecanismos más complejos pueden ocurrir como por ejemplo reacciones electroquímicas en las interfases asociadas al cambio de la dirección de la polarización ferroeléctrica y no se pueden excluir. Aunque la activación de vacantes de oxígeno es un mecanismo que puede llegar a ser improbable en el fenómeno de electroresistencia túnel, pequeños porcentajes de estos defectos pueden producir grandes efectos en las propiedades ferroeléctricas como anclaje de dominios ferroelectricos o fatiga [12]. A pesar de ello, en los dispositivos túnel multiferroicos todavía no se ha estudiado el efecto de las vacantes de oxígeno en la inversión de la polarización ferroeléctrica de la barrera o ni su influencia en la conductancia túnel.

En este trabajo de tesis se estudia el transporte dependiente de espín en uniones túnel basadas en óxidos complejos con barrera túnel ferroeléctrica de $BaTiO_3$ y electrodos ferromagnéticos de $La_{0.7}Sr_{0.3}MnO_3$. Aprovechando la alta sensibilidad de la corriente túnel a las propiedades interfaciales, se ha estudiado la reconstrucción eléctrica y magnética en la interfase $La_{0.7}Sr_{0.3}MnO_3/BaTiO_3$, la interacción entre ferromagnetismo y ferroelectricidad y la influencia de las vacantes de oxígeno. Se ha encontrado que las vacantes localizadas en la interfase LSMO/BTO juegan un papel importante en el transporte túnel, siendo

responsables de un incremento de la electroresistencia túnel, y de un fuerte acoplamiento magneto-eléctrico interfacial. Se han correlacionado estos resultados con distintas técnicas sensibles a las interfases, como lo son el dicroísmo circular magnético o la microscopía electrónica de transmisión y barrido de contraste-Z unido a técnicas de análisis como la espectroscopía de pérdida de energía de electrones.

2 Objetivos

- Crecimiento de heteroestructuras $La_{0.7}Sr_{0.3}MnO_3/BaTiO_3$ epitaxiales de alta calidad cristalina mediante la técnica de pulverización (sputtering) de alta presión de oxígeno que presenten simultáneamente buenas propiedades ferromagnéticas y ferroelectricas en la nano-escala.

- Desarrollo y fabricación de los dispositivos de unión túnel de tamaño micrométrico en escala lateral por técnica de litografía óptica y comido seco por iones argón.

- Caracterización de las propiedades de magnetotransporte en los dispositivos de unión túnel.

- Estudio de la reconstrucción magnética y electrónica, así como la interacción entre ferromagnetismo y ferroelectricidad en las interfases entre $La_{0.7}Sr_{0.3}MnO_3$ y $BaTiO_3$.

3 Resultados y Conclusiones

En el capítulo 3 se han caracterizado las propiedades estructurales, magnéticas y ferroeléctricas de las heteroestructuras $La_{0.7}Sr_{0.3}MnO_3/BaTiO_3$. Se ha comprobado la alta calidad cristalina de las muestras crecidas. Mediante técnicas de difracción de rayos-X, y microscopía electrónica de alta resolución se

ha comprobado que las muestras crecen epitaxiales libres de defectos estructurales, y no presentan interdifusión química a través de las interfaes entre distintos materiales. Se ha verificado que las láminas ultra-delgadas de LSMO poseen propiedades magnéticas cercanas a las de muestras en volumen, y que es posible obtener un alineameatiento antiparalelo de las direcciones de las imanaciones de las dos capas de LSMO separados por una capa ultra-delgada de BTO. Por último se ha confirmado que las propiedades ferroeléctricas en capas ultra delgas de BTO crecidas sobre una lamina de LSMO persisten por debajo de los 4.4 nm de grosor, haciendo posible su uso como barrera túnel activa. La polarización ferroeléctricas de dichas capas presenta una dirección preferencial hacia abajo (apuntando hacia la capa de LSMO).

En el siguiente capítulo se ha estudiado el transporte dependiente de espín en uniones túnel usando electrodos ferromagnéticos de LSMO y barrera túnel de BTO. Se han medido grandes valores de magnetoresistencia túnel superiores al 100%, demostrando el carácter medio-metal de los electrodos. La magnetoresistencia túnel medida a bajos voltajes presenta una fuerte disminución de su valor y un carácter oscilatorio para todo el rango de voltajes medido que resulta más acusado a bajas temperaturas. Esta compleja fenomenología es explicada en términos de un efecto de carga producido por bloqueo de Coulomb debido a la existencia de agrupamientos de vacantes de oxigeno de escala nanométrica en la interfase de abajo de la tricapa LSMO/BTO/LSMO. La densidad de carga producida por dichas vacantes presenta un momento magnético inducido, que ha sido medido mediante dicroísmo circular magnético y reflectometría de neutrones polarizados. Además se ha demostrado que es posible cambiar el alineamiento relativo de las imanaciones de los electrodos de LSMO desde el estado antiparalelo al estado paralelo usando únicamente campos eléctricos. Este proceso es irreversible pues no se puede recuperar nuevamente el estado antiparalelo mediante pulsos de voltaje.

Finalmente en el capítulo 5 se ha explorado el efecto de las propiedades ferroeléctricas de la barrera túnel en el transporte túnel. Al cambiar la dirección de la polarización ferroleléctrica de la barrera túnel se produce un efecto de electroresistencia túnel superior al 1000%, lo que evidencia una fuerte asimetría en las uniones túnel LSMO/BTO/LSMO. Este resultado se produce debido a la modulación de la densidad de carga en la interfase inferior de la tricapa

LSMO/BTO/LSMO producida por la inversión de la dirección de la polarización ferroeléctrica. El efecto resultante es una variación de la anchura efectiva de la barrera túnel que afecta fuertemente la corriente túnel. Asimismo, cuando la dirección de la polarización ferroeléctrica apunta hacia abajo se ha encontrado que la magneto resistencia túnel a bajos voltajes está fuertemente deprimida como resultado de un filtrado de espín en la corriente túnel a consecuencia del momento magnético inducido en el Ti acoplado antiferromagneticamente con el momento magnético del Mn. Sin embargo, cuando la dirección de la polarización ferroeléctrica apunta hacia arriba se produce un vaciamiento de carga en la interfase inferior. Al no haber carga el momento inducido en la interfase desaparece lo que produce y una cancelación del filtrado de espín. Como consecuencia de esto, la fuerte depresión de la magnetorresistencia túnel a bajos voltajes se suprime produciendo un fuerte aumento de su valor a bajos voltajes, dando lugar a una modulación del TMR. También se ha encontrado una gran electroresistencia al modificar la dirección de la polarización ferroeléctrica en el sistema LSMO/BTO/Ag cercana al 100000% producido por un cambio en el mecanismo de transporte a través del BTO.

A lo largo de esta tesis se han investigado las propiedades interfaciales de óxidos de metales de transición con orden ferroico usando estructuras de unión túnel. Nuestros resultados muestran la importancia de las vacantes de oxígeno en las interfases de la heteroestructuras de óxidos complejos, y su fuerte influencia en el transporte túnel. Se ha comprobado que es posible modificar la corriente túnel dependiente de espín usando campos eléctricos gracias al carácter ferroelectrico de la barrera túnel. Con esto se demuestra que estas propiedades interfaciales en las uniones túnel multiferroicas basadas en óxidos de metales de transición no son solo interesantes desde un punto de vista fundamental, sino que también pueden ser de gran utilidad a la hora de diseñar nuevos dispositivos funcionales en el campo de la espintrónica.

4 Bibliografía

[1] M. Fiebig, *J. Phys. D: Appl. Phys*. **38**, R123 (2005).

[2] W. Eerenstein, N. D. Mathur, and J. F. Scott, *Nature* **442**, 759 (2006).

[3] R. Ramesh, and N. A. Spaldin, *Nat. Mater*. **6** 21 (2007).

[4] M. Bibes, J. Villegas, and A. Barthelemy, *Adv. Phys.* **60**, 5 (2011).

[5] J. Velev, C.-G. Duan, J. D. Burton, A Smogunov, M. K. Niranjan, E. Tosatti, S. S. Jaswal, and E. Y. Tsymbal*, Nano Letters* **9**, 427 (2009).

[6] V. Garcia, M. Bibes, L. Bocher, S. Valencia, F. Kronast, A. Crassous, X. Moya, S. Enouz-Vedrenne, A. Gloter, D. Imhoff, C. Deranlot, N. D. Mathur, S. Fusil, K. Bouzehouane, and A. Barthélémy, *Science* **327**, 1106-1110 (2010).

[7] D. Pantel, S. Goetze, D. Hesse, and M. Alexe, *Nature Mater.* **11**, 289 (2012).

[8] Y. W. Yin, J. D. Burton, Y-M. Kim, A. Y. Borisevich, S. J. Pennycook, S. M. Yang, T.W. Noh, A. Gruverman, X. G. Li, E. Y. Tsymbal, and Q. Li. *Nature Mater*. **12**, 397 (2013).

[9] R. Waser, and M. Aono, Nature Mater. **6**, 833 (2007).

[10] N. Ng, R. Ahluwalia, and D. J. Srolovitz, *Phys. Rev. B* **86**, 094104 (2012).

[11] H. Kohlstedt, A. Petraru, K. Szot A. Rüdiger, P. Meuffels, H. Haselier, R. Waser, and V. Nagarajan, *Appl. Phys. Lett.* **92**, 062907 (2008).

[12] M. Dawber, K. M. Rabe, and J. F. Scott, Rev. Mod. Phys. **77**, 1083 (2005).